WISCO

UNIVERSITY OF WISCONSIN • MADISON, WISCONSIN

AN ANALYSIS OF MONOJET DATA IN $p\bar{p}$ COLLISIONS AT $\sqrt{s} = 1.8$ TEV

by

RICHARD MARKELOFF

A thesis submitted in partial fulfillment of the

requirements for the degree of

DOCTOR OF PHILOSOPHY

(Physics)

at the

UNIVERSITY OF WISCONSIN - MADISON

1992

ONSIN

Abstract

An analysis is presented of events with a single jet and significant missing transverse energy selected from 4.7 pb^{-1} of data collected at the Fermilab Tevatron with the CDF detector. The goal is to identify events of the type $p\bar{p} \rightarrow Z^0 + \mathrm{jet}$; $Z^0 \rightarrow \nu\bar{\nu}$. Event selection and backgrounds are discussed. The number of observed monojet events is compared to the number of observed $Z^0 \rightarrow e^+e^-$ events in which the Z^0 is accompanied by a jet. We measure the number of light neutrino species to be $N_\nu = 2.2 \pm 1.5$ and we place an upper limit on the number of neutrino species at $N_\nu < 5$ (90% C.L.).

Acknowledgements

I would like to thank my thesis advisor, Lee Pondrom, for all that he has taught me. Without his support, this work would never have been completed. I would also like to extend my gratitude to Tom Phillips for the valuable advice he has given me, and to Jim Bellinger, who never failed to offer his assistance when I needed it. I also appreciate all the help that I have received from my many other CDF colleagues.

My heartfelt thanks to my wife, Jeannine Esmonde, for standing by me through my long years in graduate school.

This work was supported by the United States Department of Energy Contract DE-AC02-76ER00881.

Contents

Abstract ii

Acknowledgements iii

1 Introduction 1

1.1 The Standard Model 2

1.2 Intermediate Vector Boson Production in the Standard Model . . 5

1.3 Missing E_t and Monojets 5

2 Experimental Apparatus 9

2.1 The Tevatron Collider 9

2.1.1 Accelerating Protons 9

2.1.2 Producing Antiprotons 11

2.1.3 Collider Operation 12

2.2 The CDF Experiment 13

2.2.1 Tracking Detectors 14

2.2.1.1 The Vertex Time Projection Chambers 14

2.2.1.2 The Central Tracking Chamber 19

2.2.2 Calorimeters 21

2.2.2.1 The Central and Endwall Calorimeters 23

2.2.2.2 The Gas Calorimeters 24

2.2.2.3 Calorimeter Calibration 26

2.2.3 The Central Muon System 28

2.2.4 The Forward Muon System 30

2.2.5 The Beam-Beam Counters 31

2.2.6 The Trigger 31

3 Event Selection **37**

3.1 The Primary Data Sample 37

3.2 Sources of Background 40

3.3 Tau Cuts 43

3.4 Muon Cuts 44

3.5 Electron Cuts 45

3.6 The Undeposited p_t Cut 49

3.7 The CTC Dijet Cuts 53

3.8 Backgrounds from Cosmic Rays and Beam Gas 57

3.9 The Monojet Sample 70

4 Monte Carlo Simulations of W and Z Decays **74**

4.1 The Event Generator 75

4.2 Parton Fragmentation 79

4.3 Detector Simulation 80

4.4 $Z^0 \rightarrow \nu\bar{\nu}$ Signal 83

4.5 W and Z Backgrounds 85

4.5.1 $W \rightarrow \tau\nu$ Background 87

5 QCD Backgrounds **96**

5.1 Dijet Backgrounds 100

5.1.1 Identifying Dijet Events with the CTC and VTPC 100

5.1.2 Estimating Dijet Backgrounds from Tracking Information . 103

5.1.3 Dijet Detection Efficiency 105

5.1.4 Calculating the True Positive Rates 107

5.1.5 Calculating the False Positive Rates 109

5.1.6 The Estimated Dijet Background 112

5.2 Multijet Backgrounds 118

5.2.1 Multijet Events with One Jet Lost or Mismeasured 119

5.2.2 Multijet Events with Two or More Jets Lost or Mismeasured 123

5.3 Summary of QCD Backgrounds 128

6 Backgrounds from Prompt Photons and Neutral Hadrons **129**

6.1 The CDF Direct Photon Sample 132

6.2 Calculating the Direct Photon/Neutral Hadron Background . . . 136

7 Conclusions **145**

7.1 Comparison to $Z^0 \rightarrow e^+e^-$ 145

7.1.1 The CDF $Z^0 \rightarrow e^+e^-$ Sample 147

7.1.2 The Ratio $Br(Z^0 \rightarrow \nu\bar{\nu})/Br(Z^0 \rightarrow e^+e^-)$ 150

7.2 The Monojet Missing E_t Spectrum 152

7.3 Limits on New Physics 154

7.4 Possible Improvements to this Study 157

A Corrections to the Missing E_t Measurement **161**

A.1 Clustered Energy Corrections 162

A.2 Unclustered Energy Corrections 163

A.3 Systematic Errors 163

B The CDF Detector Simulation Program **166**

B.1 Calorimeter Simulation 167

B.2 Tracking Simulation 168

C Calculating the Monojet Signal Upper Limit **169**

List of Tables

1.1 The fundamental constituents of matter in the Standard Model. . 3

1.2 Fundamental forces and gauge bosons. 4

3.1 Number of events rejected by the background cuts 69

4.1 Results of Monte Carlo simulations of $Z^0 \rightarrow \nu\bar{\nu}$ 84

4.2 Results of Monte Carlo simulations of W and Z decays. 88

4.3 Summary of factors in the τ background calculation. 92

5.1 True positive rates for various values of N_{cut}^{VTPC} and the nominal CTC cuts 109

5.2 False positive rates for CTC cuts determined from $Z^0 \rightarrow \nu\bar{\nu}$ Monte Carlo 110

5.3 False positive rates for various values of N_{cut}^{VTPC} 111

5.4 False positive rates for CTC cuts determined from direct photon data 114

5.5 Summary of estimated number of non-dijet events and dijet background in Region 2 116

5.6 Fraction of events with 3 or more clusters that have 2 or more clusters in crack regions 124

6.1 Trigger and event selection cuts for the direct photon sample . . . 134

7.1 Summary of background estimates 146

7.2 Trigger and event selection efficiencies for $Z^0 \rightarrow e^+e^-$ events . . . 150

7.3 Characteristics of $Z^0 \rightarrow e^+e^-$ events that pass the monojet cuts . 152

7.4 Recent measurements of N_ν, the number of light neutrino species 153

C.1 Upper limits on the monojet signal, and corresponding confidence levels 173

List of Figures

1.1 Lowest order Feynman diagrams for IVB production 6

1.2 Feynman diagrams for monojet production 7

2.1 The Fermilab accelerator complex 10

2.2 The Antiproton Source 12

2.3 A perspective view of the CDF detector 15

2.4 The CDF detector as it was used during the 1988-89 run 16

2.5 Two of the eight Vertex Time Projection Chamber (VTPC) modules 18

2.6 End view of the CTC 19

2.7 Wire geometry for an axial drift cell in the CTC 20

2.8 Quadrant of the calorimeter 22

2.9 Hadron calorimeter towers in one of eight identical η-φ quadrants 22

2.10 A central calorimeter wedge 24

2.11 E_t/p_t distribution for W electrons 28

2.12 Location of the Central Muon Chambers 29

2.13 A CMU drift cell 30

2.14 r-φ view of one of the FMU planes 32

2.15 r-φ view of one of the Beam-Beam Counter planes 33

2.16 The $\not{E}_t$ trigger efficiency 36

3.1 The missing E_t significance for minimum bias events 41

3.2 The LSHR distribution for a sample of W electrons. 50

3.3 CES χ^2 distributions 51

3.4 PEM $\chi^2_{3\times3}$ distributions 52

3.5 A QCD background event 54

3.6 A dijet background event found by the CTC track clustering algorithm 56

3.7 Charged fraction of the leading cluster in monojet candidates and dijet events 59

3.8 Scatter plot of charged fraction vs. out of time energy for the monojet candidates 61

3.9 r-φ display for cosmic ray background event 62

3.10 The CES/CEM ratio for the monojet candidates 63

3.11 Scatter plot of charged fraction vs. CES/CEM ratio for the monojet candidates 64

3.12 VTPC display for a beam gas event 66

3.13 VTPC display for a typical monojet event 67

3.14 Charged fraction of the leading cluster in monojet candidates after cosmic ray/beam gas background cuts 68

3.15 Raw $\not{E}_t$ distribution for the monojet sample 71

3.16 Calorimetry lego display for a typical monojet event 72

3.17 CTC r-φ display for a typical monojet event 73

4.1 The parton model picture of a hadron-hadron interaction 77

4.2 Comparison between jet fragmentation in W events and Monte Carlo 81

4.3 Comparison between the underlying events in W events and Monte Carlo. The variables displayed are defined in the text. 82

4.4 The $\not{E}_t$ spectrum of the $Z^0 \rightarrow \nu\bar{\nu}$ signal from Monte Carlo and the upper and lower systematic bounds 86

4.5 The $\not{E}_t$ spectrum of the W and Z background, from Monte Carlo 89

4.6 The estimated $\not{E}_t$ spectrum of the W and Z background used in calculating the final results 90

4.7 Comparison of data and Monte Carlo for monojet candidates rejected by tau cuts. 94

4.8 $\not{E}_t$ spectrum of estimated $W \rightarrow \tau\nu$; $\tau \rightarrow$ hadrons background . . 95

5.1 Distribution in η-φ space of the centroid of the smaller jet in mismeasured dijet events 98

5.2 Azimuthal coordinate (modulo 15°) of central poorly measured jets 99

5.3 Lowest order Feynman diagrams for QCD parton-parton scattering 101

5.4 Dijet identification probability for CTC and VTPC track clustering 108

5.5 VTPC dijet identification false positive rates for IVB decays and direct photon events 113

5.6 Estimated $\not{E}_t$ spectrum of dijet background 117

5.7 $\Delta\varphi$ between $\not{E}_t$ vector and second or third clusters 121

5.8 $\Delta\varphi$ between the $\not{E}_t$ vector and the fourth cluster 122

6.1 Lowest order Feynman diagrams for direct photon production . . 130

6.2 Photon strip and wire clusters in a CES chamber. 135

6.3 The neutral hadron selection efficiencies for the CES cuts 137

6.4 CES χ^2 distributions for photons and neutral hadron background 138

6.5 The probability for a photon to escape detection as a function of photon p_t 141

6.6 Fraction of prompt photon and neutral hadron background events with the photon candidate in the region $|\eta| > 0.9$ 142

6.7 The $\not{E}_t$ spectrum of the prompt photon and isolated neutral hadron background 144

7.1 The $\not{E}_t$ spectrum of the estimated sum of background + signal, compared to data 155

A.1 Corrected $\not{E}_t$ distribution for the monojet sample 165

Chapter 1

Introduction

In the 5th century B.C., the Greek philosopher Democritus proposed that all matter is composed of infinitesimally small, indivisible particles called atoms; and that all physical processes are ultimately the result of the motions of atoms. Today, such concepts may be so familiar that we hardly take notice of them, but at the time these ideas were bold and startling. Democritus' contributions towards our understanding of the fundamental structure of the universe are of great significance.

Now, in the last decade of the twentieth century, the intellectual heirs of Democritus are still striving to understand the fundamental constituents of matter and how they interact. These efforts have culminated in the construction of a theoretical framework that has come to be known as the Standard Model. The Standard Model has so far been remarkably successful in explaining the phenom-

ena observed in today's high energy physics experiments, where the structure of the universe is studied at the highest energies and smallest distances currently accessible.

Democritus and his contemporaries also constructed a theoretical model that attempted to explain the world around them. They postulated that atoms are indivisible, and the properties of matter in bulk are determined by the spatial arrangement and shapes of its constituent atoms. They also believed that all matter in the universe was originally formed from a great vortex of atoms swirling in the void. In the centuries that have passed since their time, these ideas have been discarded, and only the seminal concept of the corpuscular nature of matter remains. How much of the Standard Model will future generations of physicists still hold as true, and what parts of it will need to be modified or rejected? There may yet be surprises ahead as accelerator experiments push for greater luminosities and higher energies. In this study, we search the experimental data for phenomena beyond the Standard Model.

1.1 The Standard Model

According to the Standard Model, all matter is composed of quarks and leptons. These fundamental particles are spin-$\frac{1}{2}$ quantum mechanical entities with no discernable internal structure. The quarks and leptons interact via four fundamental forces: electromagnetism, the weak force, the strong force and gravity.

Quark	Charge	Mass (GeV)	Lepton	Charge	Mass (GeV)
up (u)	$+\frac{2}{3}$	0.31	e-neutrino (ν_e)	0	$< 1.8 \times 10^{-8}$
down (d)	$-\frac{1}{3}$	0.31	electron (e)	-1	5.11×10^{-4}
charm (c)	$+\frac{2}{3}$	1.5	μ-neutrino (ν_μ)	0	$< 2.5 \times 10^{-4}$
strange (s)	$-\frac{1}{3}$	0.5	muon (μ)	-1	0.106
top (t)	$+\frac{2}{3}$	?	τ-neutrino (ν_τ)	0	$< 7 \times 10^{-2}$
bottom (b)	$-\frac{1}{3}$	4.5	tau (τ)	-1	1.78

Table 1.1: The fundamental constituents of matter in the Standard Model.

Interactions between particles are the result of the exchange of gauge bosons peculiar to each force. The gauge bosons for the four forces are the photon (γ), the $W^{\pm}$ and the Z^0, the gluon (g) and the graviton. Quarks feel the strong force while leptons do not. These particles and their properties are displayed in Tables 1.1 and 1.2. The quark masses listed in Table 1.1 are calculated from the observed mass spectrum of the baryons (particles composed of quarks.) Because of the properties of the strong interaction, it is impossible to observe a single, isolated quark. Therefore, the definition of a quark mass is somewhat obscure.

Quarks and leptons are naturally organized into three families or generations. The particles in each generation are more massive than the particles in the one before, except for the neutrinos. The current experimental data is consistent with the hypothesis that the neutrinos are massless. Of the twelve quarks and

Force	Gauge Boson	Charge	Spin	Mass (GeV)
Strong	gluon (g)	0	1	0
Electromagnetic	photon (γ)	0	1	0
Weak	W-boson ($W^{\pm}$)	± 1	1	79.8
	Z-boson (Z^0)	0	1	91.1
Gravitational	graviton (G)	0	2	0

Table 1.2: Fundamental forces and gauge bosons.

leptons, the τ neutrino and the top quark have not yet been directly observed. There is compelling evidence for the existence of the τ neutrino; its existence must be postulated in order for momentum to be conserved in the decay of the τ lepton. The top quark may be too massive to be produced by even the most powerful particle accelerators now in operation. The most recent searches for the top quark by the CDF Collaboration have set a lower limit on its mass at 91 GeV [1].

The theory of the Standard Model contains no stricture that limits the number of quark and lepton generations to three. But it is an empirical fact that only three generations exist. The MARK II Collaboration at SLAC have determined the number of neutrino species, N_ν, from measurements of the decay widths of the Z^0 boson and found that $N_\nu = 3$ (95% C.L.) [7],[8]. The existence of only three species of light neutrinos has also been confirmed by the experiments at the

LEP machine at CERN [9]-[13].

1.2 Intermediate Vector Boson Production in the Standard Model

The W and Z particles that are the carriers of the weak force are referred to as intermediate vector bosons (IVB's). In the Standard Model, IVB's are produced through $q\bar{q}$ annihilation. The processes $q\bar{q} \rightarrow W^{\pm} \rightarrow \ell^{\pm}\nu_{\ell}$ and $q\bar{q} \rightarrow Z^0 \rightarrow \ell\bar{\ell}$ are shown symbolically in Figure 1.1. Diagrams like those shown in Figure 1.1 are called Feynman diagrams. A Feynman diagram is a sort of space-time schematic of a quantum mechanical reaction. The diagrams in Figure 1.1 are the lowest order diagrams for IVB production. This means that they represent the simplest sequence of fundamental interactions that link the initial and final states. The lowest order diagrams give the largest contributions to the quantum mechanical probability amplitude for a given process.

1.3 Missing E_t and Monojets

In this study we examine the so-called "invisible" decays of the Z^0 weak vector boson. These decays are of the form $Z^0 \rightarrow \nu\bar{\nu}$ where the $\nu, \bar{\nu}$ represent neutrinos and antineutrinos from one of the three generations. These decays are said to be "invisible" because the neutrinos feel only the weak force, and the probability that one of them might interact within the volume of the detector is vanishingly

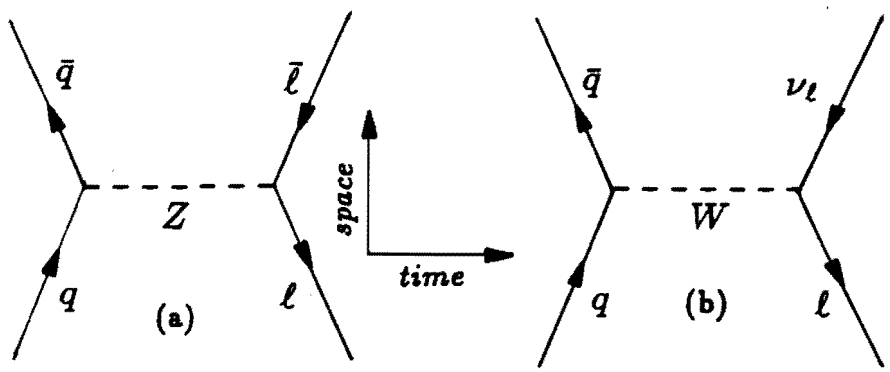

Figure 1.1: The lowest order Feynman diagrams for the processes (a) $q\bar{q} \rightarrow Z^0 \rightarrow \ell\bar{\ell}$ and (b) $q\bar{q} \rightarrow W^{\pm} \rightarrow \ell^{\pm}\nu_\ell$.

small. However, when a Z^0 boson is produced in a proton-antiproton collision it occasionally recoils off a jet of hadronic (strongly interacting) particles. Feynman diagrams for this process are shown in Figure 1.2. In one case the incoming quark radiates a final state gluon, and in the other case a quark is radiated. The quark or gluon fragments into a jet of particles that is observed in the laboratory. It is the presence of this jet that makes it possible to separate the invisible Z^0 decays from other processes that occur in $p\bar{p}$ events. The $p\bar{p}$ collisions are observed in the center of mass frame, and the vector sum of the particles' momenta perpendicular to the beam axis must be zero. An event with a jet and a Z^0 that decays into neutrinos would be characterized by a single jet (a "monojet") with no observed particles to balance its transverse momentum. In practice, we measure the energy and not the momentum of the particles, but for extremely relativistic particles the two quantities are very nearly equal. This technique for isolating invisible

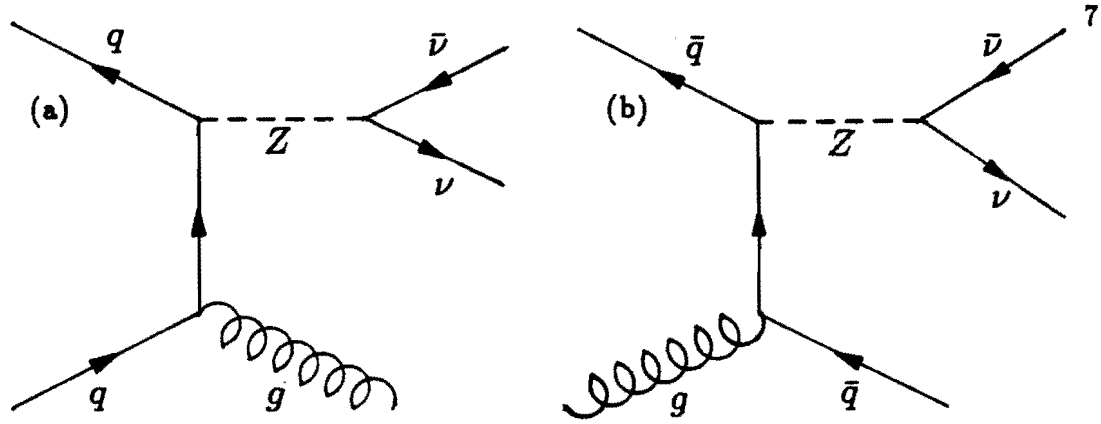

Figure 1.2: Two of the next to leading order Feynman diagrams for Z^0 production with (a) gluon and (b) quark radiation in the final state .

decays has come to be known as Missing Transverse Energy, or Missing Energy for short.

Previous studies seeking new physics in $p\bar{p}$ events with large missing transverse energy ($\not{E}_t$) include searches for supersymmetric particles done at the Fermilab Tevatron [2],[3] and the CERN S$p\bar{p}$S Collider [4],[5]. In these studies no evidence for physics beyond the Standard Model was found. However, these analyses focused on events with two or more hadronic jets, while here we have restricted our attention to events with a single jet and large $\not{E}_t$ (monojets). An analysis of monojet events produced in $p\bar{p}$ collisions has been presented by the UA1 Collaboration [6]. They compared the number of monojet events found in 715 nb^{-1} of $p\bar{p}$ data at $\sqrt{s}$ = 630 GeV to predictions based on Monte Carlo simulations of intermediate vector boson decays and known backgrounds. They arrived at an upper limit for the number of neutrino species: $N_\nu \leq 10$ at the 90%

confidence level. More recently, the L3 Collaboration at CERN have studied events containing single photons with missing E_t produced in e^+e^- collisions at center of mass energies between 88 and 94 GeV [14]. These events represent the e^+e^- analog to monojets: $e^+e^- \rightarrow \gamma Z^0$; $Z^0 \rightarrow \nu\bar{\nu}$. Their results are consistent with the Standard Model and three light neutrino species.

In the following chapters, we describe the Collider Detector at Fermilab, and the monojet data collected from it in the 1988-89 run. We examine the various sources of background for invisible Z^0 decays. We explain the techniques used to eliminate these backgrounds from the data set, and we present estimates of the amount that remains. We then compare the number of $Z^0 \rightarrow \nu\bar{\nu}$ events that we find to the number of $Z^0 \rightarrow e^+e^-$ events found by the CDF Collaboration. Finally, we conclude that the observed frequency of Z^0 decays into neutrinos is consistent with the predictions of the Standard Model and three lepton generations.

Chapter 2

Experimental Apparatus

2.1 The Tevatron Collider

The Tevatron Collider is currently the world's most powerful particle accelerator, capable of producing proton–anti-proton collisions with a center of mass energy of 1.8 TeV. It is part of a complex of accelerators at the Fermi National Accelerator Laboratory near Batavia, Illinois. A schematic of the Fermilab accelerator system is shown in Figure 2.1. We present here a brief description of accelerator operations at Fermilab. The reader who is interested in more detail should consult References [15].

2.1.1 Accelerating Protons

A proton beam in the Tevatron starts off as negatively ionized hydrogen accelerated by a Cockcroft-Walton generator. This device uses high voltage capacitors charged in parallel and then connected in series to impart an energy of

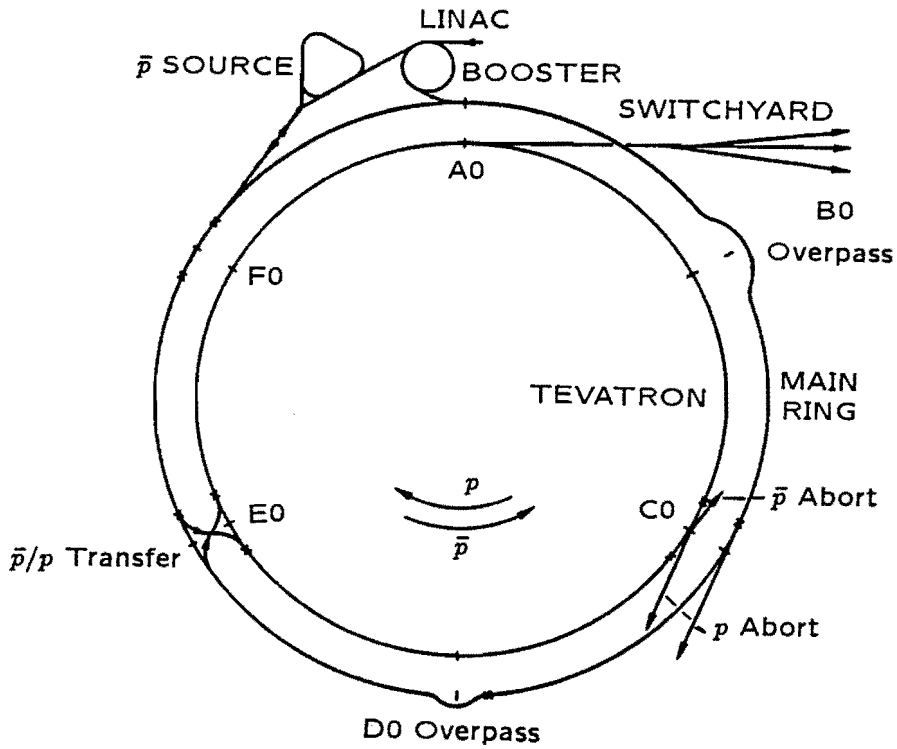

Figure 2.1: The Fermilab accelerator complex.

750 keV to the H^- ions. From the Cockcroft-Walton machine the ions are sent into a linear accelerator (linac). They emerge from the linac with an energy of 200 MeV and enter the booster synchrotron. Here the ions pass through a thin metal foil to strip them of their electrons. The bare protons are then accelerated to 8 GeV and injected into the Main Ring synchrotron.

The Main Ring is 2 km in diameter, and accelerates the proton beam to 150 GeV. At this point, there are around 2.0×10^{12} protons in the Main Ring, and about 84 of the 1113 Main Ring RF buckets are occupied. This results in an average of about 2.5×10^{10} protons per bunch. In collider operations, six bunches of protons are injected into the Tevatron along with six conterrotating bunches of antiprotons. In order to achieve the maximum luminosity, the goal is to have at least 6×10^{10} particles in each proton bunch. The RF fields in the Main Ring

are used to coalesce 8 or more adjacent bunches into a single large bunch.

The protons are then transferred to the Tevatron, which shares the same tunnel with the Main Ring. Although it has the same radius as the Main Ring, the Tevatron's superconducting magnets enable it to achieve a much higher energy. In the Tevatron the beam is accelerated to 900 GeV.

2.1.2 Producing Antiprotons

The Main Ring is also used in the production of antiprotons. When it is operating in this mode, protons are accelerated to 120 GeV and directed to a copper target. About one $\bar{p}$ is captured for every 10^5 protons that strike the target. The antiprotons are focused by a lithium lens and sent to a triangular 8 GeV storage ring called the Debuncher. In the Debuncher, RF bunch rotation is used to reduce the momentum spread of the antiprotons and stochastic cooling is used to reduce their transverse emittance. The $\bar{p}$'s circulate in the Debuncher for 3 seconds before being transferred to the Accumulator storage ring. Here the particles are cooled further and added to the "stack" of stored antiprotons. The Debuncher, Accumulator, and target area together form the Antiproton Source. The layout of the Antiproton Source is shown in Figure 2.2. The antiproton production rate is typically about 2×10^{10} $\bar{p}$'s stacked in the Accumulator per hour.

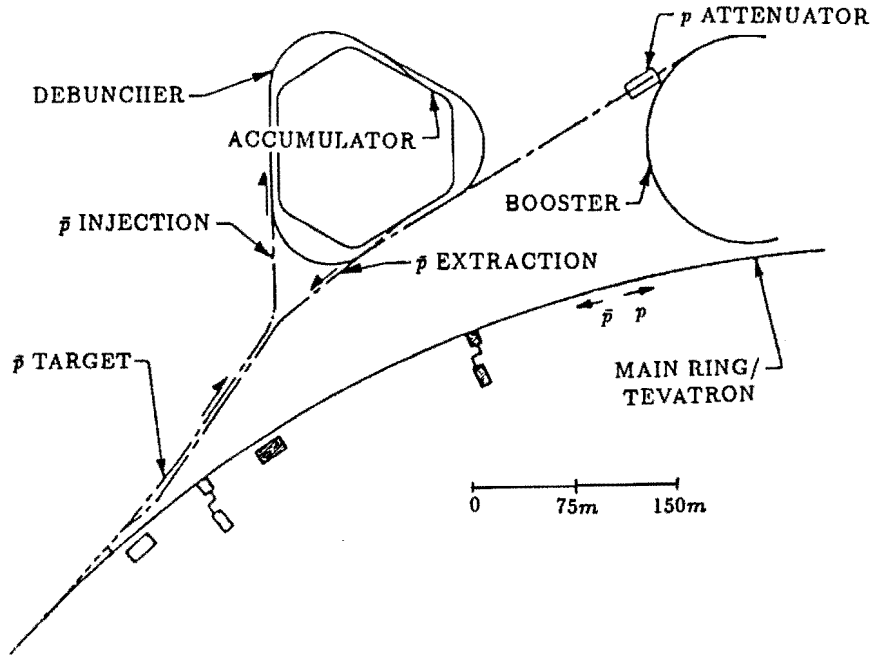

Figure 2.2: The Antiproton Source.

2.1.3 Collider Operation

When the stack contained enough antiprotons (about 6×10^{11}), the Tevatron was made ready for colliding beams. The proton bunches were inserted first. Once the proton bunches were circulating successfully, the antiprotons were extracted from the Accumulator, accelerated to 150 GeV and coalesced in the Main Ring, and then injected into the Tevatron. The six p and six $\bar{p}$ bunches intersected at 12 points around the ring. The next step was to adjust the azimuthal coordinates of the RF buckets so that the intersection points were at the positions of the collider experiments. This procedure was known as "cogging". After cogging was complete, the Tevatron was ramped to 900 GeV. The low beta quadrupoles in the B0 collision hall were then energized. These magnets squeezed the beams to

the smallest possible cross section in order to increase the rate of $p\bar{p}$ interactions. This corresponded to beams around 60 μm wide. The beams were then scraped to remove "beam halo", stray particles outside of the bunches. The beams would then coast in the Tevatron for 15 hours or more, with the bunches crossing every 3.5 μs. Typical values for the number of particles per bunch were 7×10^{10} for the protons and 3×10^{10} for the $\bar{p}$'s. The luminosity, $\mathcal{L}$, is given by

$$\mathcal{L} = \frac{N_p N_{\bar{p}} f}{4\pi\sigma_x\sigma_y}$$

where N_p and $N_{\bar{p}}$ are the numbers of protons and antiprotons per bunch, f is the crossing frequency (286 kHz), and σ_x, σ_y are the orthogonal rms widths of the beam in a plane perpendicular to the beam direction ($\sigma_x = \sigma_y = 60$ μm). For the bunch multiplicities quoted above, this formula gives $\mathcal{L} = 1.3 \times 10^{30}$ cm^{-2}s^{-1}.

2.2 The CDF Experiment

The Collider Detector at Fermilab (CDF) is a 5000 ton, azimuthally symmetric detector built to study $p\bar{p}$ collisions at the Fermilab Tevatron. A perspective view of the apparatus is shown in Figure 2.3, and an elevation view of the forward half of the detector is shown in Figure 2.4. In this section we describe features of the CDF detector that are relevant to this study. More detailed descriptions are available elsewhere [16]. We also describe the CDF trigger system, and the missing E_t trigger used to collect the monojet data.

The CDF detector coordinate system has its origin at the center of the detector

with the $+y$-axis vertically upward and the $+z$-axis along the proton direction. The usual azimuthal and polar angular coordinates are denoted by φ and θ. Psuedorapidity, $\eta = -\ln\tan(\theta/2)$, is usually used to specify polar angle.

2.2.1 Tracking Detectors

CDF used two systems for charged particle tracking, the Vertex Time Projection Chambers (VTPC) and the Central Tracking Chamber (CTC). To measure the momenta of charged particles, the chambers were placed within a superconducting solenoid that provided a magnetic field of 1.4 T.

2.2.1.1 The Vertex Time Projection Chambers

The VTPC system [17] immediately surrounded the beam pipe at the interaction region. These chambers provided charged particle tracking down to $\theta = 3.5°$ ($|\eta| < 3.5$). The z coordinate of the interaction vertex was measured by the VTPC, with an rms resolution of 1 mm. For this study, VTPC tracking was also used to help identify QCD jet background.

The VTPC system consisted of eight octagonal time projection chambers. Two such modules are illustrated in Figure 2.5. Each chamber was divided into two 15.25 cm long drift regions by a central high voltage grid. The chambers were filled with a 50-50 argon-ethane gas mixture. Charged particles passing through the gas left trails of electrons and ionized molecules. The electrons drifted in the electric field to the ends of the chambers. At the ends of each chamber was

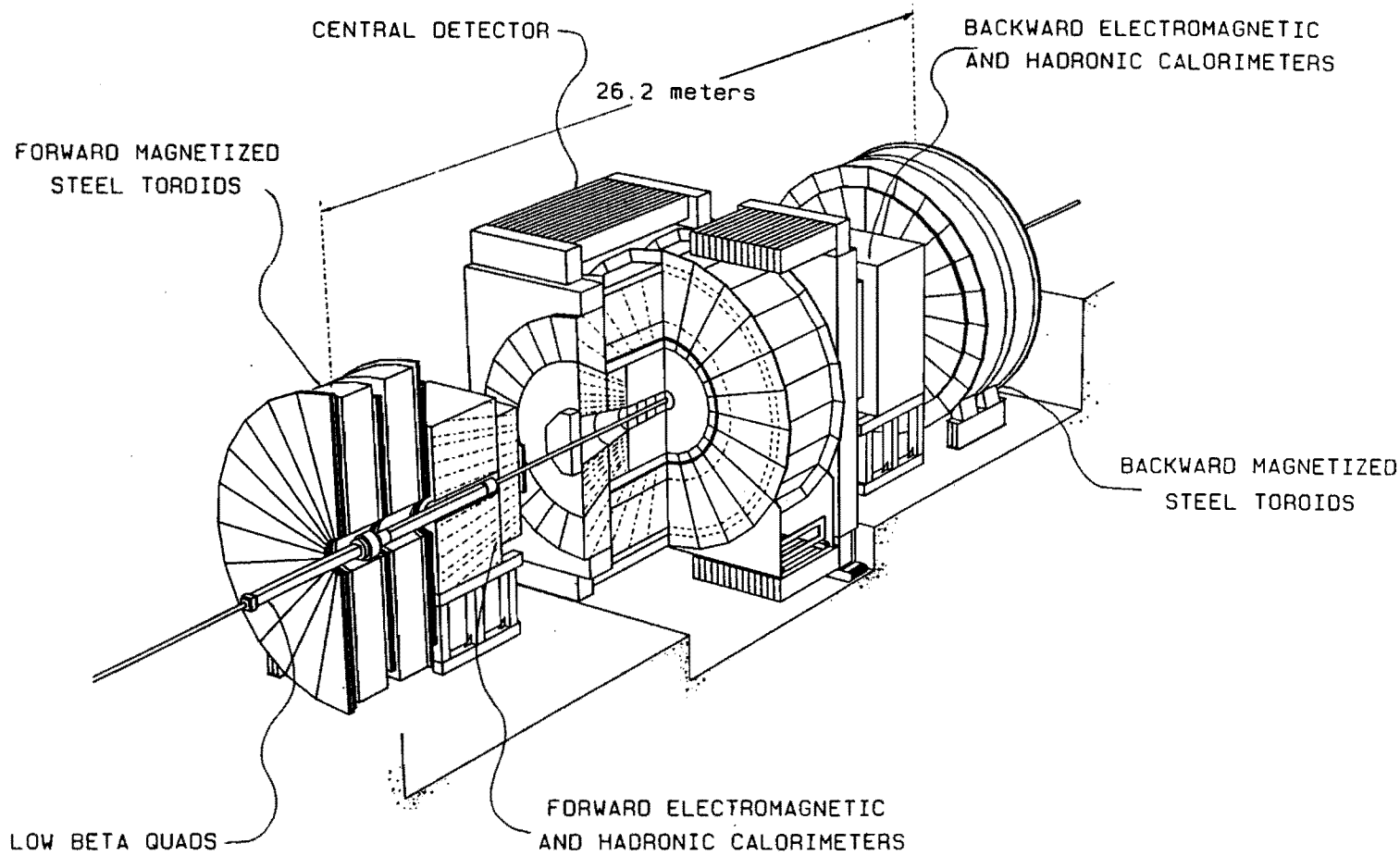

Figure 2.3: A perspective view of the CDF detector.

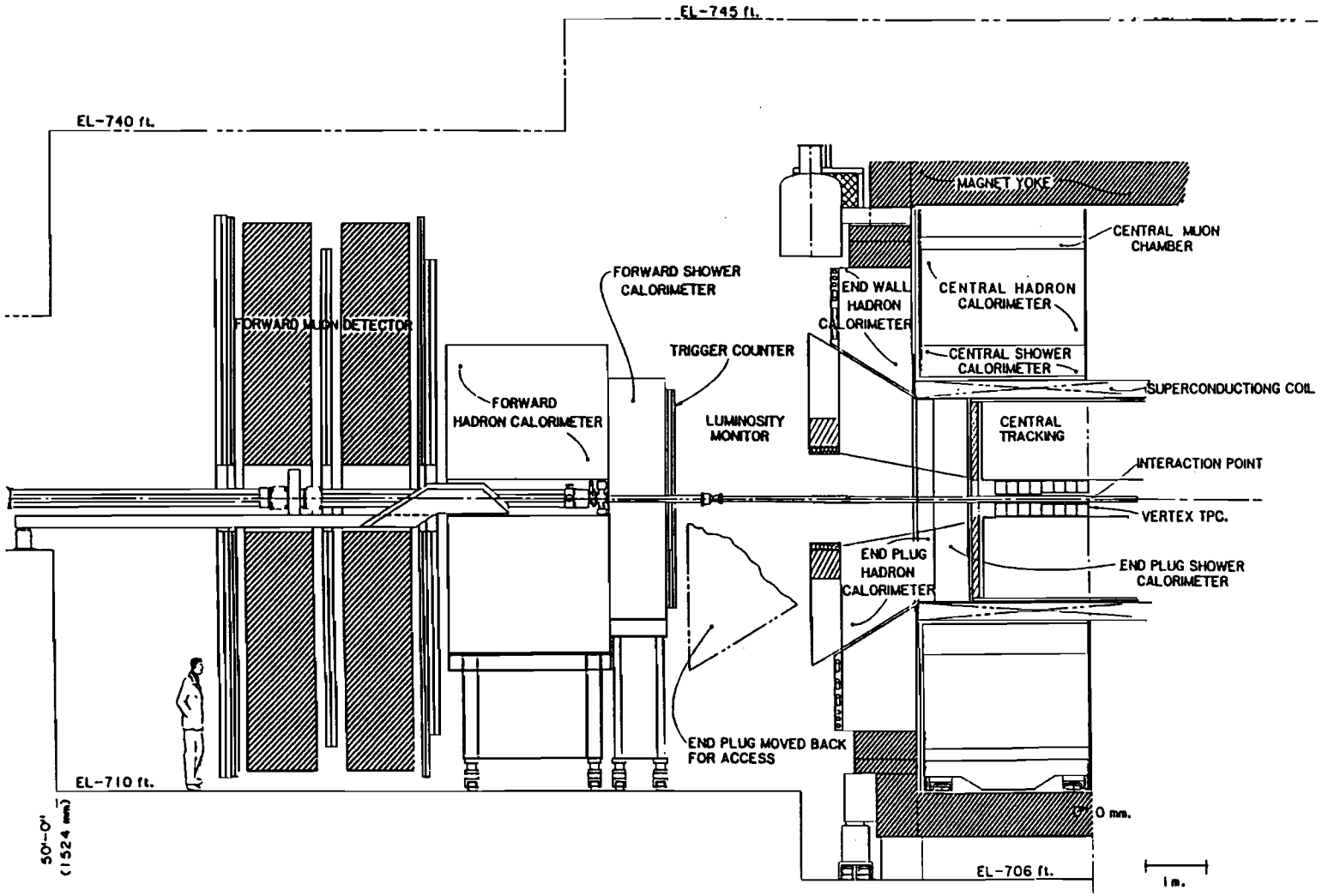

Figure 2.4: The CDF detector as it was used during the 1988-89 run.

proportional regions divided into octants, with 24 sense wires and 24 cathode pads in each octant. Drift time measurements from the sense wires provided tracking information in the r-z plane, and signals from the pads provided φ information. Adjacent modules were rotated by 11.3° with respect to each other. This allowed a stereo view of tracks that passed through more than one chamber. The z resolution deteriorated with decreasing polar angle; at $\theta = 90°$ ($\eta = 0$) the resolution was 420 μm, and at $\theta = 11°$ ($\eta = 2.3$) it was 1100 μm. The pad $r\varphi$ resolution was 418 μm.

Tracks found by the VTPC pattern recognition code had three levels of φ information:

- The track could consist only of a set of wire hits in a single octant, without pad information. In this case, the φ coordinate was known only to within the width of an octant (45°).
- The track could lack pad information but pass through more than one chamber, so that a three dimensional stereo reconstruction was possible.
- The track could possess both wire and pad information.

We refer to tracks in the first category as two-dimensional or "octant" tracks. About 35% of the tracks identified in the VTPC were of this type. Another 15% of the tracks had φ information only from a stereo view, and the remaining 50% had a full three-dimensional reconstruction from both wires and pads.

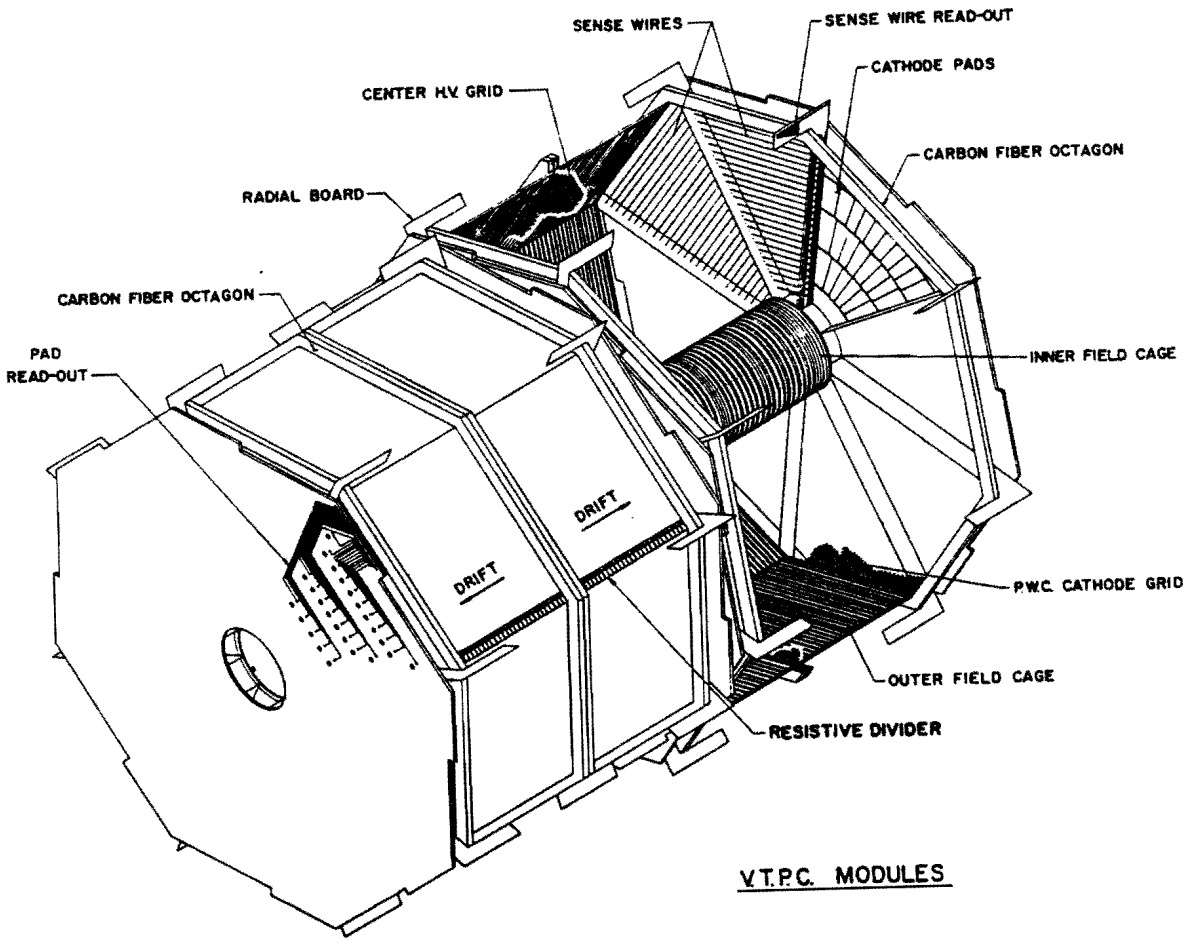

Figure 2.5: Two of the eight Vertex Time Projection Chamber (VTPC) modules.

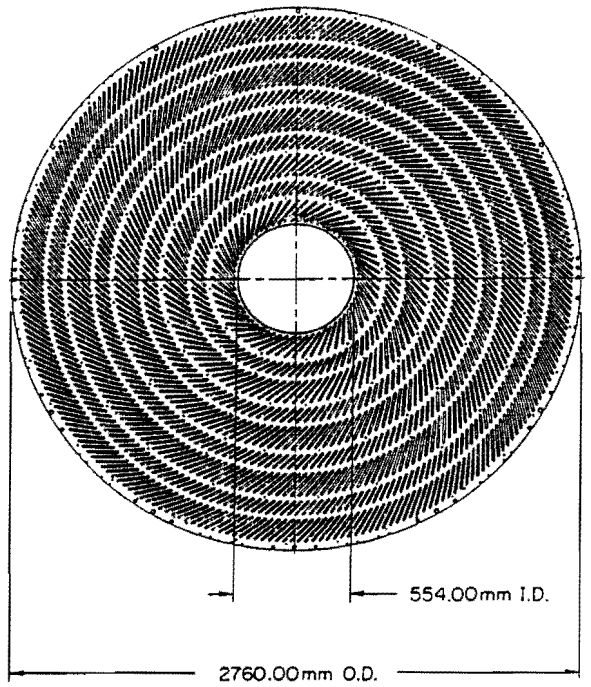

Figure 2.6: End view of the CTC.

2.2.1.2 The Central Tracking Chamber

Outside of the VTPCs was the Central Tracking Chamber [18]. The CTC was a cylindrical drift chamber 3.2 m in length and 2.76 m in diameter. It had 84 layers of sense wires grouped in 9 superlayers. Five of the superlayers had sense wires parallel to the beam axis, and provided tracking information in the r-φ plane. In between these axial superlayers were four superlayers whose sense wires were tilted alternately $\pm 3°$ with respect to the beam axis. These superlayers provided three dimensional stereo views of the tracks. An r-φ view of the CTC, showing the nine superlayers, is shown in Figure 2.6.

Each superlayer was divided into drift cells consisting of a row of sense wires flanked by two rows of field wires. There were 12 sense wires per cell in the axial

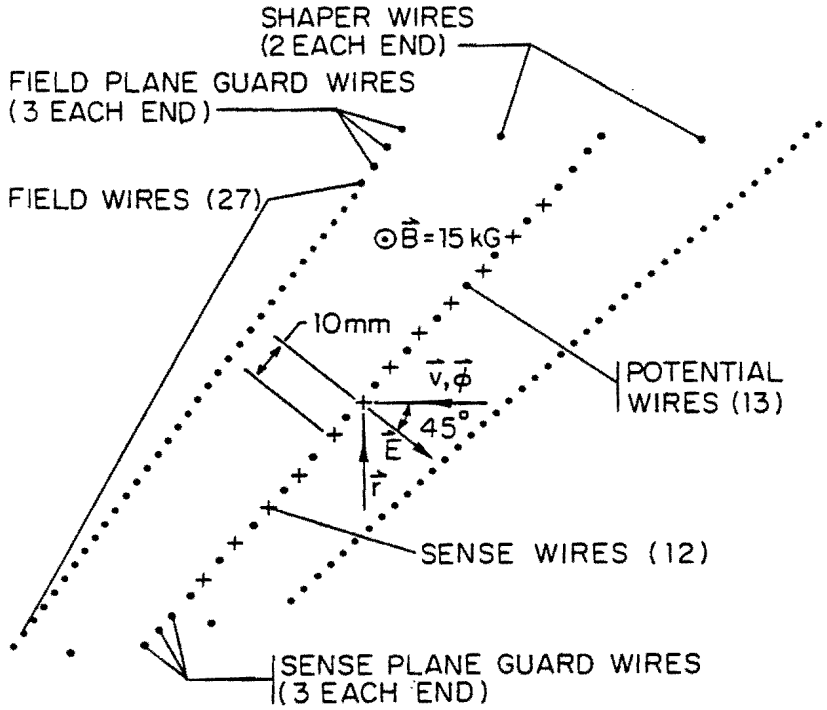

Figure 2.7: Wire geometry for an axial drift cell in the CTC.

superlayers and 6 sense wires per cell in the stereo superlayers. An axial drift cell is illustrated in Figure 2.7. The cells were tilted by 45° with respect to the radial direction. This large tilt angle had several advantages. It simplified the problem of resolving the left-right ambiguity in the drift direction, it guaranteed that each high-p_t track passed near at least one sense wire in every superlayer (useful in triggering), and it produced approximately azimuthal drift trajectories in the presence of crossed electric and magnetic fields.

By using the CTC to determine the radius of curvature of a track in the magnetic field, the transverse momentum p_t could be measured with an rms resolution of $\delta p_t/p_t = 0.0020 * p_t$ (p_t in GeV). If the track was also constrained to pass through a point on the beam axis, the momentum resolution was improved to $\delta p_t/p_t = 0.0011 * p_t$. Momentum resolution and tracking efficiency were degraded

outside of the region $40° < \theta < 140°$ ($|\eta| < 1.0$) since lower angle tracks did not pass through all the superlayers. The nominal region in which CTC tracking was useful was $|\eta| < 1.1$.

2.2.2 Calorimeters

The CDF calorimetry was divided into three systems: Central/Endwall [19],[21], Plug [22], and Forward [23, 24]. The central calorimeters were four C-shaped units or "arches" that surrounded the CTC and solenoid in the region $|\eta| < 1.1$, as shown in Figure 2.3. The endwall and plug formed the magnet yoke, and extended the η coverage down to $|\eta| = 2.4$. The forward calorimeters were situated away from the central detector, and covered the small angle regions ($2.4 < |\eta| < 4.2$).

The CDF calorimetry used a projective tower geometry. Each tower subtended a solid angle of $\Delta\eta \simeq 0.1$ and $\Delta\varphi = 15°$ ($5°$) in the central (plug/forward). Transverse energy, E_t, was defined as $E \sin\theta$, where E was the energy deposited in a calorimeter tower and θ was the polar angle for the tower with respect to the event vertex.

Figure 2.8 shows a side view of a quadrant of the central, endwall and plug calorimeters. An η-φ map of the towers for a full quadrant ($\eta > 0$, $\Delta\varphi = 90°$) of the hadron calorimetry is shown in Figure 2.9. This map shows the small angle regions not covered by the hadron calorimeters because of the space required by the low beta quadrupoles. The φ coverage of the EM calorimeters is complete

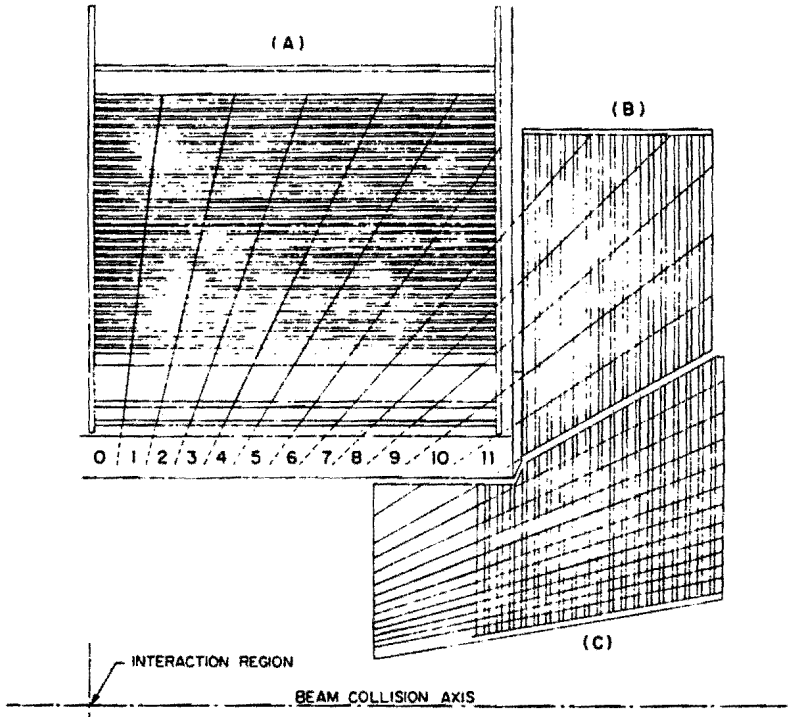

Figure 2.8: Quadrant of the calorimeter where A, B, C show central, endwall and plug respectively.

out to $\eta = 4.2$.

2.2.2.1 The Central and Endwall Calorimeters

The central arches contained 48 calorimeter modules. Each module was in the shape of a 15° wedge and contained 10 EM and 8 hadronic towers. The electromagnetic compartment of each wedge contained 31 sampling layers of 0.32 cm lead absorber and polystyrene scintillator. The hadronic compartment in each wedge had 32 sampling layers of 2.5 cm steel absorber and acrylic scintillator. A drawing of one of these wedges, showing the light collection system for the EM towers, is displayed in Figure 2.10. Each tower was read out by two phototubes coupled to the scintillators through waveshifters and light guides. The hadronic

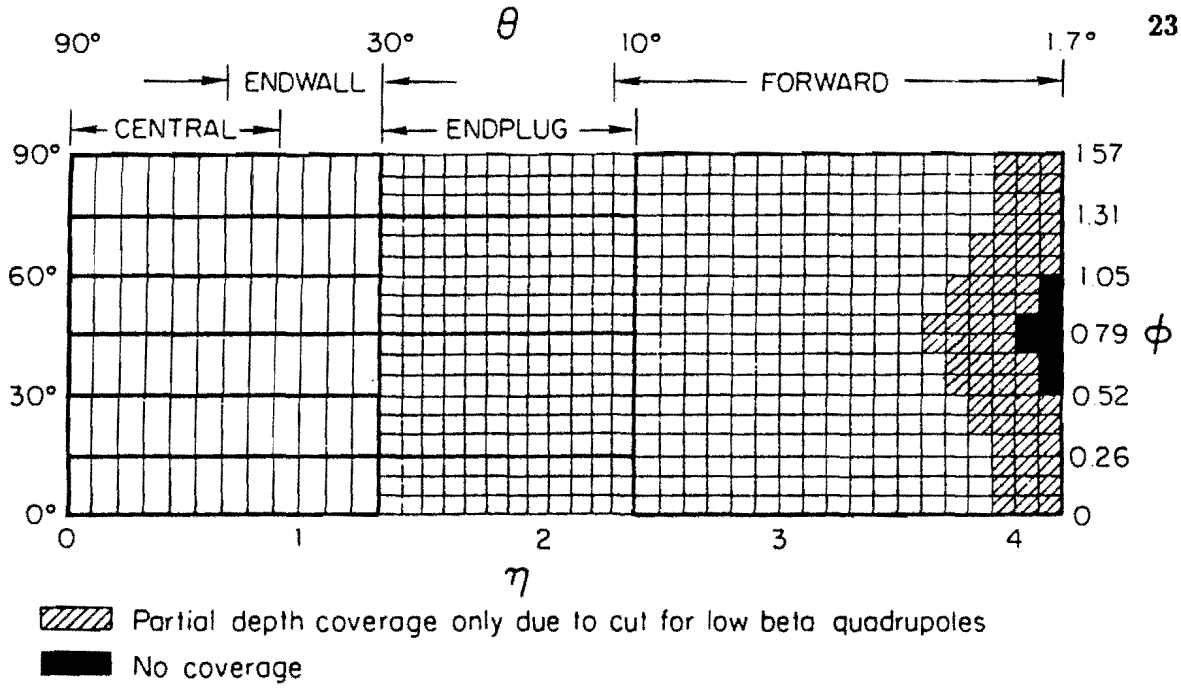

Figure 2.9: Hadron calorimeter towers in one of eight identical η-φ quadrants.

compartments for the last four towers in each wedge (numbered 6 through 9 in Figures 2.10 and 2.8) extended beyond the central arches into separate endwall modules. The endwall calorimeters had 15 sampling layers of 5.1 cm steel absorber and acrylic scintillator.

Proportional chambers called the Central Strip (CES) Chambers [20] were sandwiched in the EM calorimeter at a depth of 5.9 radiation lengths (including the solenoid coil). These chambers were constructed from ribbed aluminum extrusions with grooves 9 mm wide by 6 mm deep. Wires were strung down the center of each groove. Glued to the top of the ribs were boards of G10 with copper strips at right angles to the ribs. The chambers were filled with a 95% Ar, 5% CO_2 gas mixture and the wires were held at high voltage. A shower of particles hitting the chamber would ionize the gas mixture, producing pulses on the wires

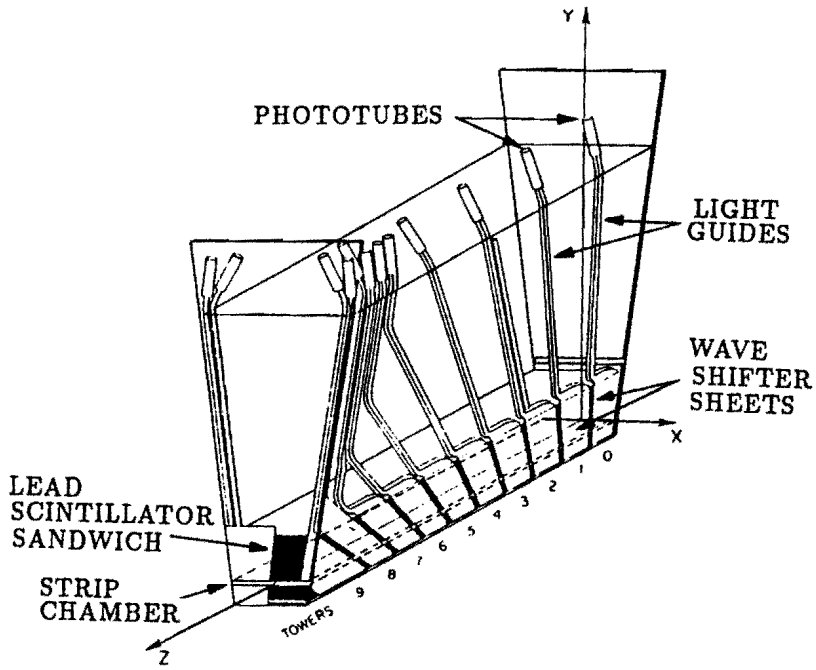

Figure 2.10: A central calorimeter wedge.

and inducing charges on the strips. Each chamber had 64 wire channels and 128 strip channels. The signals from the wires gave the r-φ coordinate of the shower centroid and the signals from the strips gave the z position. The CES chambers provided a precise measurement of the shower position (to within about ± 2 mm) and its transverse dimensions.

The energy resolution of the central EM calorimeters was given by $13.5\%/\sqrt{E}$ (E in GeV.) For the central and endwall hadron calorimeters the resolutions were given by $77\%/\sqrt{E}$ and $98\%/\sqrt{E}$ respectively.

2.2.2.2 The Gas Calorimeters

The plug calorimeters used layers of absorber and proportional tubes. The plug EM (PEM) calorimeters had 34 sampling layers with 0.27 cm lead absorber,

and the plug hadron (PHA) calorimeters had 20 sampling layers with 5.1 cm steel absorber. The forward EM and hadron calorimeters were gas-tube calorimeters very similar in design to the plug calorimeters. The forward EM (FEM) calorimeters had 30 sampling layers and used 0.48 cm sheets of lead for the absorber layers. The forward hadron (FHA) calorimeters had 27 sampling layers and 5.1 cm steel absorber.

The proportional tubes used in the gas calorimeters were made of conductive plastic and had a square cross section of 8.6 mm $\times$ 8.6 mm. The tubes were filled with a 50-50 argon-ethane gas mixture. A central wire in each tube was held at high voltage. Adjacent to each layer of tubes was a sheet of copper-clad G10 that had been etched into $0.1 \times 5^\circ$ η-φ pads. Ionization in the gas produced by a shower of particles induced charges on the pads, which were digitized by the readout electronics. For the 9 layers in the plug EM calorimeters around the shower maximum (corresponding to a depth of 4.4 to 9.7 radiation lengths) orthogonal strips, instead of pads, were used. This provided better position resolution.

To provide information about the longitudinal development of showers in the plug EM calorimeters, the pads in each tower were ganged together into three depth segments. In the FEM, the pads were ganged together in in the first 15 layers and in the last 15 layers, giving two signals per tower.

The gain of the gas calorimeters depended on the density of the gas, which varied with temperature and pressure. To monitor fluctuations in the gain, a

system of small proportional tubes containing ^{55}Fe sources was installed in the calorimeter gas lines. The gain was periodically tested by measuring the 6 keV X rays from the ^{55}Fe.

The energy resolution for the plug EM calorimeters was $28\%/\sqrt{E}$ (E in GeV) and for forward EM calorimeters it was $25\%/\sqrt{E}$. The plug and forward hadron calorimeters had about the same energy resolutions, around $90\%/\sqrt{E}$.

2.2.2.3 Calorimeter Calibration

Throughout our discussion, we use the symbol $\not{E}_t$ to refer to the raw missing transverse energy as measured by the CDF calorimeters. Because of calorimeter imperfections and non-linearities, this quantity is only approximately equal to the true transverse momentum imbalance in an event. If we wish to compare the observed $\not{E}_t$ spectrum of the monojet sample to the Z^0 p_t spectrum predicted by theory, we must first apply corrections to the missing E_t to account for detector effects. The details of the $\not{E}_t$ correction technique are presented in Appendix A. To briefly summarize, it involves multiplying the observed E_t of each jet by an η dependent factor to give the E_t that would have been observed had the jet been in the central calorimeter. Therefore, to accurately determine the missing E_t we must know the energy scale of the central calorimeters.

Each one of the central and endwall calorimeter modules was calibrated in the test beam. A beam of 50 GeV electrons was used to calibrate the electromagnetic compartments, and 50 GeV pions were used to calibrate the hadronic

sections. At the same time, calibrations were performed using ^{137}Cs sources permanently attached to each module [25]. Each source was connected to a drive mechanism that allowed it to be moved through the module, testing each tower separately. During data taking, the calibration of the central calorimeter was periodically retested with the sources. The data from the sources indicate that the absolute calibration of the central hadron calorimeter (CHA) was accurate to 3-4%. Separate testing of the phototubes was also done on a regular basis, using LEDs for the tubes in the central EM (CEM) and a nitrogen laser for the tubes in the CHA. There was also a xenon flasher system to test the CEM waveshifters. These tests showed no significant degradation of calorimeter performance from radiation damage over the course of the run [26].

The calibration of the CEM was also determined from experimental data [27],[28]. The transverse energy (E_t) deposited in the calorimeters by electrons from W decays was compared to their transverse momenta (p_t) measured by the CTC. The p_t is assumed to be correct within the errors quoted in Section 2.2.1.2. A distribution of the ratio E_t/p_t is shown in Figure 2.11. It exhibits a peak around $E_t/p_t = 1$ and a long tail at higher values of E_t/p_t caused by electrons that radiate bremsstrahlung photons. This distribution was compared to Monte Carlo simulations of $W \rightarrow e\nu$. The region around the peak (typically $0.90 < E_t/p_t < 1.10$) was fitted to a gaussian and the energy scale for the CEM was adjusted until the mean of the gaussian matched the value expected from Monte Carlo. These studies showed that the CEM energy scale was known to

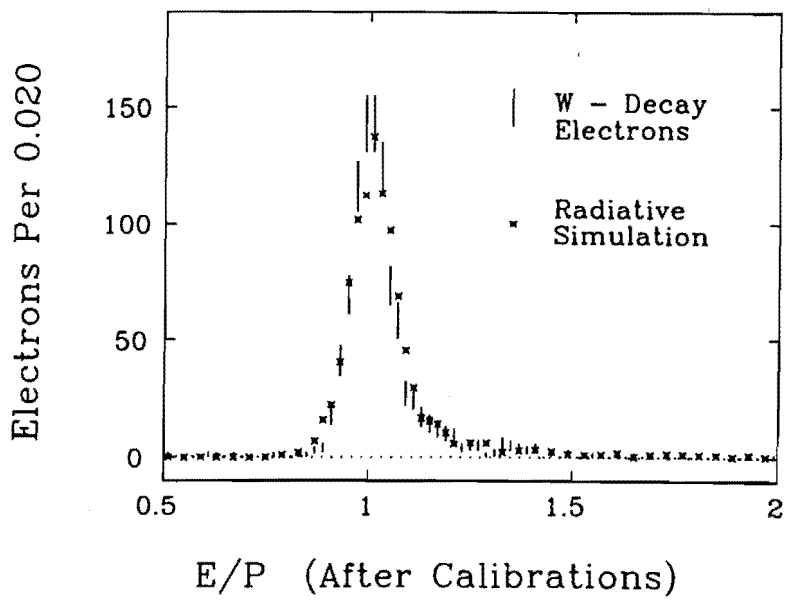

Figure 2.11: E_t/p_t distribution for W electrons.

within 4%.

2.2.3 The Central Muon System

Just outside of the 4.9 absorption lengths of the central calorimeter was the Central Muon (CMU) system [29]. Each central calorimeter wedge was equipped with three muon chamber modules as shown in Figure 2.12. Each module consisted of four layers of four rectangular drift cells. A drift cell is shown in Figure 2.13. The central anode wires ran the length of the cells (2.3 m) and field shaping was provided by the aluminum cathodes at ends of the cells. Drift time measurements from the sense wires provided r-φ information for charged particles passing through the cells. The left-right ambiguity as to which side of the wires a track passed was resolved by offsetting alternate layers of drift cells in each chamber by 2 mm in the r-φ direction relative to the layers below them. Charge division

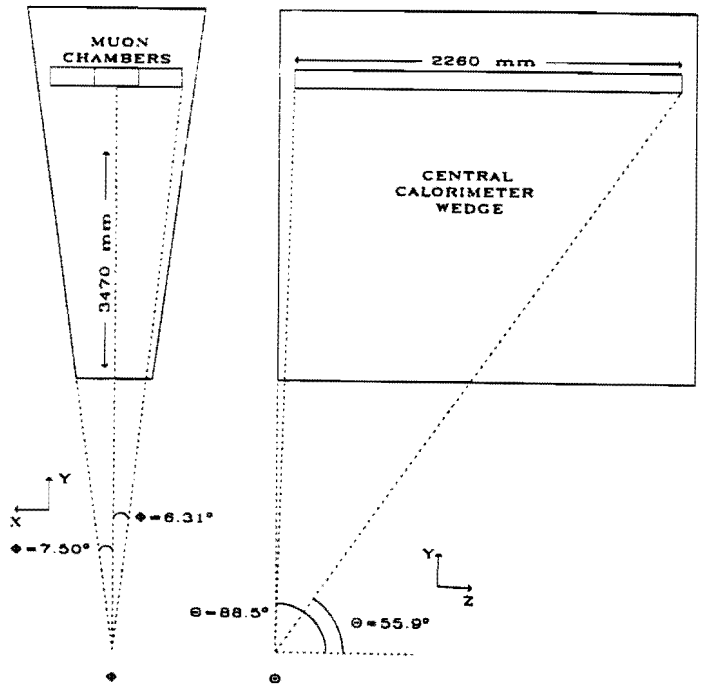

Figure 2.12: Location of the central muon chambers within a central calorimeter wedge.

was used to provide r-z information. In this technique, capacitors at each end of the wire store the charge from a pulse caused by a passing charged particle. The position of the particle along the length of the wire, z_{wire}, is given by

$$z_{wire} = (\frac{Q_L - Q_R}{Q_L + Q_R})\ell$$

where Q_L and Q_R are the amounts of charge collected at the left- and right-hand ends of the wire and ℓ is the length of the wire.

The CMU system covered the region $0.04 < |\eta| < 0.61$. The chamber resolutions were 250 μm in r-φ and 1.2 mm in z.

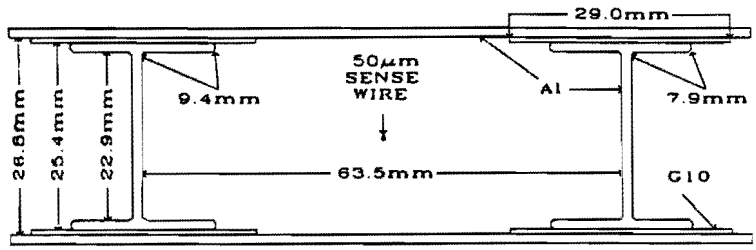

Figure 2.13: A CMU drift cell.

2.2.4 The Forward Muon System

Beyond the forward calorimeters and covering the region $2.0 < |\eta| < 3.6$ was the Forward Muon (FMU) system [30]. Each FMU unit consisted of a pair of magnetized iron toroids instrumented with drift chambers and scintillation counters. The azimuthal magnetic fields in the toroids made it possible to measure the muon momentum.

Each FMU unit had 6 planes of drift chambers and four planes of acrylic scintillators. The scintillators were used to provide a trigger signal. The chambers and scintillators were segmented into 15° slices (see Figure 2.14.) Each chamber contained two layers of 96 sense wires strung azimuthally. The separation between the wires was chosen to maintain a constant psuedorapidity interval of $\Delta\eta \simeq 0.3$ for each drift cell. The two layers of wires made it possible to resolve the left-right ambiguity in drift direction. Between the wire layers was a copper cathode plane divided into η-φ pads of size $0.35 \times 5°$.

The position resolution of the drift chambers was 650 μm. The toroidal magnetic field varied with radius, causing the FMU momentum resolution to vary slightly with polar angle. For a track entering the FMU toroids at $\theta = 10°$, the resolution was given by $\delta p/p = 16.6\%$.

2.2.5 The Beam-Beam Counters

The Beam-Beam Counters (BBC's) were positioned on either side of the central detector, just in front of the forward EM calorimeters (see Figure 2.4). These were planes of scintillators and phototubes, illustrated in Figure 2.15. The BBC's served two important functions: they provided a minimum bias trigger and measured the beam luminosity. The trigger required that there be at least one hit recorded in each forward and backward BBC array within a 15 ns time window centered on a beam crossing. The luminosity is given by

$$\mathcal{L} = \frac{R}{44 \text{ mb}}$$

where R is the rate of $p\bar{p}$ interactions measured by the BBC's and 44 mb is the BBC cross section. The BBC rate is typically around 60 kHz. The uncertainty in the luminosity measurement is 7% [31].

2.2.6 The Trigger

CDF used a three-level FASTBUS based trigger system [32]. The lowest trigger level was Level 0. Events passing this level had hits recorded in forward

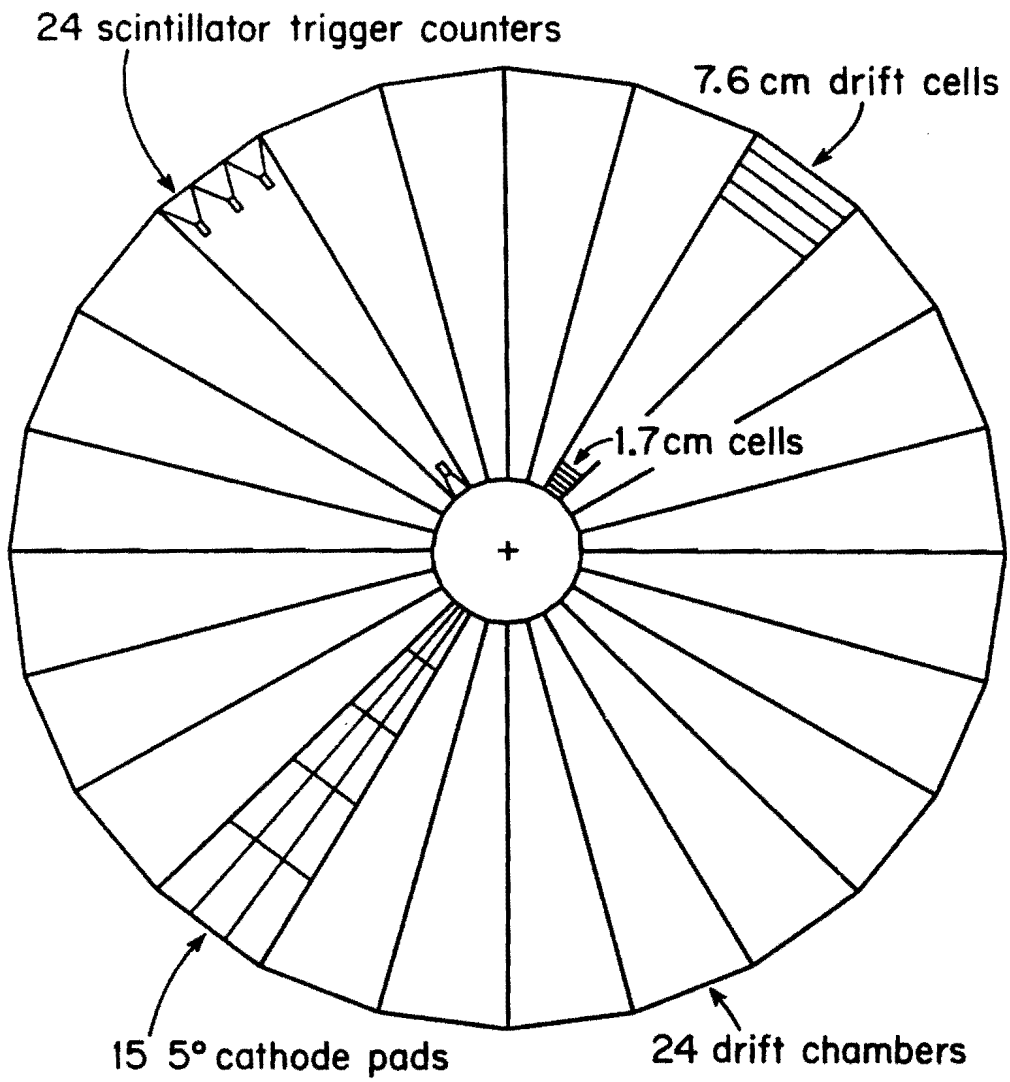

Figure 2.14: r-φ view of one of the FMU planes.

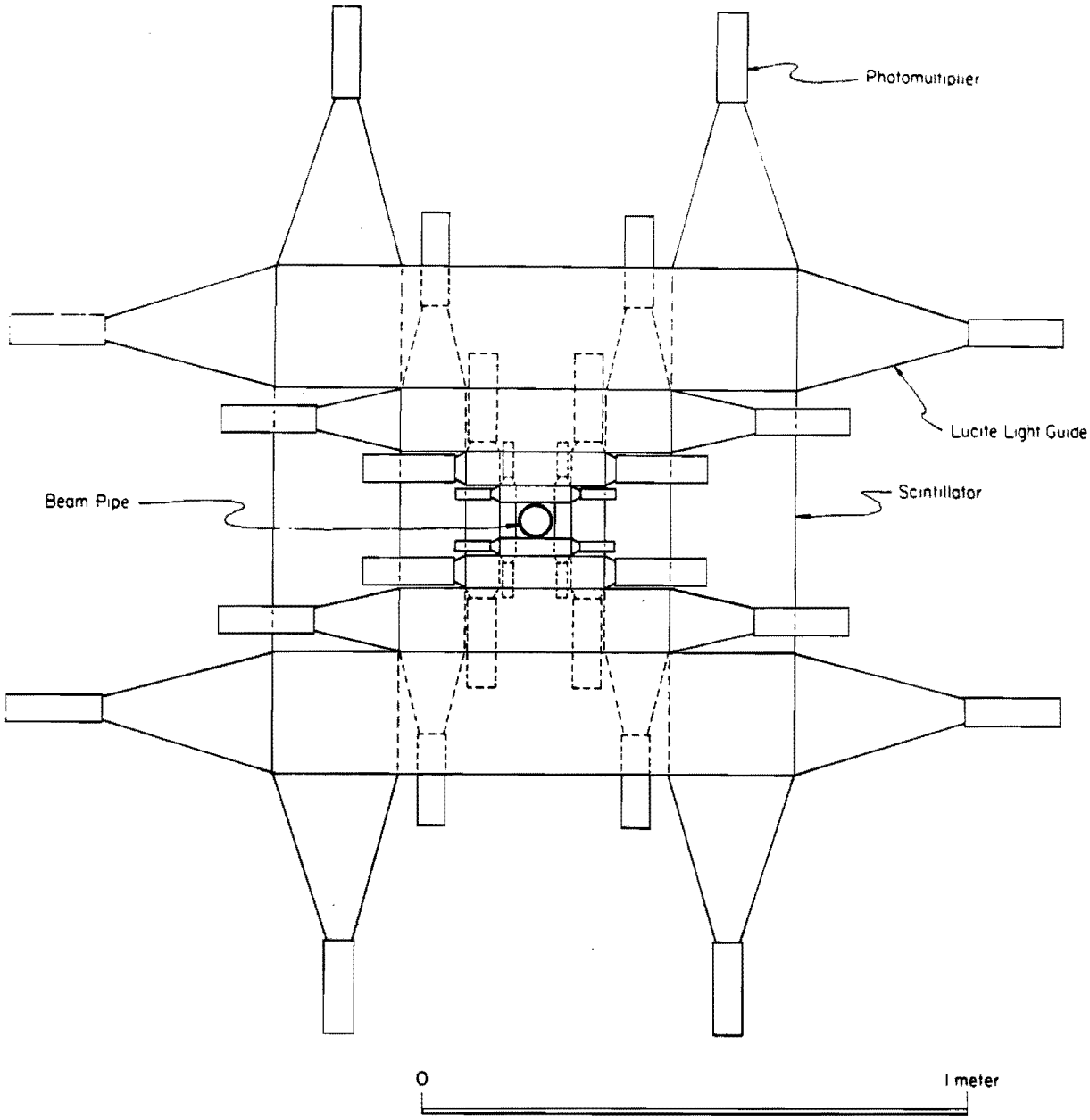

Figure 2.15: r-φ view of one of the Beam-Beam Counter planes.

and backward BBC's, as described above. The Level 1 trigger decision was based on the global energy deposition in the calorimeters and data from the muon system. An event passed Level 1 if the scalar sum of the E_t over all calorimeters was above a certain threshold, or if there were muon candidates in the muon chambers. The time required to make a Level 1 decision was greater than the interval between beam crossings (3.5 μs), so that one crossing was lost for every Level 0 trigger. The next trigger level, Level 2, required about 10 μs to make a decision. If the decision was made to record the event, the data acquisition system required about 15 ms to read out all the detector components. The trigger rate was ultimately limited by the rate at which events could be written to magnetic tape, around 1 Hz.

There were a variety of Level 2 triggers, each designed for a specific physics analysis. This study is based upon events which passed the Level 2 Missing E_t trigger. Events which came in on this trigger satisfied the following requirements:

- $\not{E}_t \geq 25$ GeV, summed over all calorimeter components. The trigger hardware calculated the $\not{E}_t$ assuming an event vertex at $z = 0$. In the offline analysis, the $\not{E}_t$ was recalculated using the event vertex determined from the VTPC data.

- The calorimeter cluster with the greatest E_t (the "leading cluster") had at least 8 GeV deposited in the EM calorimeters.

- The leading cluster could not have a "seed tower" (a tower with $E_t \geq 3$

GeV, used by the clustering algorithm to initiate cluster formation) in the forward calorimeters.

The last two requirements were imposed to reduce the rate of spurious triggers caused by detector noise.

To estimate the efficiency of the $\not{E}_t$ trigger, we studied a sample of events that passed a separate Level 2 trigger. This trigger required a single cluster with $E_t > 60$ GeV. The events in our sample were required to satisfy the second and third requirements listed above. The $\not{E}_t$ distribution for this sample was plotted on a histogram, and the fraction of the events in each $\not{E}_t$ bin that passed the Level 2 $\not{E}_t$ trigger was identified as the $\not{E}_t$ trigger efficiency for that bin. The results are summarized in Figure 2.16. Also shown in Figure 2.16 is the empirical fit to the data used to estimate the trigger efficiency in Monte Carlo simulations. The fit is a cubic polynomial for $\not{E}_t < 35.3$ GeV, and a straight line for $\not{E}_t > 35.3$ GeV. The linear fit reaches 100% at $\not{E}_t = 126.4$ GeV, and we assume that the trigger is 100% efficient beyond this point. From the statistical errors on the data points used in the fit, we calculate that the absolute error on our trigger efficiency estimate is not greater than $\pm 1\%$.

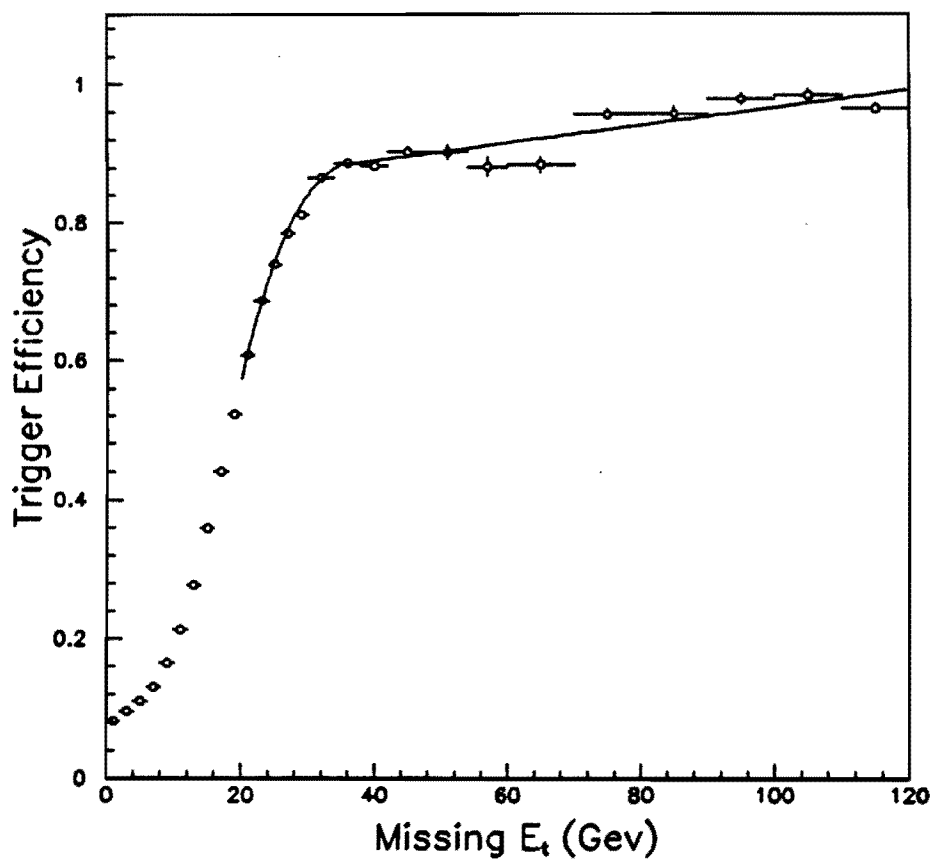

Figure 2.16: The $\not{E}_t$ trigger efficiency (circles) and the fit used in Monte Carlo simulations.

Chapter 3

Event Selection

This analysis is based on 4.7 pb^{-1} of data collected during the CDF 1988-89 run. These data consist of about 4×10^6 events written to tape. In this chapter we describe the procedure used to filter $Z^0 \rightarrow \nu\bar{\nu}$ candidates from this data set. We first describe the cuts used to isolate events containing a high-E_t jet and significant missing E_t . We then present a list of all the possible sources of monojet backgrounds, and describe further cuts designed to reduce the contribution from each source of background.

3.1 The Primary Data Sample

The selection process began with a subset of the data containing events that passed at least one of several Level 2 triggers. These included triggers for high-E_t jets, electrons, and photons, and the Missing E_t trigger. These data represent about half of the total CDF data set. In the steps described below, the other

triggers were processed along with the Missing E_t triggers. Only in the final stage of the selection process were the $\not{E}_t$ triggers separated from the other events.

We first removed from the sample events that were likely to be cosmic rays. We rejected events that had more than 8 GeV of energy in the central hadron calorimeters outside of a time window of -20 ns $< \Delta t <$ 35 ns (-25 ns $< \Delta t <$ 55 ns for the endwalls) relative to the beam crossing. About 3% of the events failed this cut.

To isolate events with substantial missing E_t, we discarded events that had any of the following characteristics:

- $\not{E}_t < 30$ GeV.

- $\sigma_{\mathrm{MET}} < 2.4$ GeV$^{\frac{1}{2}}$. The quantity σ_{MET} is called the missing E_t significance and is defined by

  $$\sigma_{\mathrm{MET}} \equiv \frac{\not{E}_t}{\sqrt{\sum E_t}}$$

  where $\sum E_t$ is the scalar sum of E_t over all calorimeters. The $\not{E}_t$ significance is proportional to the ratio of the missing E_t to the error on the measurement of the total E_t in the event. A histogram of σ_{MET} for CDF minimum bias events is shown in Figure 3.1. For these events, the true $\not{E}_t$ should be zero. A value of $\sigma_{\mathrm{MET}} = 2.4$ GeV$^{\frac{1}{2}}$ is greater than the mean value observed in minimum bias events by more than 6 standard deviations. This cut eliminated many mismeasured QCD jet events.

- There was a cluster with $E_t > 5$ GeV within a 30° wedge opposite in φ to

the leading cluster. This cut removed most of the background from dijet events in which one jet was poorly measured.

- The E_t of the leading cluster was less than 15 GeV.

These cuts yielded a sample of about 2×10^4 events. To enhance our signal to noise ratio, we further rejected events that met any of these conditions:

- The leading cluster was outside of the central region ($|\eta| > 1.2$).
- The scalar sum of the transverse momenta of the charged particles associated with the leading cluster was less than 10% of the E_t of the cluster. The particles associated with a jet were those whose tracks were measured by the CTC to be in a cone of radius 0.7 in η-φ space centered on the energy centroid of the cluster. This cut eliminated most of the remaining cosmic ray and beam gas events.

About 5000 events survived these cuts. To select those events with a single jet, we also discarded events that satisfied any of the following criteria:

- The leading cluster had an EM fraction less than 0.1 or greater than 0.85. The EM fraction was defined as the ratio of the E_t in the electromagnetic calorimeters to the E_t in the hadronic calorimeters. Detector noise was removed by the lower bound on the EM fraction, and $W \rightarrow e\nu$ events were rejected by the upper bound.
- There was more than one cluster with $E_t > 15$ GeV.

These cuts produced a sample of 815 events. We then removed from the sample events in which the z position of the event vertex was more than 60 cm from the center of the detector. The distribution of the vertices for all events was closely approximated by a gaussian with width 31 cm. This cut improved the hermeticity of the detector. Some events were found to contain two vertices, with one vertex far from the center of the detector. These events were rejected as well. 571 events survived these cuts.

Finally, we rejected events that did not come in the Level 2 Missing E_t trigger. As described above, the average efficiency for this trigger was measured to be 89% for events with $\not{E}_t > 30$ GeV. We are left with 510 monojet candidates.

3.2 Sources of Background

The signal from the process $Z^0 \rightarrow \nu\bar{\nu}$, with the Z^0 recoiling off a jet in the central region of the detector, should be contained in the sample of events that survived the above cuts. However, the sample also contains events produced by other processes that only mimic monojets. We list here the possible monojet backgrounds:

- Decays of the W boson. Each decay mode can be mistaken for a monojet in the following ways:
  - $W \rightarrow e\nu$, where the W is accompanied by a jet and the electron has escaped detection.

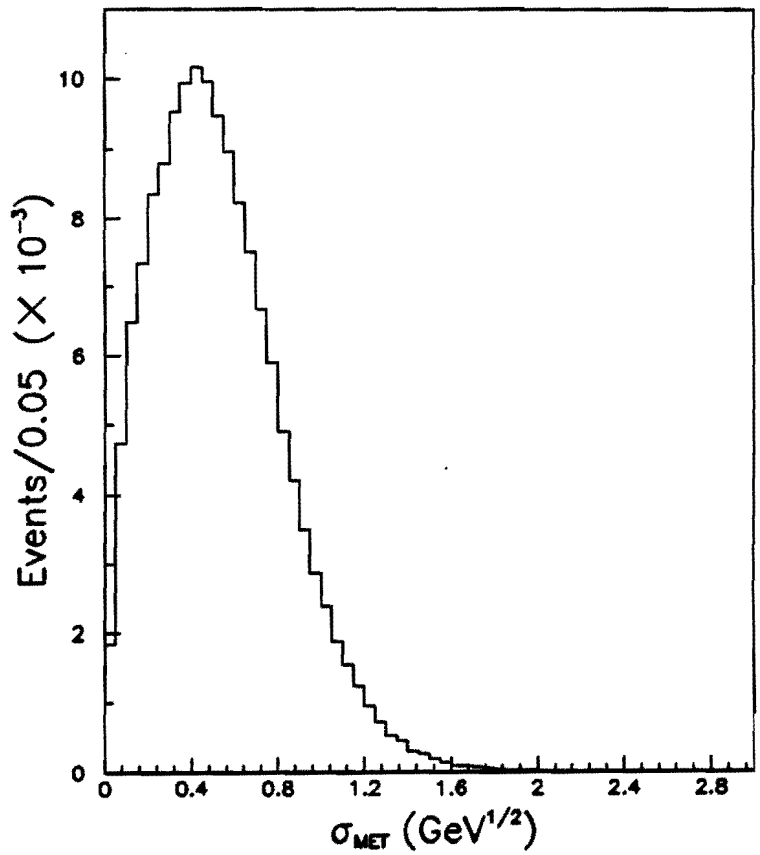

Figure 3.1: The missing E_t significance (σ_{MET}) for a sample of CDF minimum bias events.

- $W \rightarrow \mu\nu$, where the W is accompanied by a jet and the muon has escaped detection.
- $W \rightarrow \tau\nu$, where the W is accompanied by a jet and the tau has escaped detection.
- $W \rightarrow \tau\nu$, where the decay of the τ lepton into hadrons is mistaken for a monojet.

- Decays of the Z^0 boson into charged leptons, where the Z^0 recoils off a jet and both leptons have escaped detection.
- Decays of the Z^0 boson into a $\tau^+\tau^-$ pair, where one tau was undetected and the other mistaken for a jet.
- QCD jet events in which the jet activity has been poorly measured.
- Events of the type $p\bar{p} \rightarrow \gamma$+jet, in which the photon has not been detected.
- Cosmic ray and beam gas events.

Each source contributes events which can be individually identified and removed from the data sample. The identification procedures are described below, and their effects are summarized in Table 3.1. Table 3.1 lists the cuts in the order in which they were made. There were some events that would have failed more than one cut, so that if the cuts had been made in a different order the number of events rejected by each cut would have varied slightly.

There remains in the data a residual background from each source which must be estimated separately and subtracted statistically. These analyses, which rely on both studies of CDF data and Monte Carlo techniques, are described in the following chapters.

3.3 Tau Cuts

A τ lepton has a 64% chance of producing one or more charged hadrons when it decays. When a daughter τ from a W boson decays hadronically, the energy cluster produced in the calorimeters is very similar to a jet resulting from parton fragmentation. But in the lab frame the τ secondaries will be confined to a narrow cone, and the vast majority (99.8%) of these decays produce only 1 or 3 charged particles. Hence, an apparent monojet with a small angular width and three or fewer stiff tracks is the signature of a τ decay.

The identification of τ candidates began by selecting CTC tracks with $p_t \geq 5$ GeV that pointed to within 5 cm of the event vertex. These tracks were used as seeds for track clustering. Clustering began with the highest p_t track seed. Tracks were included in a cluster if they had $p_t \geq 1$ GeV, were within 30° of the seed track, were no more than 5 cm in the z direction from the seed track when both tracks were closest to the z axis, and were not already included in another τ cluster. The E_t for each τ cluster was then calculated by summing the energy in a region 2 towers wide in φ by 6 towers in η ($30° \times 0.6$) centered on the seed

track.

Events were rejected if they contained a τ candidate that satisfied the following criteria:

1. 10 Gev $< E_t <$ 55 GeV. Monte Carlo studies indicate that there should have been no taus with $E_t > 55$ GeV.

2. 3 or fewer tracks within a cone of half angle 10° centered on the seed track.

3. No additional tracks were outside of the 10° cone and within a 30° cone centered on the seed track.

These cuts rejected 135 events.

3.4 Muon Cuts

Our data set included events of the type $W \rightarrow \mu\nu$ where the W boson recoiled off a high-p_t parton. We could reject these events if the muon was identified by the muon system or if it had a well-reconstructed track in the CTC. Smaller sources of backgrounds are the processes $p\bar{p} \rightarrow Z^0 + \text{jet}$; $Z^0 \rightarrow \mu^+\mu^-$ and $p\bar{p} \rightarrow W + \text{jet}$; $W \rightarrow \tau\nu$; $\tau \rightarrow \mu\nu_\mu\nu_\tau$. Our cuts tended to reject these events as well.

Our criteria for a particle detected by the CMU system to be a W muon candidate were:

1. $p_t > 5$ GeV, where p_t is measured by the CTC.

2. $E_{EM} < 2$ GeV and $E_{Had} < 6$ GeV, where E_{EM} and E_{Had} are the energies deposited in the electromagnetic and hadronic calorimeters in an η-φ cone of radius 0.13 around the muon. This cut suppressed hadronic punch-through.

3. The E_t deposited in a cone of radius 0.4 minus the E_t in a cone of radius 0.13 around the muon could not exceed 5 GeV. This cut required the lepton to be isolated.

4. A spatial match was required between the CTC track and the track stub reconstructed in the muon chambers.

It was possible for a W muon to be in the central region of the detector and to miss the CMU system. In this case, the high-p_t track produced by the muon in the CTC was the evidence we could use to reject the event. Therefore, we discarded events containing one or more CTC tracks with $p_t > 10$ GeV that met conditions (2) and (3) above. We refer to these CTC tracks as Central Minimum Ionizing Objects (CMIO's).

The muon cuts rejected 109 events. Of these, 39 were detected as muons by the CMU chambers, and 70 were identified as CMIO's.

3.5 Electron Cuts

As we mentioned previously, we required the leading cluster in each event to have no more than 85% of its E_t in the electromagnetic compartment of the calorimeter. This removed most of the events in which a W decays into an electron

and a neutrino. However, we also applied additional cuts to further reduce the background from $W \rightarrow e\nu$ events. These cuts also eliminated events containing daughter electrons from taus produced in $W \rightarrow \tau\nu$ events.

Electron identification was based on energy clusters found in the electromagnetic calorimeters. Towers which contained at least 3 GeV electromagnetic E_t were used as seed towers for clustering, and towers were included in a cluster if their electromagnetic E_t was at least 0.1 GeV. Limits were placed on the size of the clusters. In the central region, an electron cluster could consist of no more than 3 towers: the seed tower, and the two towers adjacent in η. In the plug, the maximum size of a cluster was 5 towers in η by 5 towers in φ centered on the seed tower, and in the forward it was 7 towers by 7 towers. Each cluster was required to have a total E_t of at least 5 GeV and to have an EM fraction no less than 0.875.

Events were eliminated from the sample if they contained a central electron candidate that satisfied these criteria:

- $E_t > 10$ GeV.
- LSHR < 0.25. LSHR is a measure of the deviation of the lateral profile of the electromagnetic shower from the shape observed with 50 GeV test beam electrons. LSHR is defined as:

$$\mathrm{LSHR} = 0.14 \sum_i \frac{E_i - T_i}{\sqrt{0.14^2 E_{clus} + (\Delta T_i)^2}}$$

where the sum is over towers adjacent to the seed tower and

E_i = Electromagnetic energy in the ith tower.

T_i = Expected EM energy from test beam studies.

E_{clus} = Total electromagnetic energy in the 3 tower cluster.

ΔT_i = Uncertainty in T_i associated with a 1 cm error in the z coordinate of the electron impact point.

The LSHR distribution for a sample of W electrons is shown in Figure 3.2. This plot shows that virtually all central electrons from W decays will fail this cut [33].

- $E_t/p_t > 0.3$. E_t is the transverse energy of the cluster and p_t is the transverse momentum of the stiffest track pointing to the cluster.
- $\Delta z < 3$ cm and $\Delta(r\varphi) < 3$ cm. Δz and $\Delta(r\varphi)$ are the distances between the extrapolated track and the shower position measured by the CES chamber.
- The lateral and transverse profiles of the shower measured by the CES chamber were similar to the average shower profiles observed for testbeam electrons. The exact cut was

$$\frac{1}{2}(\chi^2_{r\varphi} + \chi^2_z) < 20.$$

The quantities $\chi^2_{r\varphi}$ and χ^2_z are defined by

$$\chi^2 = \frac{1}{4}\sum_i \frac{[y_i - t_i]^2}{\sigma_i^2}$$

where the sum is over the CES strip or wire channels and

y_i = Measured profile (either strip or wire), normalized to unity.

t_i = Profile observed for testbeam electrons.

σ_i = Estimated variance of the profile.

In Figure 3.3 we display the CES χ^2 distributions for W electrons and testbeam electrons and pions.

These cuts were somewhat looser than those used in $W \rightarrow e\nu$ analyses [34].

In the gas calorimeters, our criteria for rejecting W electrons were:

- $E_t > 10$ GeV.
- For plug electrons, the cut on the shape of the EM shower was

$$\chi^2_{3\times3} < 20.$$

$\chi^2_{3\times3}$ is defined by

$$\chi^2_{3\times3} = \frac{1}{9}\sum_i \frac{[e_i - f_i]^2}{\sigma_i^2}$$

where the sum is over the 9 towers in a 3×3 section centered on the shower centroid and

e_i = Fraction of the EM energy in the 9 tower section measured in the ith tower.

f_i = Energy fraction in the ith tower observed for testbeam electrons.

σ_i = Estimated variance of f_i.

The $\chi^2_{3\times3}$ distributions for W candidate and testbeam electrons are shown in Figure 3.4. The data show that nearly all electrons from W decays have $\chi^2_{3\times3} < 20$.

For electron candidates in the forward calorimeter, the cut on the longitudinal shower shape was that at least 60% of the cluster energy be deposited in the first 15 sampling layers.

- At least half of the VTPC wire channels along a road between the event vertex and the calorimeter cluster had to record hits.
- The E_t deposited in a η-φ cone of radius 0.4 centered on the cluster minus the E_t of the cluster could not exceed 5 GeV. This required the lepton to be isolated.

The electron cuts eliminated 16 events.

3.6 The Undeposited p_t Cut

Since much of our background comes from events in which energetic charged particles deposit little or no energy in the calorimeters, it seems sensible to try to exploit the high efficiency and good momentum resolution of the CTC to identify

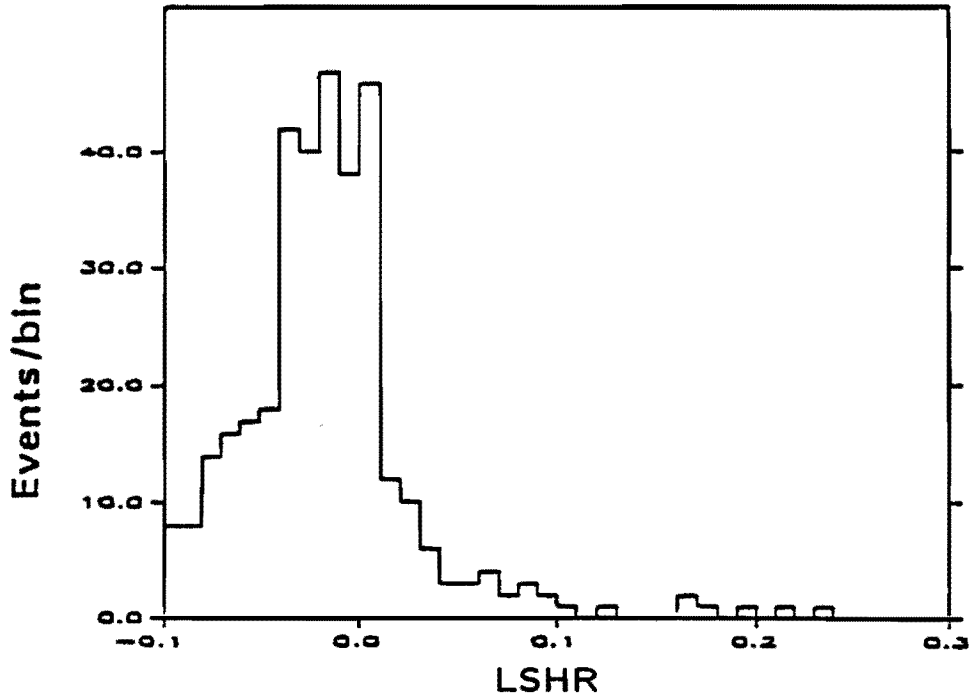

Figure 3.2: The LSHR distribution for a sample of W electrons.

these particles in the central region. Therefore, we looked in the CTC for tracks that had transverse momenta larger than their transverse energies measured by the calorimeters. We removed from our sample events in which the combined undeposited p_t of all such tracks, when subtracted from the $\not{E}_t$ measured by the calorimeters, was sufficient to reduce the transverse momentum imbalance below our threshold of 30 GeV. Specifically, we rejected events for which

$$|\vec{\not{E}}_t - \sum_{\text{CTC tracks}} (\vec{p}_t - \vec{E}_t)| < 30 \text{ GeV}$$

where $\vec{p}_t$ is the p_t of the particle measured by the CTC, and $\vec{E}_t$ is the E_t deposited in the calorimeters in an η-φ cone of radius 0.13 centered on the track. The sum is over CTC tracks with $p_t > 10$ GeV (CMIO's), and terms are included in the

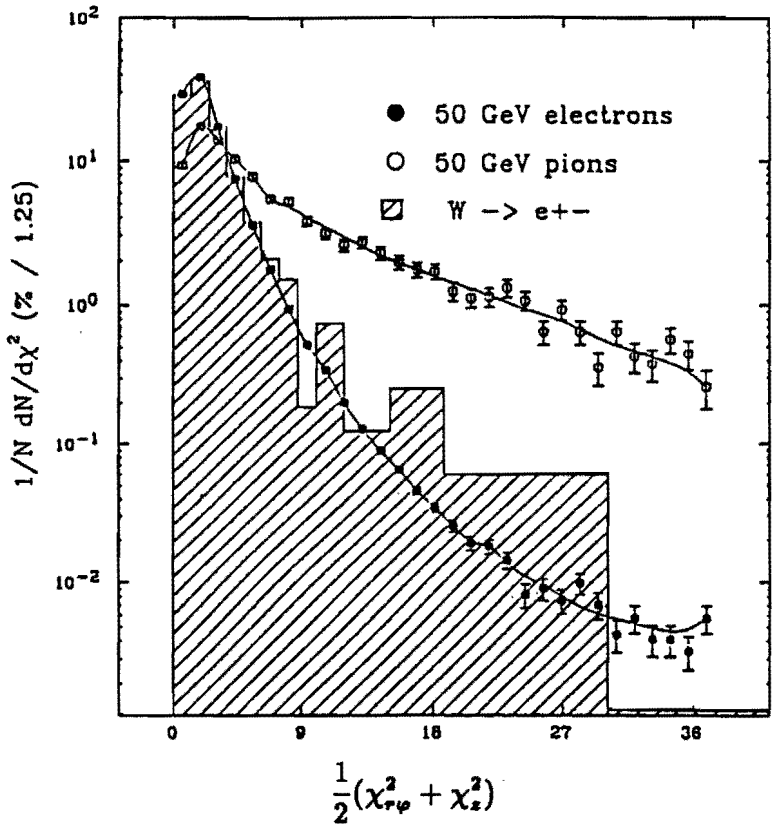

Figure 3.3: The CES χ^2 distributions for W electrons and testbeam electrons and pions.

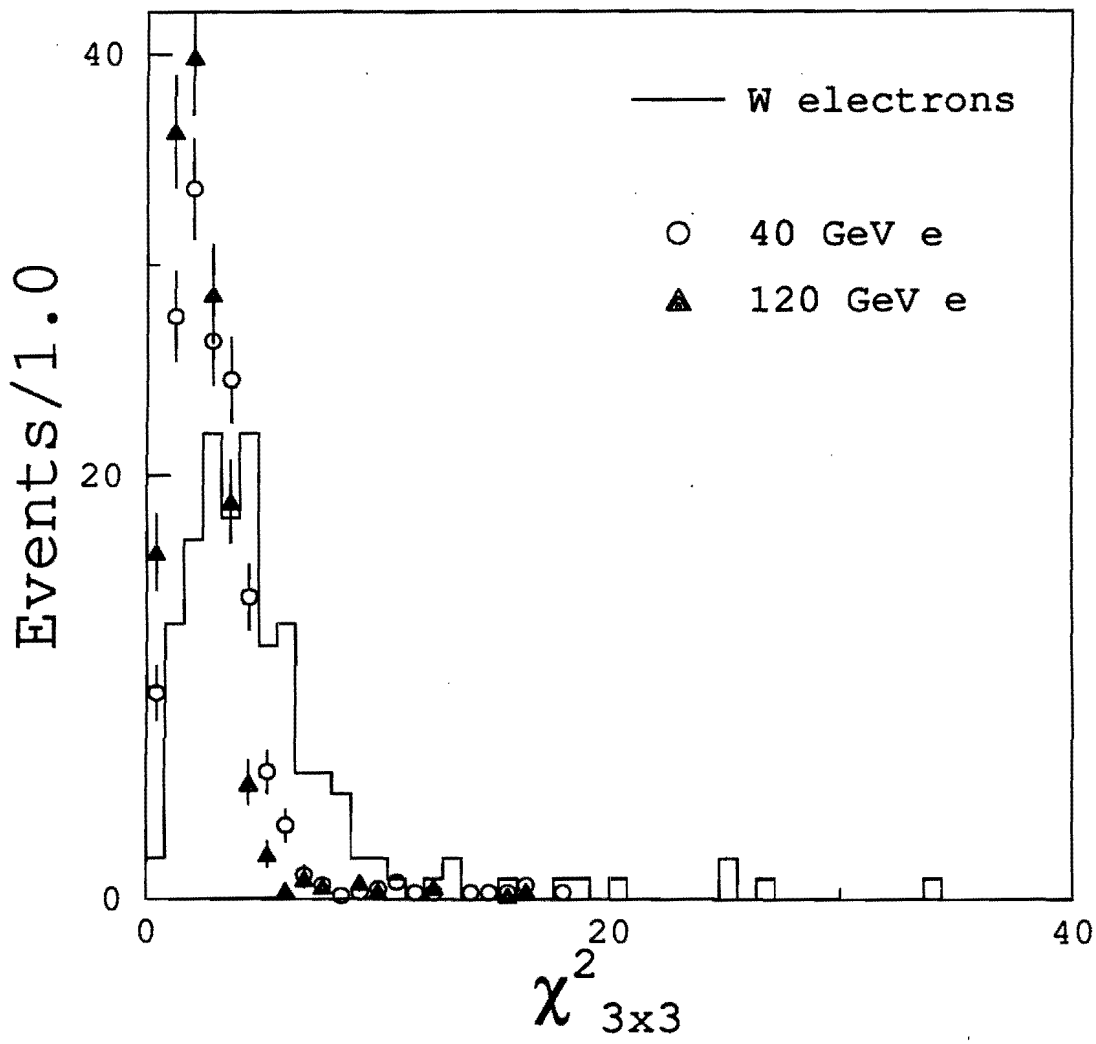

Figure 3.4: The PEM $\chi^2_{3\times3}$ distributions for testbeam electrons (data points) and W candidates (histogram).

sum only if $p_t > E_t$. Only two events were rejected by this cut. Upon inspection, one event is probably a $W \rightarrow \mu\nu$ decay in which the muon narrowly missed being recognized by the muon cuts and the other event appears to be a three jet QCD event in which a high-p_t particle escaped through a crack in the calorimetry.

In Figure 3.5 we show an r-φ view of the CTC for the QCD event that failed this cut. Around the circumference of the CTC is shown the r-φ projection of the energy deposition in the central calorimeters. In this event we find a track with $p_t = 21$ GeV associated with a cluster with an E_t of only 14 GeV. This event is an example of the QCD backgrounds that still remain in the data set.

3.7 The CTC Dijet Cuts

If a jet is lost in a crack and cannot be observed in the calorimeters, then perhaps it can still be seen by the tracking detectors. We have developed software which uses data from the CTC to identify lost jets in the region $|\eta| < 1.5$. Jets outside of this region can be seen with the VTPC, but dijet background cannot be reliably identified from the VTPC data. We defer a discussion of finding lost jets with the VTPC to Chapter 5.

The basic technique for identifying dijet events with tracking detectors is to look for a cluster of tracks back-to-back with the leading jet. We define a track cluster back-to-back to the leading cluster as a set of tracks in an η-φ cone of radius 0.7 with the cone axis opposite the leading cluster within $\pm 30°$. Clusters

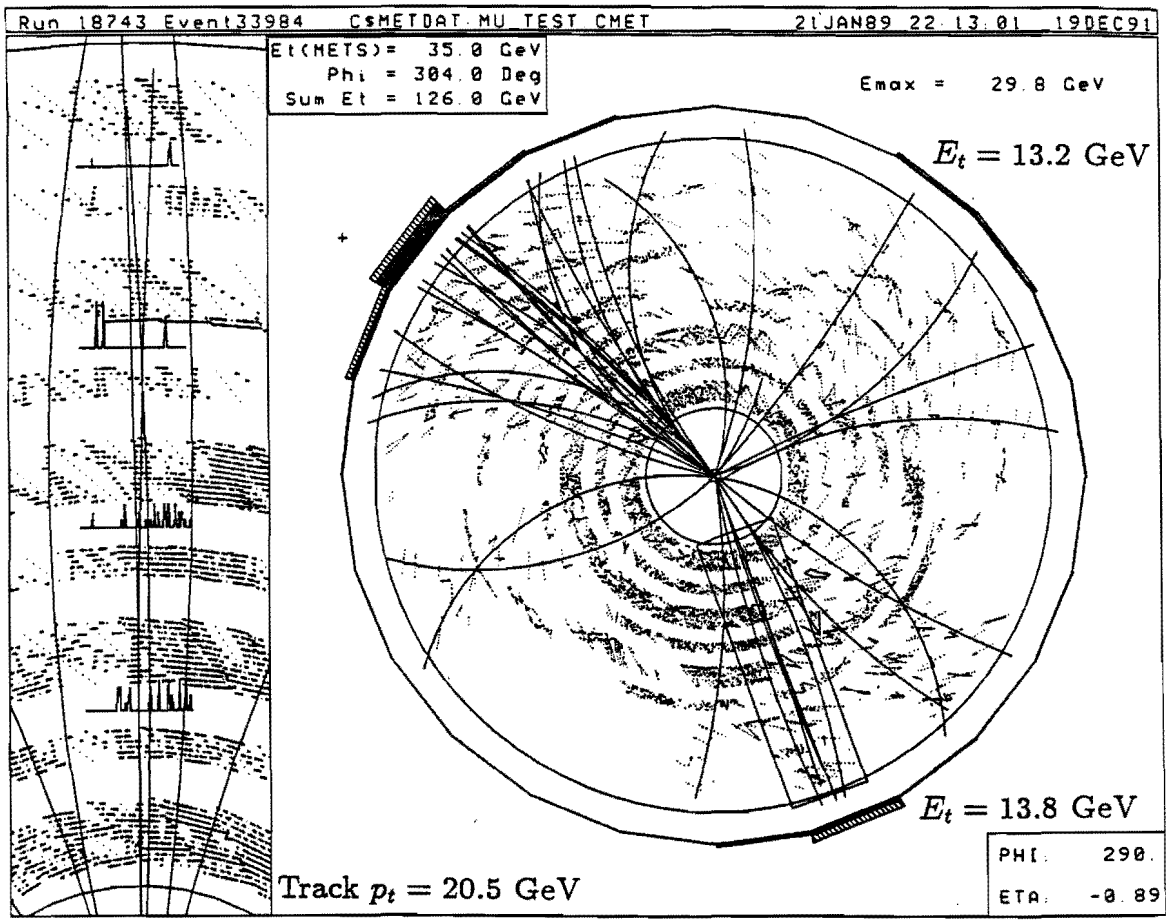

Figure 3.5: A QCD background event. The track in the center of the window has $p_t = 21$ GeV; its associated cluster has $E_t = 14$ GeV.

of CTC tracks are formed around "seed" tracks. Seed tracks are those tracks that are opposite to the leading cluster in φ within $\pm 30°$, and pass a set of quality cuts. For each seed track, the algorithm calculates the scalar sum of the transverse momenta, $\sum p_t$, of all the tracks within a cone of radius 0.7 in η-φ space centered on the seed track. The algorithm looks for the cone with the highest $\sum p_t$, and calculates its p_t centroid (the average of the η and φ coordinates of the tracks, weighted by their p_t). A new cluster is formed from the tracks that fall within a cone centered on the p_t centroid, and the centroid is recalculated. This process is repeated until it converges on a stable cluster.

The event is rejected as a dijet if the track cluster found in this manner satisfies the following criteria:

- The φ centroid is opposite to the leading cluster, within $\pm 30°$.
- The number of tracks in the cone is ≥ 2.
- $\sum p_t/(E_t$ of the leading cluster$) \geq 0.30$.

Three events from the data set were rejected by these cuts. We will show in Chapter 5 that these events are almost certainly dijet background. One of these events is shown in Figure 3.6. Three CTC tracks can be clearly seen back-to-back with the leading cluster. The energy from this jet was lost in a calorimeter crack at $\theta = 30°$ (cracks in the CDF calorimetry are discussed in Chapter 5.)

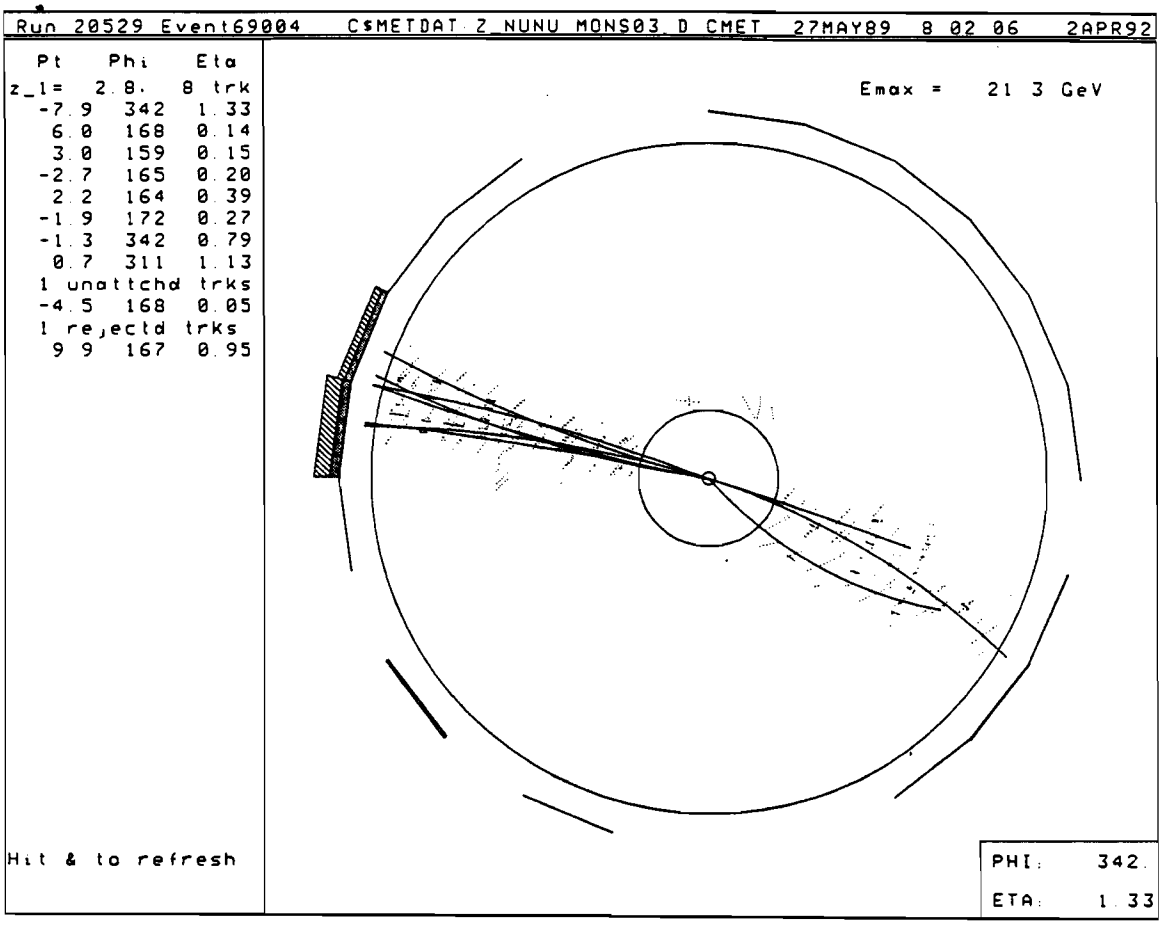

Figure 3.6: A dijet background event found by the CTC track clustering algorithm. The lost jet is at $\eta \simeq 1.3$.

3.8 Backgrounds from Cosmic Rays and Beam Gas

It is possible for the leading cluster in a monojet candidate event to be produced by energetic particles that do not come from the beam-beam interaction. These particles could come from cosmic rays or beam gas.

The initial cut on the central hadron timing information removed about 90% of the cosmic ray background. Approximately 5% of the cosmic rays were in time with the beam crossing, and another 5% deposited energy only in the EM calorimeters. The next cut used to reduce the cosmic ray/beam gas background was on the ratio $\sum p_t / E_t^{(1)}$, where $\sum p_t$ is the scalar sum of the transverse momenta of the CTC tracks associated with the leading cluster and $E_t^{(1)}$ is the transverse energy of the leading cluster. We refer to this quantity as the charged fraction, and we required that it be at least 0.1. Fake clusters caused by particles from outside the detector are unlikely to have a significant number of stiff CTC tracks pointing at them, and usually fail this cut. But how many cosmic ray and beam gas events remain in the sample?

To answer this question, we compared the leading clusters in the monojet candidate events to a sample of jets that are free of cosmic rays and beam gas. These jets were selected from QCD dijet events. The dijet events were required to have two jets back-to-back in φ within 30°, and the transverse energies of these jets had to be equal to within 20%. We also required the z coordinate of the vertex

to be no more than 60 cm from the center of the detector. The leading clusters had to pass the same cuts as the leading clusters in the monojet candidate events. To avoid including cosmic rays and beam gas in the dijet sample, the events were also required to have $\sigma_{\mathrm{MET}} < 2$ GeV$^{\frac{1}{2}}$. Our sample of dijet events that satisfy these criteria contains approximately 44000 events.

In Figure 3.7 we display a histogram of the charged fraction of the leading cluster for the 245 monojet candidates that survive the W and dijet cuts. Also shown in this plot is a distribution of the charged fraction of the leading cluster from the QCD dijet events, normalized to 245 events. Compared to the dijet events, the monojet candidates show an excess of events with low charged fraction. This indicates that a substantial amount of cosmic ray/beam gas background remains in the sample.

Figure 3.8 shows a scatter plot of charged fraction versus E_{OOT}, the amount of energy in the central hadron calorimeters that is outside of the beam crossing time window. Note that events with relatively large out of time energy also tend to have a low charged fraction. At least one these events definitely contains a cosmic ray. An r-φ view of this event is shown in Figure 3.9. This display shows the CTC and the central muon chambers. Hits in the CMU chambers are indicated by crosses. The CMU hits show where the particle entered and exited the detector. Along a line connecting these points, an ionization trail in the CTC is visible. This event has a charged fraction of 0.11 and 5.2 GeV of out of time energy. It appears to be a low-E_t dijet, but the extra energy from the cosmic ray

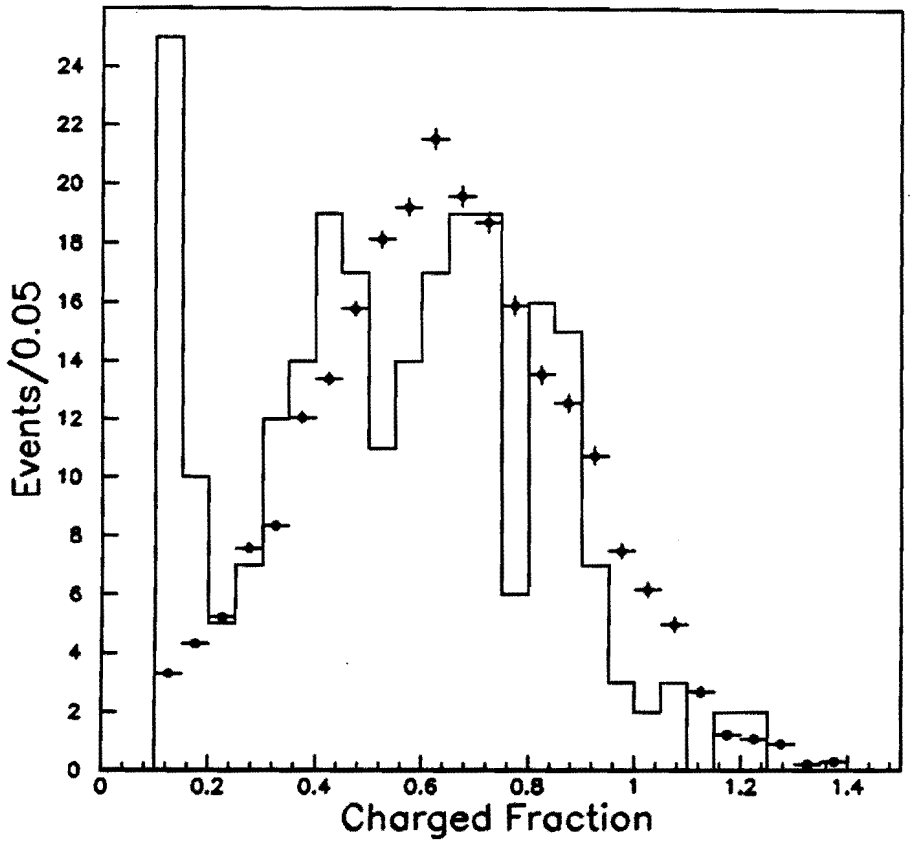

Figure 3.7: The charged fraction of the leading cluster in the monojet candidates (histogram) and the charged fraction of the leading cluster in dijet events (data points) normalized to the same sample size. Error bars indicate statistical uncertainties.

caused it to pass the monojet cuts.

We assume that all the events with charged fraction less than 0.2 and $E_{OOT} >$ 0.4 GeV are background, and we remove them from the sample. These cuts are shown graphically in Figure 3.8.

Besides the charged fraction and the out of time energy, there is one other measurement that is useful in discriminating between the monojet signal and cosmic ray/beam gas background. This quantity is the ratio of the EM energy of the leading cluster measured by the CES chambers to the energy measured by the CEM calorimeters. A histogram of the CES/CEM ratio for the monojet candidates is shown in Figure 3.10. For real jets this ratio is typically around unity, but for fake clusters it is often close to zero. Figure 3.10 shows a peak at small values of the CES/CEM ratio that can be attributed to cosmic ray and beam gas background. Figure 3.11 shows a scatter plot of charged fraction versus CES/CEM ratio for the leading clusters in the monojet candidates. Most of the events with low CES/CEM ratio also have a low charged fraction. We assume that all the events with CES/CEM ratio less than 0.2 and charged fraction less than 0.2 are background, and we remove them from the sample. These cuts are shown graphically in Figure 3.11.

A final test for beam gas background is to visually examine the VTPC data for evidence of tracks coming from a point outside of the detector. A scan of the entire 245 event monojet candidate sample revealed a single event that is definitely contaminated by beam gas particles. The VTPC data for this event

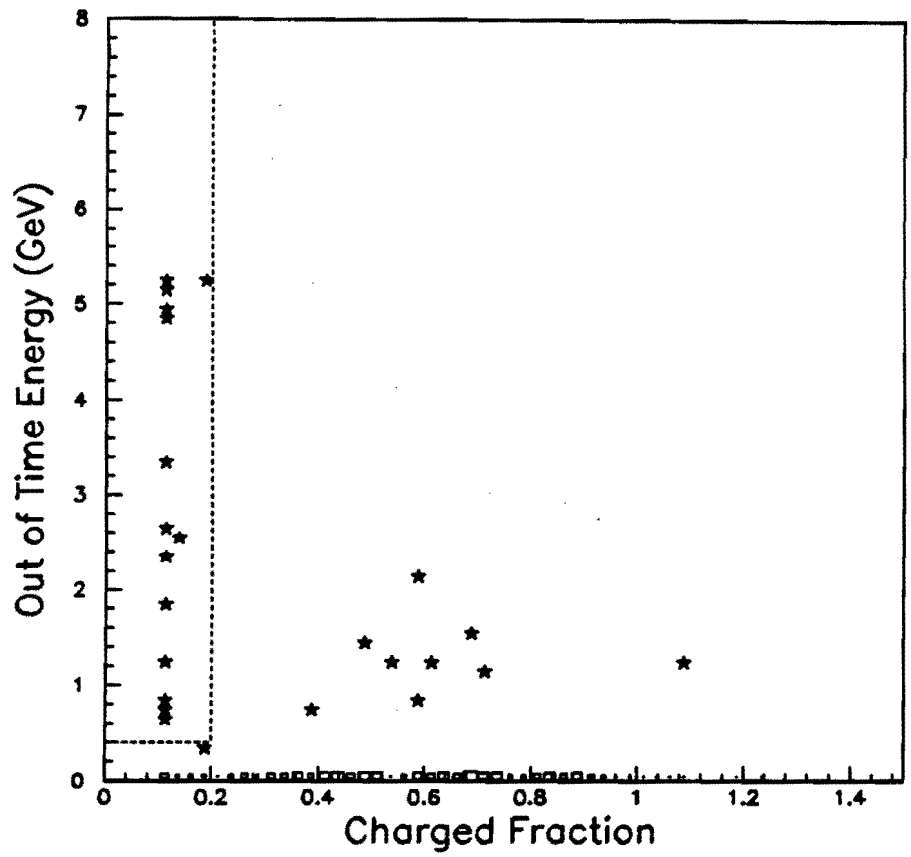

Figure 3.8: Scatter plot of the charged fraction of the leading cluster versus out of time energy in the CHA calorimeters for the monojet candidates. Stars indicate one or two events per bin. The events in the box were rejected as background.

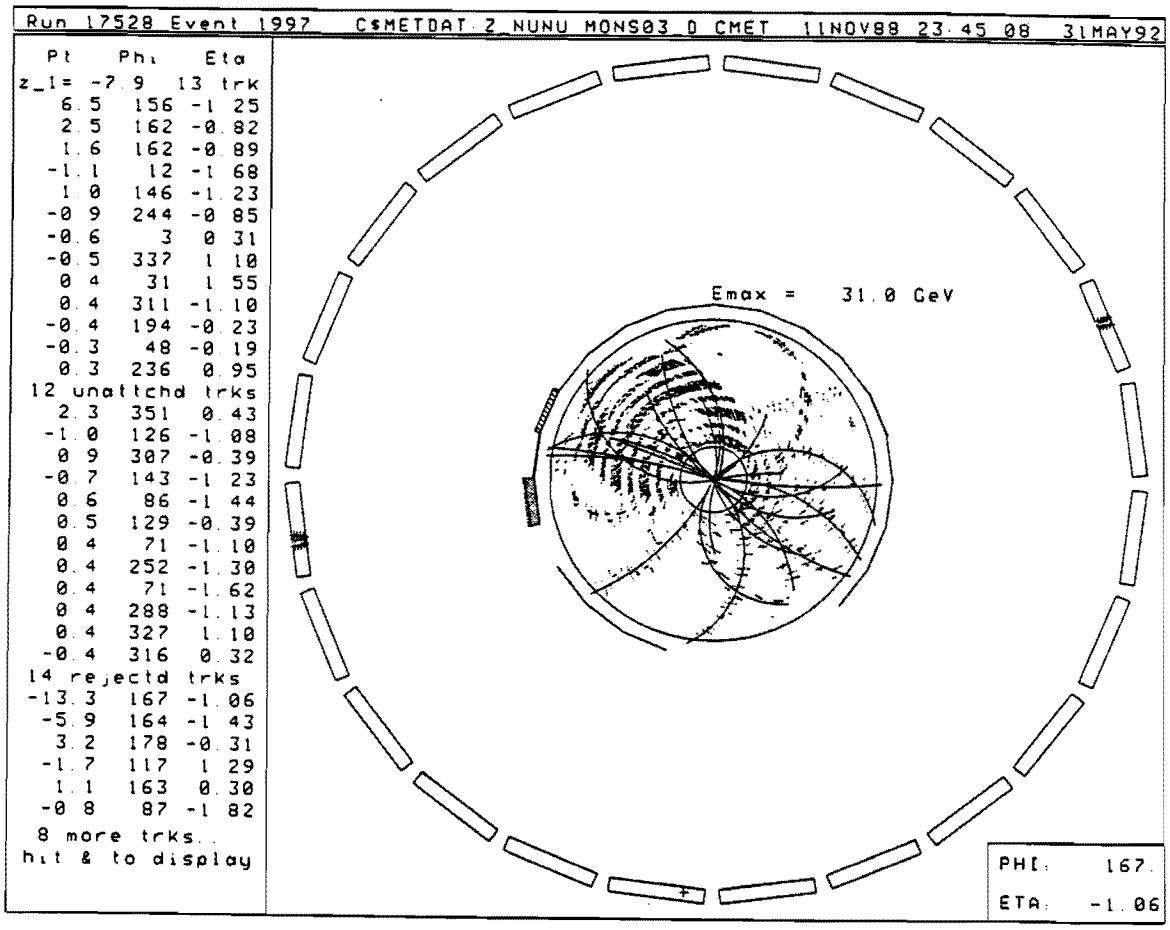

Figure 3.9: An r-φ view of the CTC and central muon chambers for a cosmic ray background event. The energy deposition in the central calorimeters is shown around the circumference of the CTC. Note that the cosmic ray passed through the tower with the most energy.

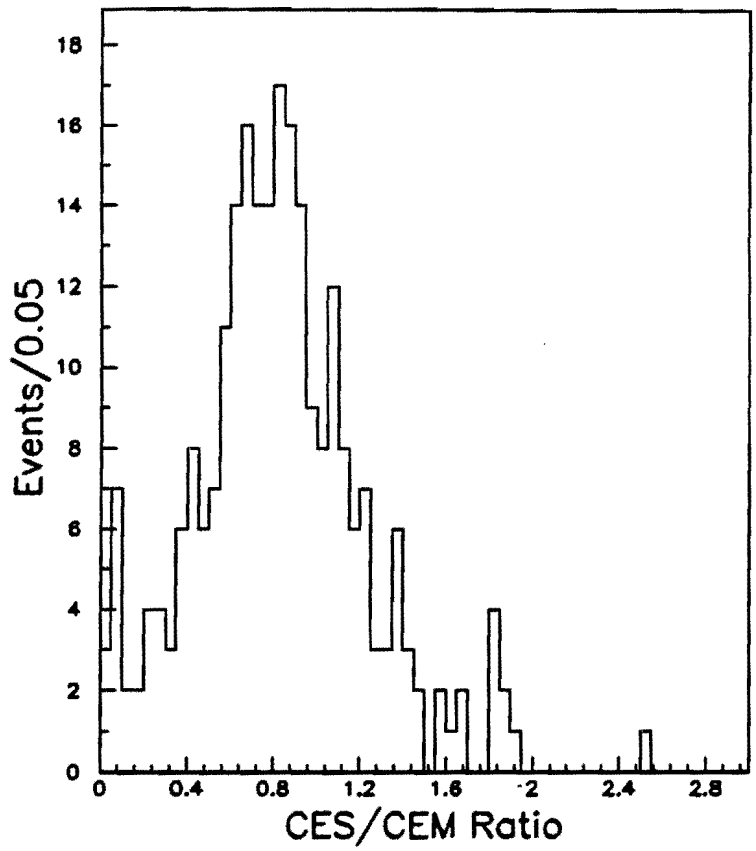

Figure 3.10: The CES/CEM energy ratio for the leading cluster in the monojet candidate events.

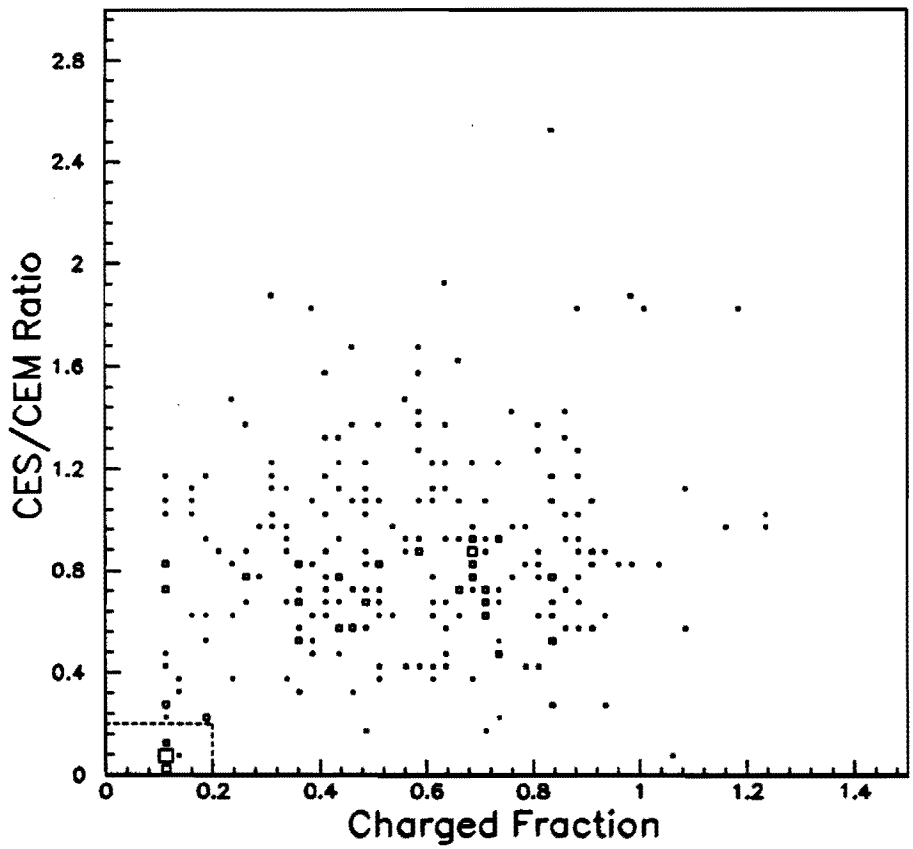

Figure 3.11: Scatter plot of the charged fraction of the leading cluster versus the CES/CEM energy ratio for the monojet candidates. The events in the box were rejected as background.

is shown in Figure 3.12. This display shows the wire hits in each of the eight VTPC octants, projected onto an r-z plane. Tracks can be clearly seen entering the VTPC from the viewer's left of the center of the detector. For comparison, Figure 3.13 shows the VTPC data for a typical beam-beam interaction from the monojet sample. The beam gas event also has a low charged fraction (0.19). We removed it from the sample.

Our cuts have removed 19 cosmic ray and beam gas events from the sample. The charged fraction distribution for the 226 remaining events is shown in Figure 3.14. The sample now contains 16 events with charged fraction less than 0.2. To determine how many of these events are residual background, we assume a background of N_{back} events and normalize the charged fraction distribution from the dijet sample to $226 - N_{back}$ events. We look for the value of N_{back} that gives the predicted number of jets with charged fraction less than 0.2 closest to $16 - N_{back}$. We find the best estimate for the residual background is $N_{back} = 9$. For this value of N_{back}, the dijet data predict 6.7 events with charged fraction less than 0.2. The uncertainty on this estimate is dominated by the statistical uncertainty in the number of monojet candidates with charged fraction less than 0.2. The error on our background estimate is therefore $\sqrt{16} = 4$ events.

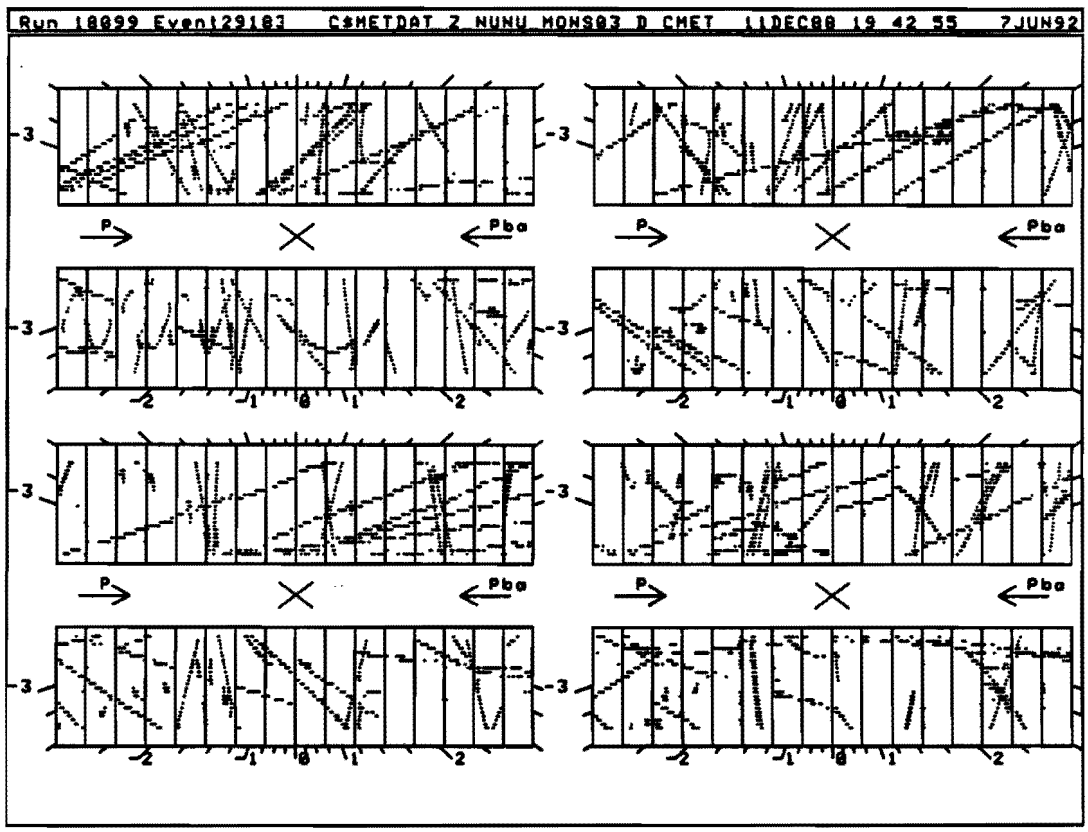

Figure 3.12: An r-z view of the wire hits in each of the eight VTPC octants for a beam gas event.

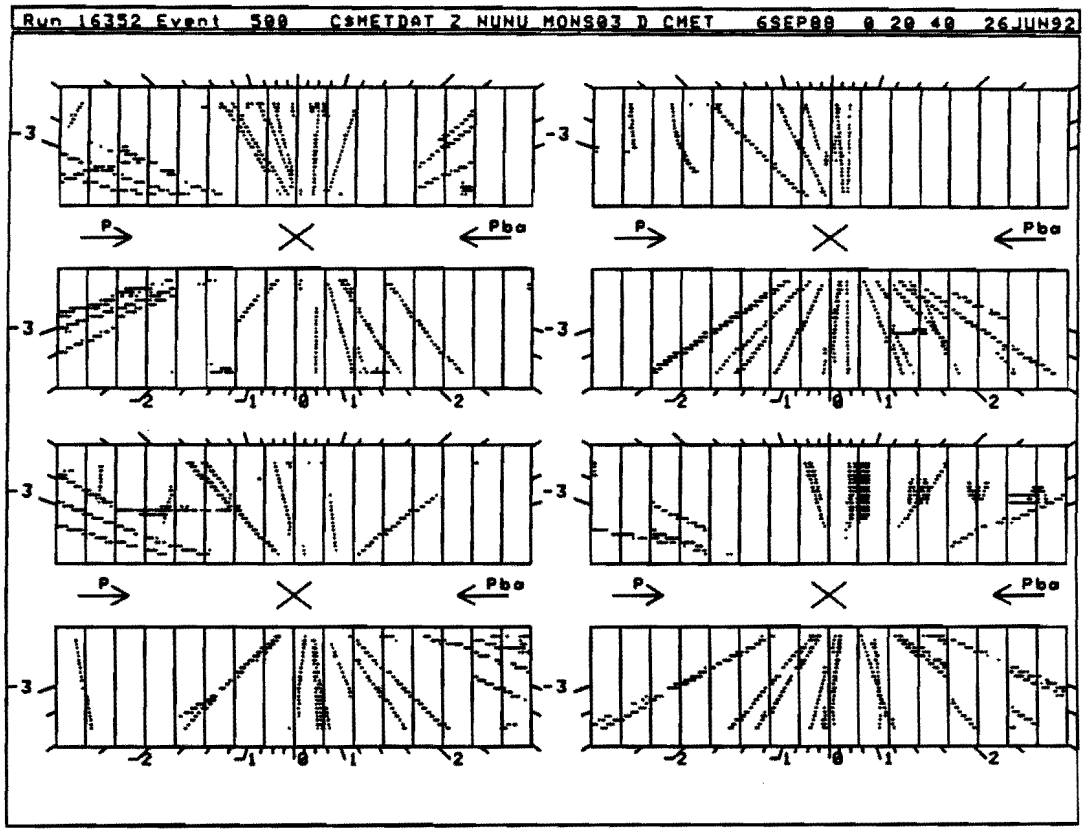

Figure 3.13: The VTPC display for a beam-beam interaction from the monojet sample.

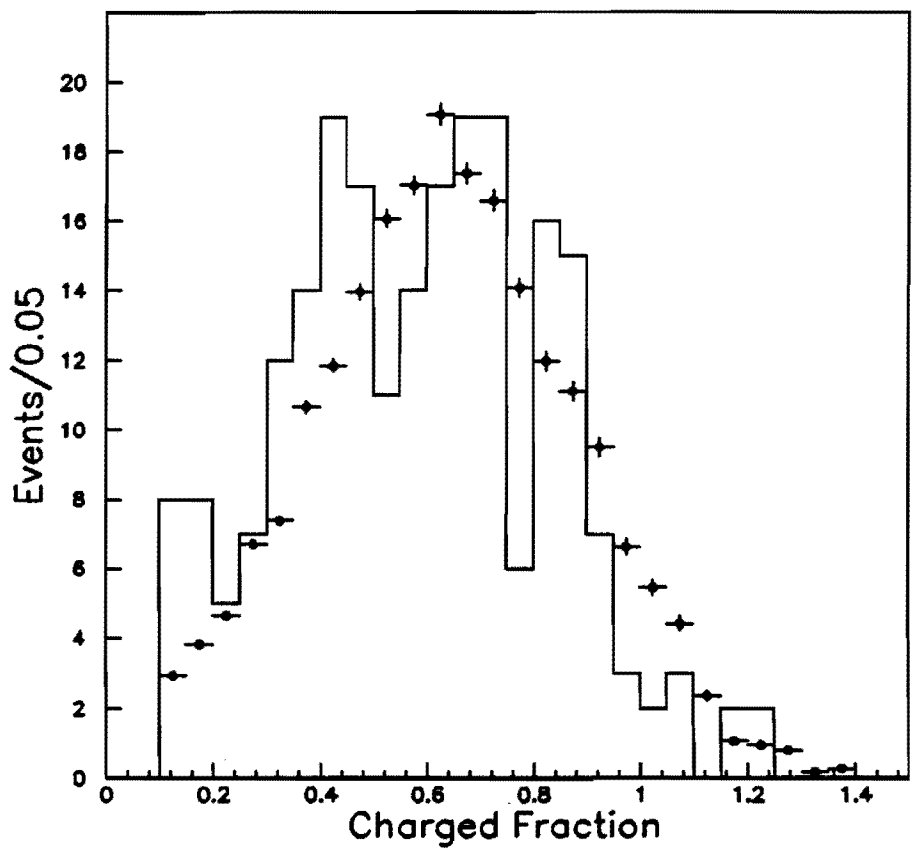

Figure 3.14: The charged fraction of the leading cluster in the monojet candidates (histogram) after removal of cosmic ray and beam gas background, and the charged fraction of the leading cluster in dijet events (data points) normalized to 217 events.

	Number of Events
Monojet Candidates	510
Rejected by τ cuts	135
Rejected by CMU muon cuts	39
Rejected by CMIO muon cuts	70
Rejected by electron cuts	16
Rejected by undeposited p_t cut	2
Rejected by CTC dijet cuts	3
Rejected by cosmic ray/beam gas cuts	19
Events surviving cuts	226

Table 3.1: Number of events rejected by the cuts described in this chapter. The cuts were made in the order shown.

3.9 The Monojet Sample

The $\not{E}_t$ distribution for the 226 events in the final monojet sample are shown in Figure 3.15. Also shown is a Monte Carlo estimate of the $\not{E}_t$ spectrum of the expected $Z^0 \rightarrow \nu\bar{\nu}$ signal. We describe our Monte Carlo techniques in Chapter 4.

Figure 3.15 shows that a substantial amount of background remains in the monojet sample, and that background events tend to have relatively low $\not{E}_t$.

We remind the reader that the distribution shown in Figure 3.15 is of the raw missing E_t, and that this quantity is only a rough measure of the true transverse momentum imbalance. The technique for correcting the measured missing E_t is discussed in Appendix A. Figure A.1 shows a distribution of the corrected $\not{E}_t$ for the monojet sample and the Z^0 p_t distribution corresponding to the Monte Carlo result displayed in Figure 3.15.

In Figure 3.16 we display a lego plot of the calorimetry information for a typical monojet from the final event sample. In Figure 3.17 we show an r-φ view of the CTC for the same event.

In the following chapter we present Monte Carlo estimates of the residual $W^{\pm}$ and $Z^0 \rightarrow \ell^+\ell^-$ backgrounds remaining in the monojet sample.

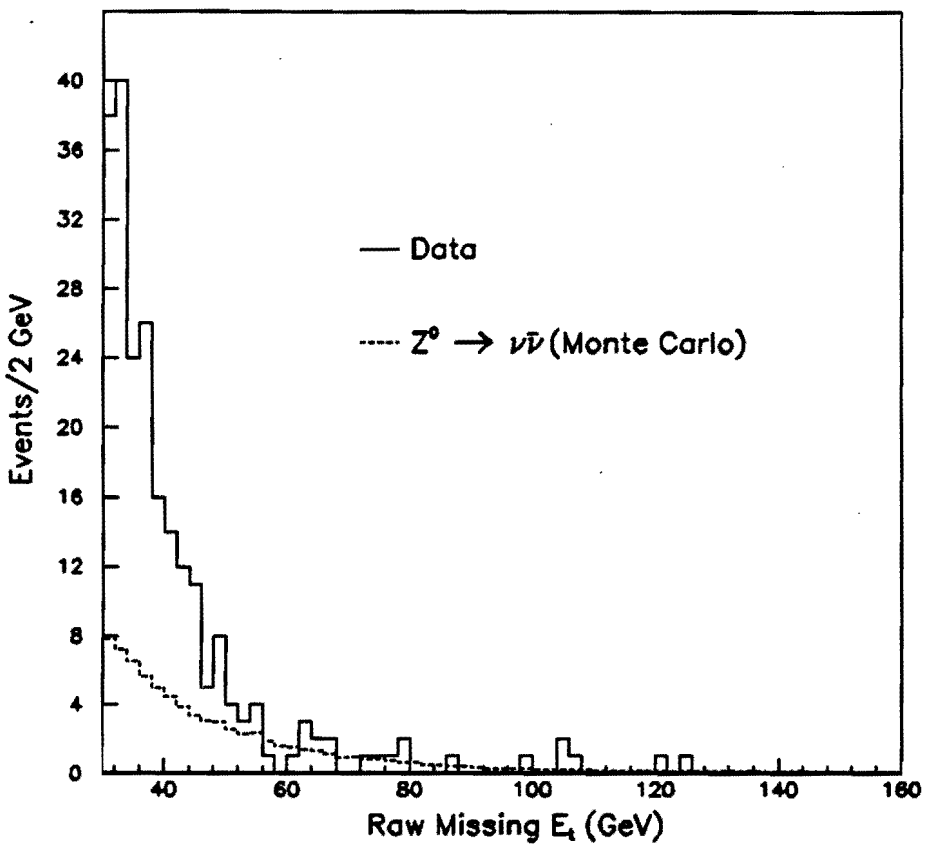

Figure 3.15: Raw $\not{E}_t$ distribution for the 226 events that pass the monojet cuts. Also shown is the estimated $\not{E}_t$ distribution for the expected monojet signal.

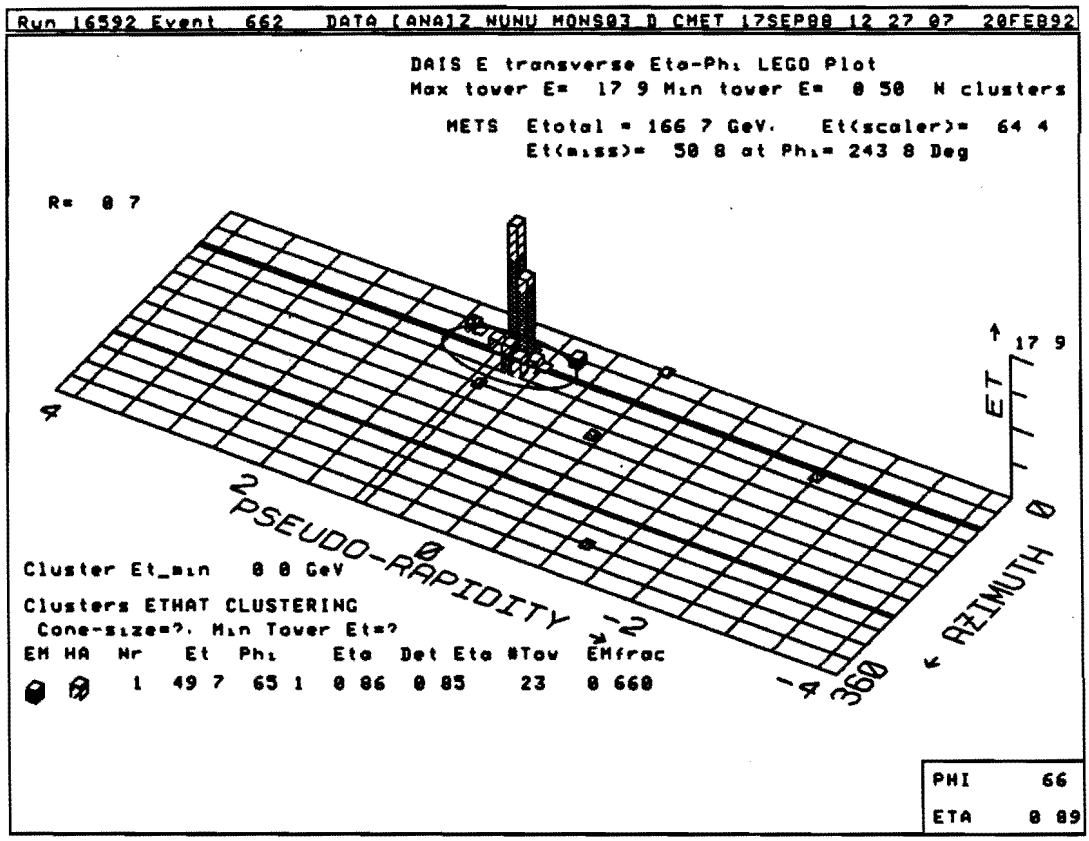

Figure 3.16: Calorimetry lego display for a typical monojet event. The leading cluster has $E_t = 50$ GeV; the missing E_t is 51 Gev.

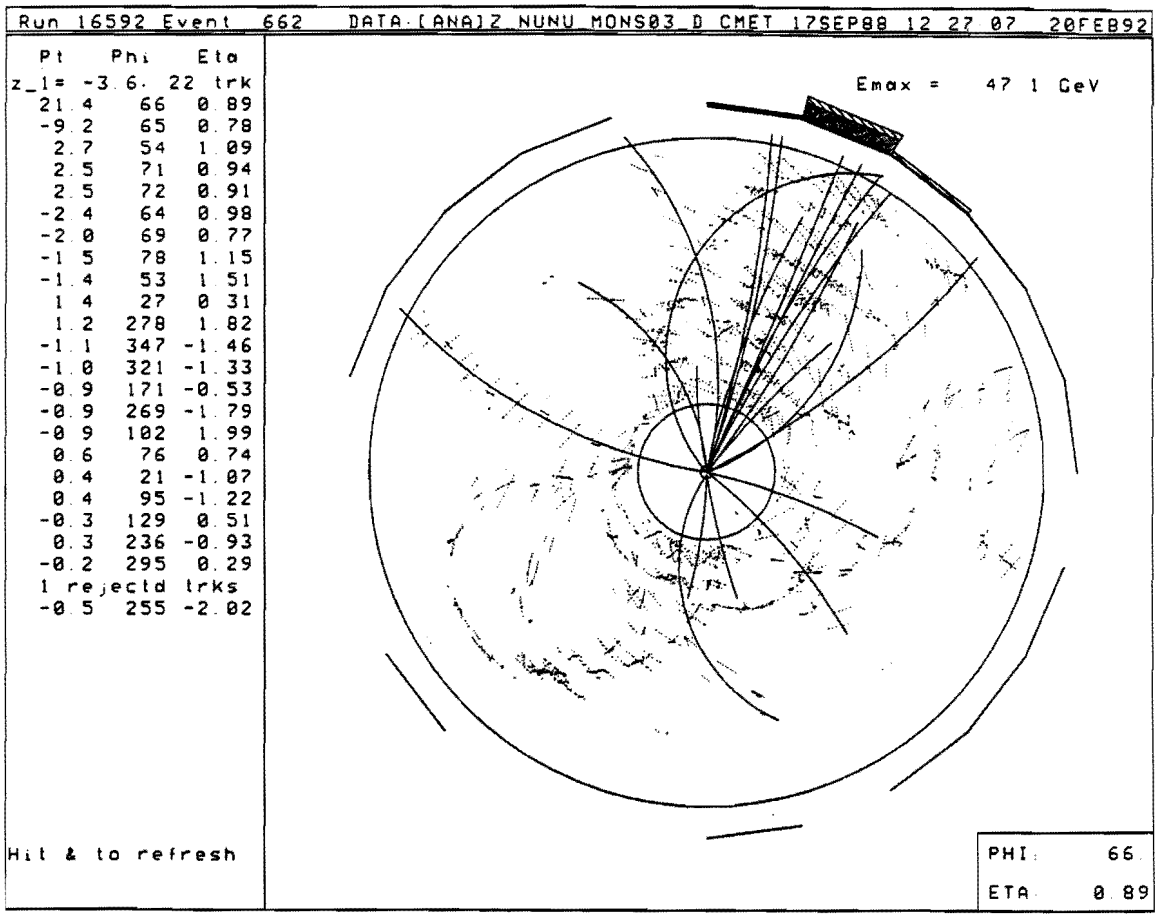

Figure 3.17: CTC r-φ display for a typical monojet event.

Chapter 4

Monte Carlo Simulations of W and Z Decays

In this chapter we describe the Monte Carlo techniques that were used to estimate the $Z^0 \rightarrow \nu\bar{\nu}$ signal in the monojet sample and the residual backgrounds from W and $Z^0 \rightarrow \ell^+\ell^-$ decays. With the exception of the process $W \rightarrow \tau\nu$; $\tau \rightarrow$ hadrons (described below), we simulated all processes involving intermediate vector bosons using the PAPAGENO Monte Carlo event generator [35] to calculate the cross sections, a Feynman-Field fragmentation model [36] to fragment the final state partons, and the CDF software package QFL [50],[51] to simulate detector response. Each step in the simulation has potential sources of systematic error. In the sections below, we identify the sources and attempt to estimate the magnitudes of the errors in our Monte Carlo calculations.

4.1 The Event Generator

Consider a generic hadron-hadron interaction:

$$A + B \rightarrow c + d.$$

A and B represent the incoming hadrons; c and d are the final state partons (quarks, gluons, or gauge bosons). This process is shown symbolically in Figure 4.1. According to the parton model, the cross section for this process is given by

$$\sigma_{AB\rightarrow c}(p_A, p_B, p_c) = \sum_{a,b} \int_{\xi_a}^{1} dx_a \int_{\xi_b}^{1} dx_b f_A^{(a)}(x_a) \hat{\sigma}_{ab\rightarrow cd}(x_a p_A, x_b p_B) f_B^{(b)}(x_b)$$

where the sum is over the partons in the incoming hadrons and

- p_A, p_B, and p_c are the four-momenta of particles A, B and c respectively.
- x_a and x_b represent the fraction of the momenta of hadrons A and B carried by partons a and b.
- $f_A^{(a)}$ and $f_B^{(b)}$ are the parton distribution or structure functions. These give the probability of finding a parton of type a (b) inside hadron A (B).
- $\hat{\sigma}_{ab\rightarrow cd}$ is the cross section of the fundamental parton process $a + b \rightarrow c + d$.
- ξ_a and ξ_b represent limits of integration determined by the kinematics of the process.

We assume that we are observing the interaction in the center of mass frame where the total momentum is zero. In this frame, the initial state partons carry

no transverse momentum. The observed transverse momenta of the final state partons comes from the subprocess $a + b \rightarrow c + d$, and hence must balance:

$$\vec{p}_{t_c} = -\vec{p}_{t_d}.$$

In terms of the scaling variables, the longitudinal momentum balance is:

$$x_a + x_b = x_c + x_d.$$

At high energies, where the particle masses can be neglected, the pseudorapidity of a final state parton is given by

$$\eta = \sinh^{-1} \frac{x\sqrt{s}}{2p_t}$$

where $\sqrt{s}$ is the total energy in the center of mass.

In a Monte Carlo program that simulates the process $A + B \rightarrow c + d$, the event generator plays the following role. Given the four momenta of the incoming hadrons, it produces possible four momenta of the outgoing particles. For each choice of final state four momenta, it calculates the cross section $\sigma_{AB\rightarrow cd}$. The parton level cross sections $\hat{\sigma}_{ab\rightarrow cd}$ are calculated using perturbative QCD expansions. The sources of error in this procedure are the statistical error resulting from the finite number of events generated, and the uncertainties in the structure functions and perturbative QCD calculations. The statistical error can be made very small by simply generating a large number of events.

The structure functions we used were determined from deep inelastic lepton-hadron scattering data. However, there are many possible structure functions

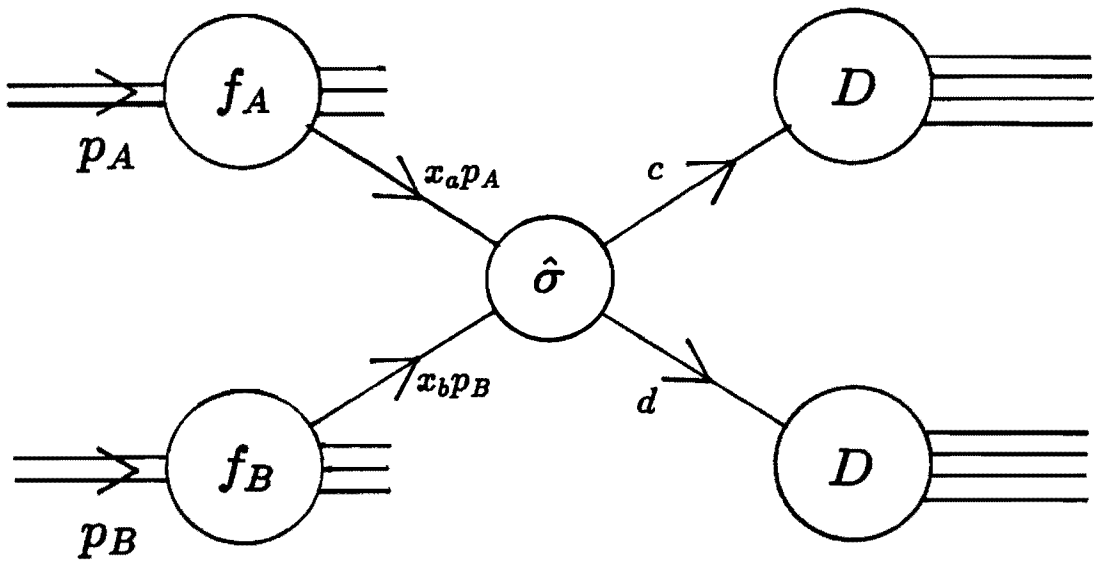

Figure 4.1: The parton model picture of a hadron-hadron interaction. D represents the fragmentation functions. The QCD subprocess denoted by $\hat{\sigma}$ is the 2 to 2 reaction $a + b \to c + d$.

consistent with the data. To estimate the systematic error in a Monte Carlo calculation caused by the structure function uncertainty, we compared results from several different choices of structure functions. The sets of functions we used were MRSB [37, 38], EHLQ1, EHLQ2 [39, 40], and Martinelli *et. al.* [41]. The structure functions were derived from neutrino-nucleon scattering data from several experiments, and the MRSB functions are also based on muon-nucleon scattering data from the Bologna-CERN-Dubna-Munich-Saclay Collaboration (BCDMS).

The structure functions and parton level cross sections depend logarithmically on the choice of the QCD mass scale Q^2. Q^2 is used in calculating the strong coupling constant α_s. The formula for $\alpha_s(Q^2)$ is

$$\alpha_s(Q^2) = \frac{12\pi}{(33 - 2n_f)\ln(Q^2/\Lambda^2)}$$

where n_f is the number of quark flavors, and Λ is the cut off value of Q^2, i.e. $\alpha_s(\Lambda^2) = \infty$. It is appropriate to choose the mass scale to be on the order of the square of some large momentum transfer in the particular process under consideration, but there is not a unique "correct" value for Q^2. We estimated the uncertainty caused by this ambiguity by using two different values for Q^2 and comparing the results. The two values for Q^2 were $\langle p_t \rangle^2$ and $\langle p_t \rangle^2/4$, where $\langle p_t \rangle$ is the average transverse momentum of the final state primary particles. Final state primary particles include quarks, gluons, and gauge bosons, but not their decay products. For the case of an event containing a W or Z with $p_t = 0$, these definitions of Q^2 are incorrect. However, in our simulations we always generated

vector bosons with finite transverse momentum.

4.2 Parton Fragmentation

The quarks and gluons produced in the fundamental scattering process $A + B \rightarrow c + d$ will form hadronic jets through a process known as fragmentation. The FORTRAN routines that were used to fragment the partons are modified versions of the routines used in the ISAJET Monte Carlo [42]. The routines that produced the underlying event were also borrowed from ISAJET. The parameters in the routines that model the fragmentation were adjusted to reproduce the jet characteristics observed in a high statistics sample of CDF two jet events [43]. The underlying event routines were fine tuned to model as accurately as possible the events in the CDF $W \rightarrow e\nu$ sample [34].

Figures 4.2 and 4.3 compare the jet fragmentation and underlying events in real $W \rightarrow e\nu$ events to Monte Carlo output. The real data are shown as data points with statistical error bars, and the simulated data are shown as histograms. The W events were required to have one and only one jet with $E_t > 10$ GeV. This jet had to also be in the central region. 138 events from the $W \rightarrow e\nu$ sample satisfied these requirements.

Figure 4.2 shows normalized distributions of the properties of the CTC tracks associated with the leading jets. The quantities displayed are:

- Transverse momenta of the CTC tracks ("Track p_t")

- Number of CTC tracks ("Track Multiplicity")
- $|\varphi_{jet} - \varphi_{track}|$ ("Track $\Delta\varphi$") where φ_{jet} is the azimuthal angle of the jet axis and φ_{track} is the φ of each track.
- $Z_t = p_{||}^{(track)}/p_t^{(jet)}$ ("Track Z_t") where $p_{||}^{(track)}$ is the momentum of each track parallel to the jet axis and $p_t^{(jet)}$ is the transverse momentum of the jet.

The plots in Figure 4.3 show the distributions of the transverse momentum, multiplicity, and scalar sum of the transverse momenta ($\sum p_t$) for CTC tracks in the underlying event.

These distributions show good agreement between data and Monte Carlo. We therefore assume that the systematic errors in the simulation of jet fragmentation and the underlying event are small enough to be neglected.

4.3 Detector Simulation

The CDF detector simulation code is described in detail in Appendix B. There are uncertainties inherent in the modeling of each component of the detector, but the systematic error is dominated by the uncertainty in the energy scale of the calorimeters. The energy scale affects the number of events that pass the $\not{E}_t$ cut and the other energy thresholds in the analysis. As described in Appendix B, a conservative estimate of the uncertainty in the simulated energy scale is 5%. We

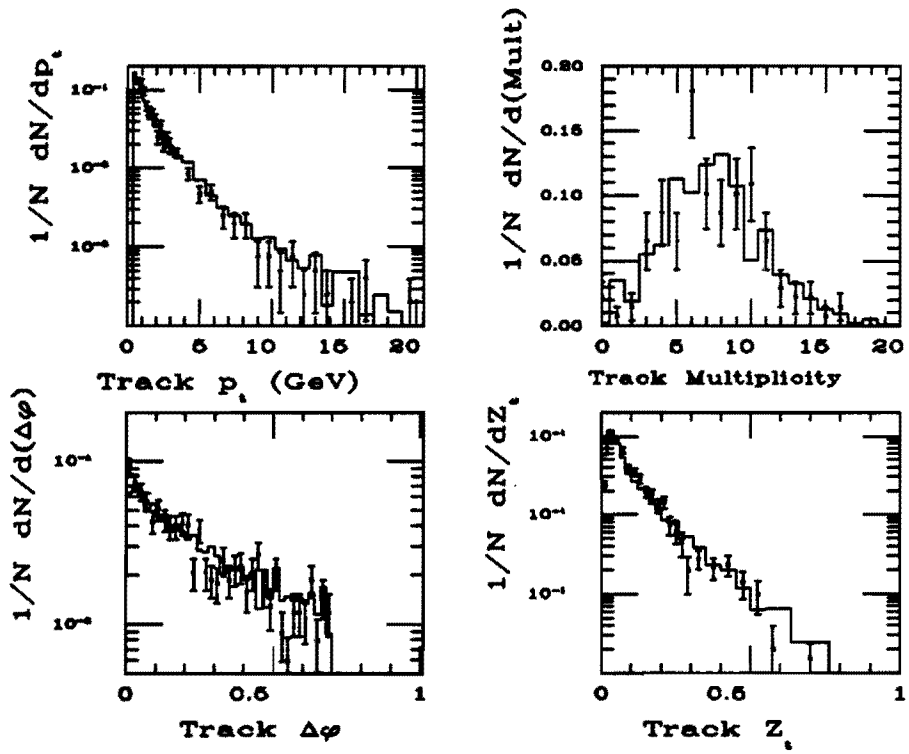

Figure 4.2: Comparison between jet fragmentation in W events (data points) and Monte Carlo (histograms). The variables displayed are defined in the text.

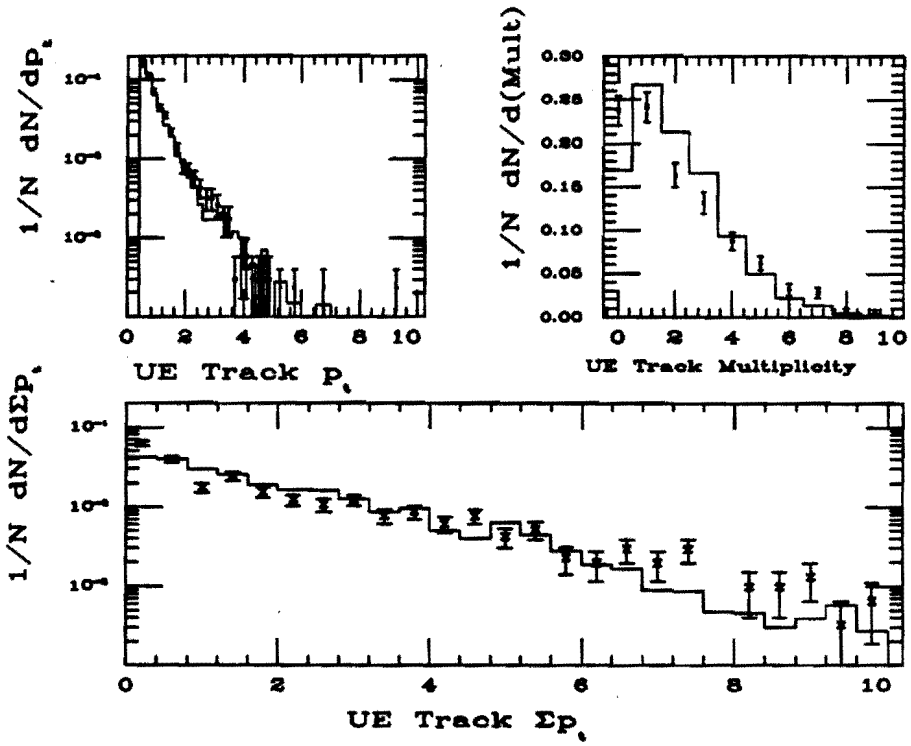

Figure 4.3: Comparison between the underlying events in W events and Monte Carlo. The variables displayed are defined in the text.

estimated the errors this uncertainty produced in the simulations by varying the energy scale ±5% and recalculating the results.

4.4 $Z^0 \rightarrow \nu\bar{\nu}$ Signal

Monte Carlo predictions for the $Z^0 \rightarrow \nu\bar{\nu}$ signal in the final data sample are summarized in Table 4.1. Also listed in Table 4.1 are the values of Λ (defined by the $\alpha_s(Q^2)$ equation in Section 4.1) assumed in evaluating the structure functions. The systematic errors quoted include the uncertainties in the trigger efficiency and luminosity. Of the eight possible combinations of structure functions and Q^2, the strongest signals are predicted by the EHLQ2 and MRSB structure functions with $Q^2 = \langle p_t \rangle^2/4$. However, the EHLQ2 structure functions give a slightly higher average $\not{E}_t$. The Martinelli *et. al.* and EHLQ1 structure functions with $Q^2 = \langle p_t \rangle^2$ predict the fewest events, and the Martinelli *et. al.* functions give the softest $\not{E}_t$ spectrum. We choose to quote as our nominal value for the estimated number of monojet events in the final data set the results obtained from the MRSB structure functions with $Q^2 = \langle p_t \rangle^2/4$:

$$77.8 \pm 5.4 \text{ (sys.)} \pm 0.5 \text{ (stat.)} \text{ events.}$$

The effect of increasing the calorimeter energy scale in the simulation is to increase the observed $Z^0 \rightarrow \nu\bar{\nu}$ signal. This is because more events will pass the $\not{E}_t$ cut. Likewise, decreasing the energy scale leads to a smaller observed signal. To estimate the lower bound on the number of $Z^0 \rightarrow \nu\bar{\nu}$ events predicted

Structure Function	Λ (MeV)	Q^2	Number of Events $\pm$ (sys.) $\pm$ (stat.)
MRSB	200	$\langle p_t \rangle^2/4$	$78 \pm 5.4 \pm 0.5$
Martinelli *et. al.*	160	$\langle p_t \rangle^2$	$61 \pm 4.3 \pm 0.4$
EHLQ1	200	$\langle p_t \rangle^2$	$62 \pm 4.3 \pm 0.4$
EHLQ2	290	$\langle p_t \rangle^2/4$	$78 \pm 5.5 \pm 0.5$

Table 4.1: Results of Monte Carlo simulations of $Z^0 \rightarrow \nu\bar{\nu}$.

by Monte Carlo, we ran the simulation using the combination Martinelli *et. al.* structure functions and $Q^2 = \langle p_t \rangle^2$ with a simulated energy scale 95% of its nominal value. This choice of structure functions and Q^2 gives the softest $\not{E}_t$ spectrum and will therefore yield the most conservative estimate of the lower bound. This simulation predicts the monojet signal to be:

$$55.7 \pm 3.9 \text{ (sys.)} \pm 0.4 \text{ (stat.) events.}$$

Similarly, to estimate the upper bound we used the EHLQ2 structure functions and $Q^2 = \langle p_t \rangle^2/4$ with the energy scale 105% of its nominal value. The upper bound on our monojet signal obtained in this manner is:

$$83.8 \pm 5.9 \text{ (sys.)} \pm 0.5 \text{ (stat.) events.}$$

We use these bounds as estimates of the systematic errors on the results of our Monte Carlo simulations. Figure 4.4 shows the $\not{E}_t$ spectrum of the simulated monojet signal and the limits of the systematic uncertainty. The histogram dis-

played in Figure 4.4 is the same as the estimated $Z^0 \rightarrow \nu\bar{\nu}$ signal shown in Figure 3.15.

4.5 W and Z Backgrounds

The same procedure that we used for estimating the monojet signal was used to estimate the background from each $W^{\pm}$ and Z^0 decay mode. The nominal Monte Carlo results were obtained using the MRSB structure functions and $Q^2 = \langle p_t \rangle^2/4$. The EHLQ2 structure functions and $Q^2 = \langle p_t \rangle^2/4$, with the energy scale 5% greater than the nominal value, were used in calculating the upper systematic bounds. The lower bounds are given by the Martinelli *et. al.* structure functions with $Q^2 = \langle p_t \rangle^2$ and the energy scale reduced by 5%. These results are summarized in Table 4.2. Figure 4.5 shows the PAPAGENO Monte Carlo predictions for the contributions to $\not{E}_t$ spectrum of the total W and Z background from each W decay mode. However, in determining the final results of this study, we do not use the PAPAGENO results for the background from $W \rightarrow \tau\nu$; $\tau \rightarrow$ hadrons. We use a different technique, described in the following section, to estimate the background from this source. Figure 4.6 shows the estimated $\not{E}_t$ distribution for the W and Z background that we use in our final calculations.

Figures 4.5 and 4.6 show that most of the background events from IVB decays have low missing E_t. The Monte Carlo results predict that about 90% of the background events will have $\not{E}_t < 60$ GeV. This is consistent with the data of

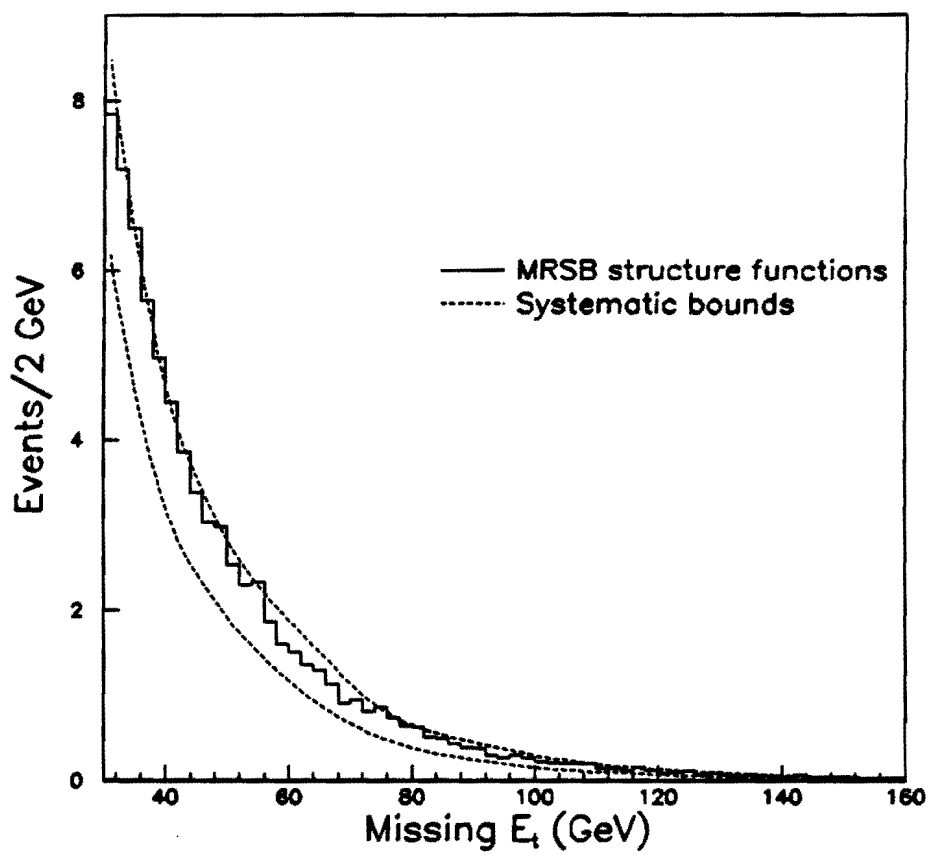

Figure 4.4: The $\not{E}_t$ spectrum of the $Z^0 \rightarrow \nu\bar{\nu}$ signal from Monte Carlo (using the MRSB structure functions) and the upper and lower systematic bounds. The histogram shown above is the same as the estimated $Z^0 \rightarrow \nu\bar{\nu}$ signal shown in Figure 3.15.

Figure 3.15, which show that most of the background occurs at low missing E_t.

When we summed the results of the background simulations, the systematic errors were handled in the following manner. We took one half of the difference between the upper and lower bounds on the total background to be a reasonable estimate of the error resulting from the uncertainties in structure functions, Q^2, and simulated energy scale. This number was added in quadrature to the systematic error from the trigger efficiency and luminosity uncertainties to obtain an estimate of the total systematic error. The estimate of the total W background quoted in Table 4.2 includes the estimate for the $\tau \rightarrow$ hadrons background from the Monte Carlo described in Section 4.5.1.

4.5.1 $W \rightarrow \tau\nu$ Background

For the case of hadronic decays of W taus, the sources of errors inherent in Monte Carlo calculations can be minimized by using a $W \rightarrow \tau\nu$ simulation based on real $W \rightarrow e\nu$ events. We have a sample of 2664 nearly background-free $W \rightarrow e\nu$ events recorded by CDF during the 1988-89 run. We used these data to estimate the amount of τ background remaining in our data set.

For each $W \rightarrow e\nu$ event in the real data set, we generated a simulated τ lepton with the same momentum as the electron. The τ was decayed into hadrons according to the best available measurements of the τ branching ratios [44]. The CTC and calorimeter signals produced by the secondary particles were modeled with the detector simulation program. The electron track and calorimeter cluster

Process	Number of Events in Final Sample		
	Lower Bound	Nominal Value	Upper Bound
$W \to e\nu$	$8.5 \pm 0.6 \pm 0.2$	$11.2 \pm 0.8 \pm 0.3$	$11.3 \pm 0.8 \pm 0.3$
$W \to \mu\nu$	$23.8 \pm 1.7 \pm 0.3$	$31.8 \pm 2.2 \pm 0.4$	$35.6 \pm 2.5 \pm 0.5$
$W \to \tau\nu$; $\tau \to$ hadrons[1]	$25.0 \pm 1.7 \pm 0.4$	$33.2 \pm 2.3 \pm 0.5$	$38.4 \pm 2.7 \pm 0.6$
$W \to \tau\nu$; $\tau \to$ hadrons[2]	$24.7 \pm 0.4 \pm 4.4$	$26.4 \pm 0.4 \pm 4.6$	$26.6 \pm 0.4 \pm 4.6$
$W \to \tau\nu$; $\tau \to \ell\nu_\ell\nu_\tau$	$10.9 \pm 0.8 \pm 0.1$	$13.0 \pm 0.9 \pm 0.2$	$15.5 \pm 1.1 \pm 0.2$
Total W Background:		$82.5 \pm 10.8 \pm 4.6$	
$Z^0 \to e^+e^-$	0.001 ± 0.0008 ± 0.004	0.001 ± 0.0008 ± 0.004	0.005 ± 0.0004 ± 0.002
$Z^0 \to \mu^+\mu^-$	$0.59 \pm 0.04 \pm 0.02$	$0.76 \pm 0.05 \pm 0.02$	$0.84 \pm 0.05 \pm 0.02$
$Z^0 \to \tau^+\tau^-$	$0.27 \pm 0.02 \pm 0.02$	$0.35 \pm 0.02 \pm 0.02$	$0.46 \pm 0.03 \pm 0.03$
Total Z Background:		$1.12 \pm 0.24 \pm 0.03$	
$Z^0 \to \nu\bar{\nu}$	$55.6 \pm 3.9 \pm 0.4$	$77.8 \pm 5.4 \pm 0.5$	$83.8 \pm 5.9 \pm 0.5$
$Z^0 \to \nu\bar{\nu}$ Signal:		$77.8 \pm 15.1 \pm 0.5$	

[1]Monte Carlo using the PAPAGENO event generator
[2]Monte Carlo based on the $W \to e\nu$ data set

Table 4.2: Results of Monte Carlo simulations of W and Z decays.

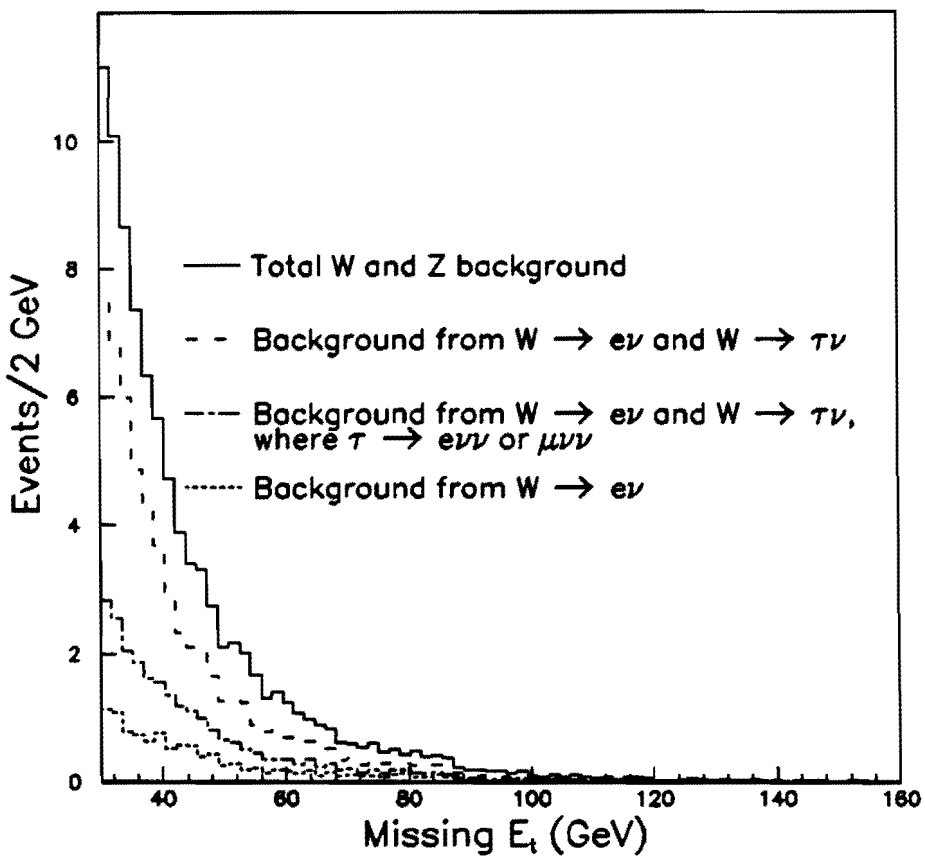

Figure 4.5: The $\not{E}_t$ spectrum of the total W and Z background from the PAPAGENO Monte Carlo, and the contributions to the $\not{E}_t$ spectrum from each of the W decay modes. The background from $Z^0 \to \ell^+\ell^-$ decays is very small, so that essentially all of the final contribution is from $W \to \mu\nu$.

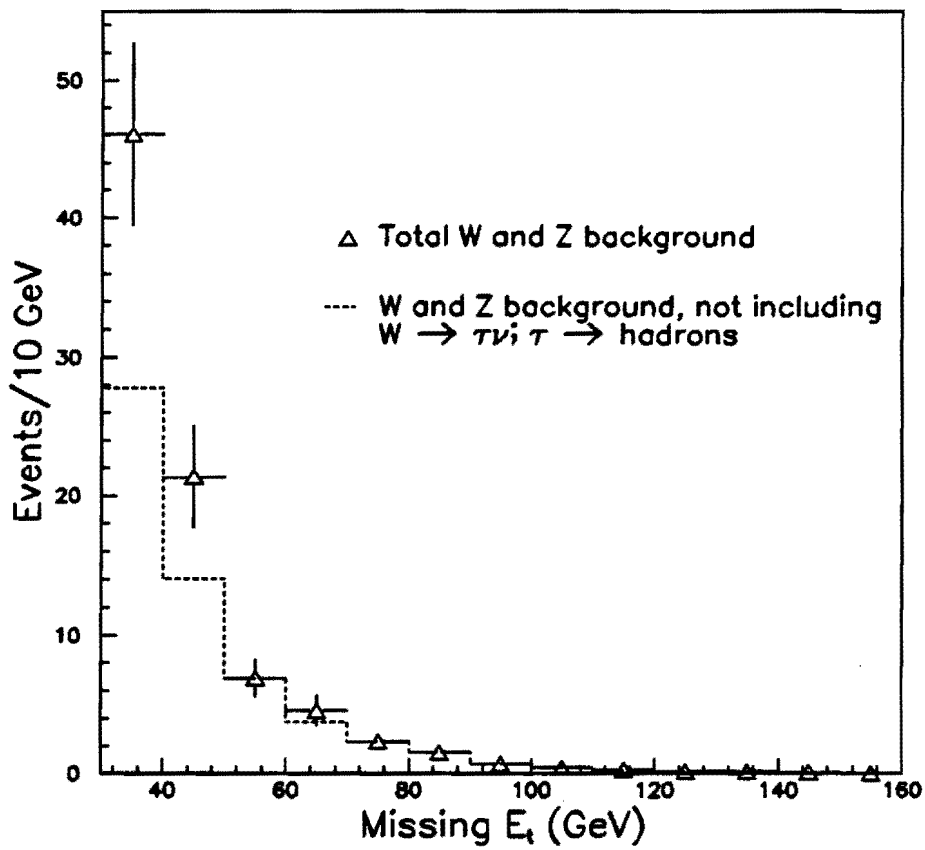

Figure 4.6: The estimated $\not{E}_t$ spectrum of the total W and Z background from all decay modes except $W \to \tau\nu$; $\tau \to$ hadrons (from the PAPAGENO Monte Carlo), and the contribution to the $\not{E}_t$ spectrum from hadronic decays of W taus estimated from the $W \to e\nu$ based Monte Carlo described in Section 4.5.1. These are the distributions used in calculating the final results of this study.

were then removed from the real event, and the simulated τ was substituted in their place. The event was then tested to see if it passed the monojet cuts.

If the number of fake $W \rightarrow \tau\nu$ events that pass our cuts in the ith $\not{E}_t$ bin is $N^{(i)}_{pass}$, then the expected number $N^{(i)}_{\tau}$ of τ background events in the ith bin is given by:

$$N^{(i)}_{\tau} = \frac{\mathcal{L}_{mon}}{\mathcal{L}_{We\nu}} * \epsilon^{(i)}_{trig} * BR * S * (1 - f_{back}) * A * N^{(i)}_{pass}$$

where

- $\frac{\mathcal{L}_{mon}}{\mathcal{L}_{We\nu}}$ is the ratio of the integrated luminosities of the monojet sample and the W electron sample.
- $\epsilon^{(i)}_{trig}$ is the $\not{E}_t$ trigger efficiency, determined from the empirical fit displayed in Figure 2.16.
- BR is the branching ratio for $\tau \rightarrow$ hadrons.
- S is a scale factor independent of bin which includes the efficiencies for the original $W \rightarrow e\nu$ selection cuts [34].
- f_{back} is the fraction of background events present in the W electron sample. Although these backgrounds are not expected to have exactly the same $\not{E}_t$ spectrum as $W \rightarrow \tau\nu$, the error introduced by making this assumption is small compared to the statistical uncertainty in this calculation.

Factor		Value
Luminosity Ratio	$\frac{\mathcal{L}_{mon}}{\mathcal{L}_{W e\nu}}$	1.18
Branching ratio for $\tau \rightarrow$ hadrons	BR	0.639
$W \rightarrow e\nu$ efficiencies	S	1.19 ± 0.05
$W \rightarrow e\nu$ background fraction	f_{back}	0.069 ± 0.013
Ratio of acceptances	A	1.23

Table 4.3: Summary of factors in the τ background calculation.

- A is the ratio of the geometrical acceptance for $W \rightarrow \tau\nu$ to the acceptance for $W \rightarrow e\nu$.

The numerical values of those factors which are independent of $\not{E}_t$ are summarized in Table 4.3.

We can test the efficacy of our τ Monte Carlo technique by comparing the monojet candidates rejected by our τ cuts to the Monte Carlo events rejected by these cuts. Histograms of the τ cluster properties are shown in Figure 4.7 and compared with results from our Monte Carlo. The good agreement between the data and Monte Carlo verifies our technique and implies that the monojet candidates rejected are predominately taus.

The number of background events predicted by these simulations is listed in Table 4.2, and the estimated $\not{E}_t$ spectrum of the background is shown in Figure 4.8. The upper and lower systematic bounds listed in Table 4.2 were obtained

by varying the calorimeter energy scale used in simulating the τ decay products by $\pm 5\%$, and the systematic uncertainties quoted for these numbers include the uncertainty in the trigger efficiency and the uncertainties in the quantities listed in Table 4.3. Also shown in Figure 4.8 is the $\not{E}_t$ spectrum of the tau background predicted by the PAPAGENO event generator and the MRSB structure functions. The close agreement between the results from the $W \rightarrow e\nu$ based tau Monte Carlo and the PAPAGENO event generator gives us additional confidence that our simulations of W decays are realistic.

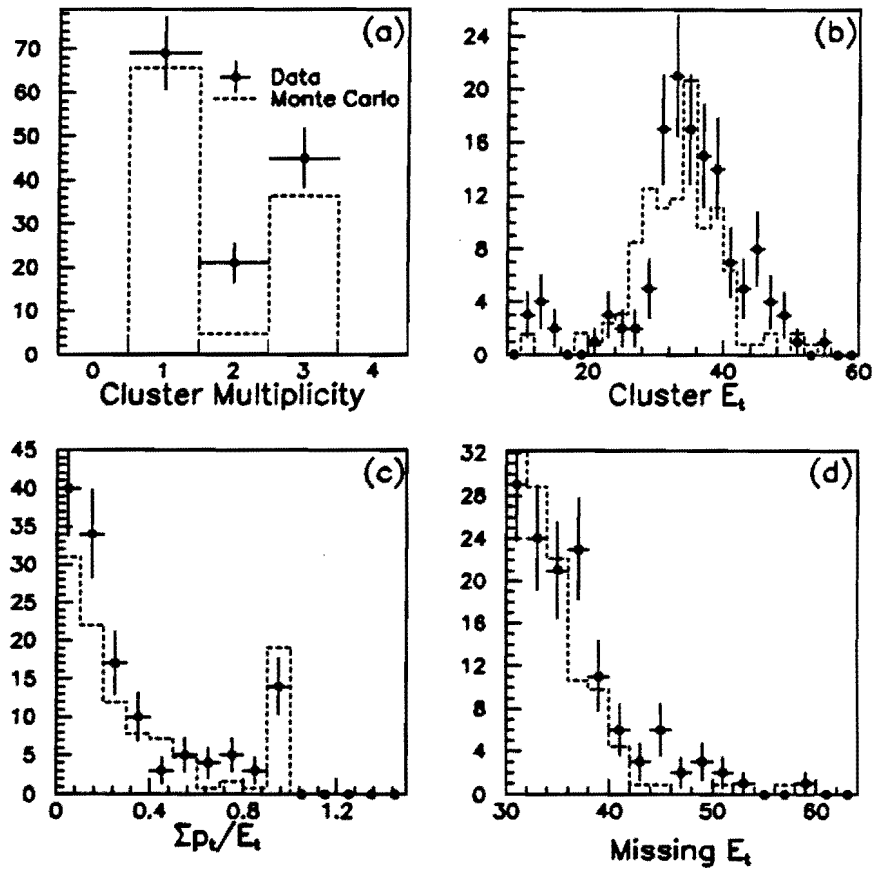

Figure 4.7: Comparison of data and $W \rightarrow e\nu$ based Monte Carlo for monojet candidates rejected by tau cuts. The quantities displayed are (a) charged multiplicity of the cluster, (b) cluster E_t, (c) ratio of scalar sum of track p_ts to cluster E_t and (d) $\not{E}_t$ of the τ candidates.

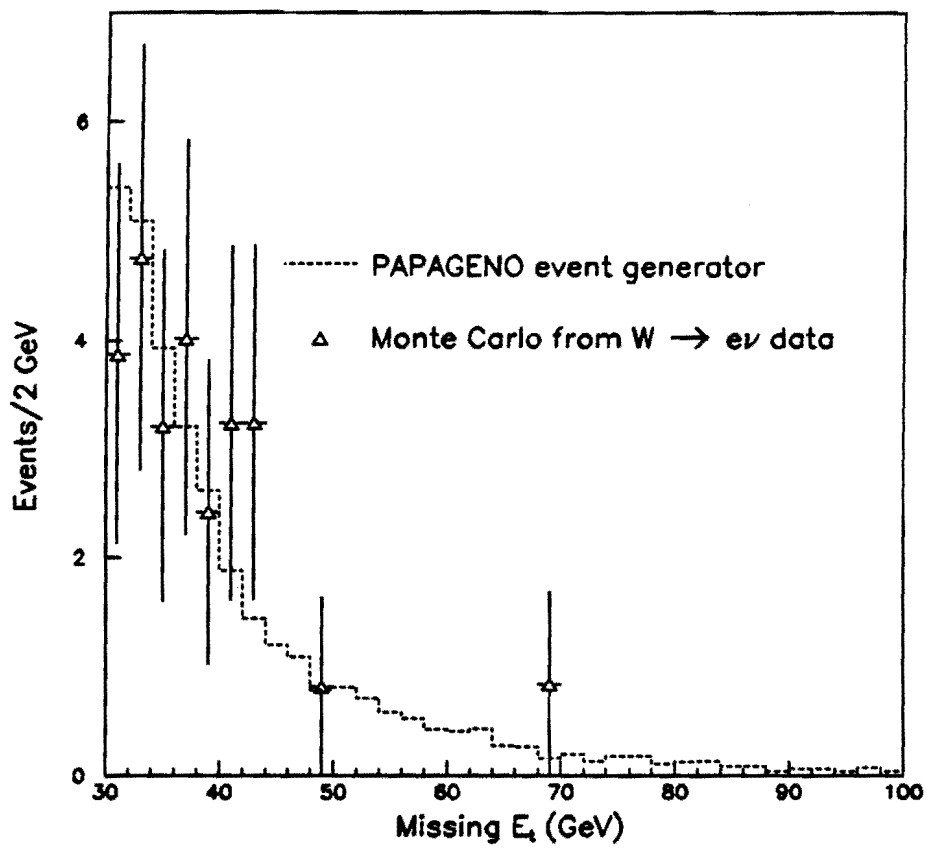

Figure 4.8: Results of simulations of the $W \rightarrow \tau\nu$; $\tau \rightarrow$ hadrons background using the PAPAGENO event generator and $W \rightarrow e\nu$ data set. Both plots are normalized to the integrated luminosity of the monojet sample (4.7 pb^{-1}).

Chapter 5

QCD Backgrounds

A false $\not{E}_t$ signal can be caused by energy leakage in the CDF calorimetry. Detector regions where energetic particles from the vertex may not produce calorimetry signals can be seen in Figure 5.1. These histograms show the distribution in η-φ space of the smaller cluster in events with two back-to-back jets with $f_2 < 50\%$ where f_2 is the fraction of the smaller jet's true energy that is actually seen by the calorimeters. The quantity f_2 is roughly given by $f_2 = E_t^{(2)}/E_t^{(1)}$, where $E_t^{(1)}$ and $E_t^{(2)}$ are the transverse energies of the larger and smaller cluster respectively. But f_2 can be measured more accurately by assuming that the transverse energy leakage is equal to the projection of the $\not{E}_t$ vector along the axis of the second jet [46], and we use this method instead.

Note how the mismeasured jets in Figure 5.1 are concentrated in the regions $\eta \approx 0$, $|\eta| \approx 1.1$, and $|\eta| \approx 2.2$. The energy leakage in these regions is a consequence of the mechanical structure of the calorimetry system, shown in

Figure 2.8. There is a crack at $\theta = 90°$ (at the left-hand edge of tower 0 in the diagram) where the central arches meet. Because of this crack, jets at $\eta \approx 0$ are poorly measured. Between towers 6 and 11, energy is lost in the dead space between the central arch and the endwall. The leakage is worst between towers 9 and 11, where there is a dead region caused by the end of the solenoid and a crack at $\theta = 30°$ between the endwall and the plug. Energy lost in these regions produces the mismeasured jets at $|\eta| \approx 1.1$, and we call this part of the calorimeter the 30° crack region. The edge of the plug at $\theta = 10°$ is not fully instrumented, and energy is lost here and in the gap between the plug and the forward calorimeters (not shown in Figure 2.8.) This causes the peaks in Figure 5.1(b) at $|\eta| \approx 2.2$, and these areas of the detector are referred to as the 10° crack regions.

In addition to the η cracks apparent in Figure 5.1, there are gaps in the central calorimetry caused by the 15° azimuthal segmentation. In Figure 5.2 we display a histogram of the φ coordinate, folded by 15°, of the smaller jet in the unbalanced dijet events of Figure 5.1 when the smaller jet is in the region $0.1 < |\eta| < 0.9$. In this plot, 0° and 15° correspond to the φ limits of the calorimeter wedges. An excess of events at the edges, relative to the center of the wedge, can be seen.

While we were able to use Monte Carlo simulations to estimate backgrounds from vector bosons, a similar approach to QCD backgrounds is not feasible. Existing Monte Carlo event generator programs are adequate for simulating the typical jets observed by CDF, and the detector simulation package realistically

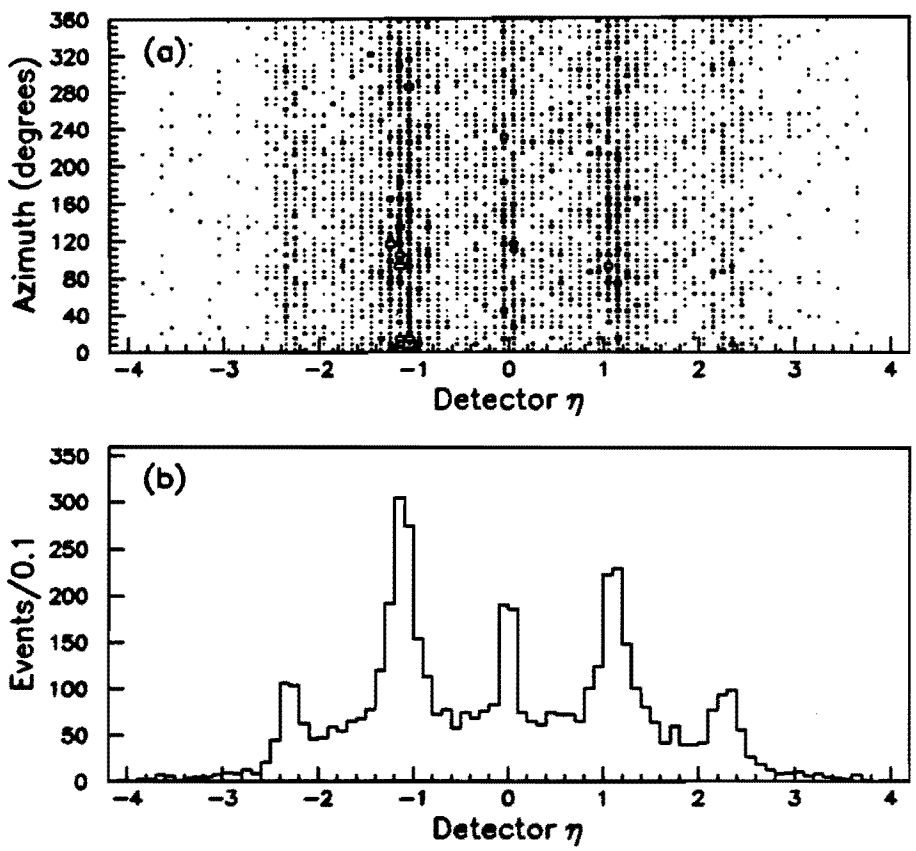

Figure 5.1: Distribution in (a) η-φ and (b) η of the centroid of the smaller jet in mismeasured dijet events.

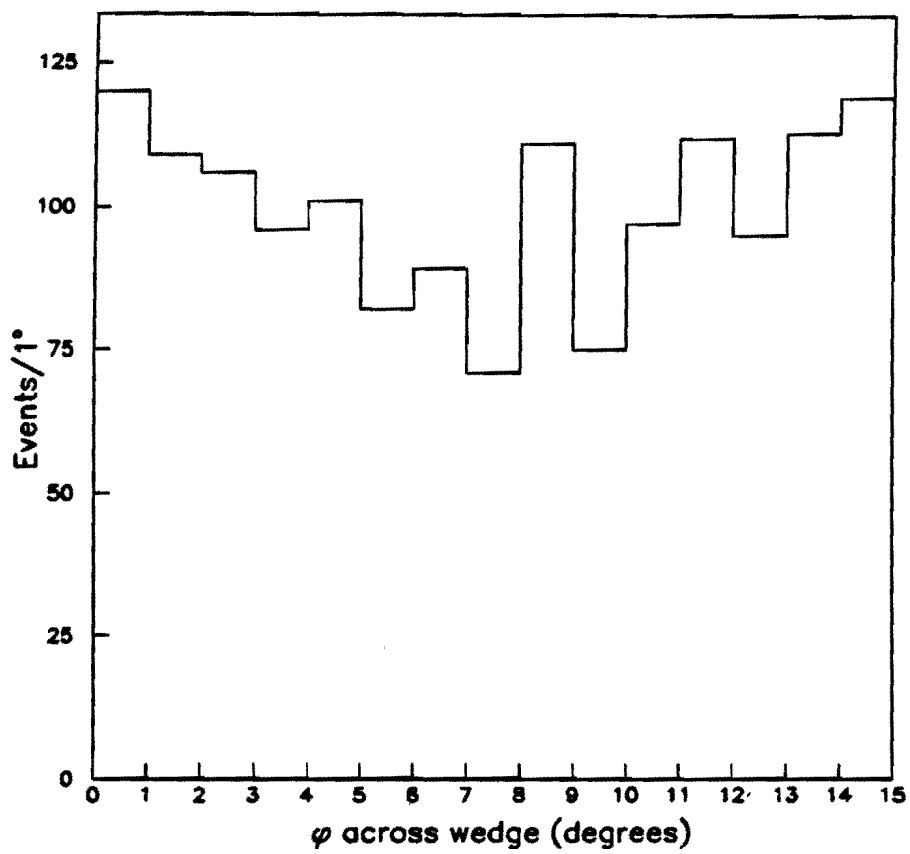

Figure 5.2: Azimuthal coordinate (modulo 15°) of central poorly measured jets.

models calorimeter flaws. But jets lost in cracks and dead regions represent rare and pathological cases of the fragmentation process and calorimeter response. Therefore, our techniques for estimating QCD monojet backgrounds are based entirely on studies of real CDF data.

In the sections below we present estimates of the number of fake monojet events in the data set that are actually QCD jet events.

5.1 Dijet Backgrounds

Figure 5.3 shows Feynman diagrams for some of the lowest order QCD subprocesses in parton-parton elastic scattering. The two scattered partons produced in these subprocesses fragment to form hadronic jets. As we mentioned in our discussion of the kinematics of the parton model in Chapter 4, the jets are 180° apart in φ but their η coordinates are not necessarily correlated. Dijet production dominates the jet cross section, and it is reasonable to expect that it will produce most of the QCD background in the monojet sample.

5.1.1 Identifying Dijet Events with the CTC and VTPC

In Section 3.7 we described the procedure for using data from the CTC to identify lost jets. We have also developed a similar algorithm that uses VTPC data to identify jets that are lost in the regions beyond the acceptance of the CTC. These track clustering algorithms provide the basis for software used to estimate the amount of residual dijet background in the final data set.

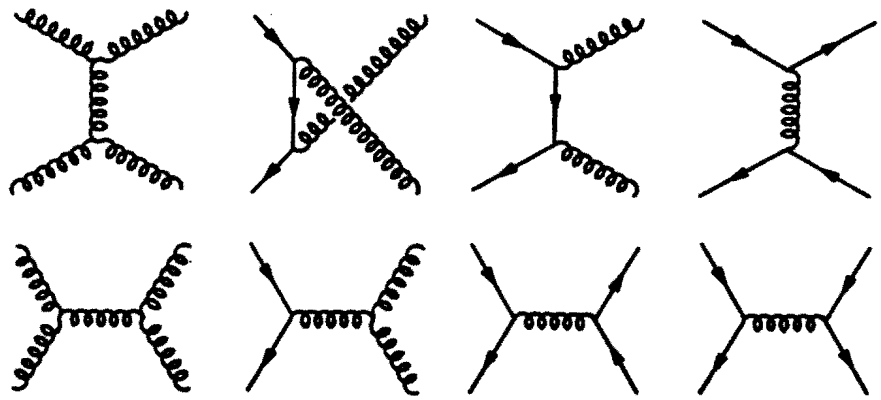

Figure 5.3: Some of the lowest order QCD Feynman diagrams for parton-parton elastic scattering. The solid lines represent quark and antiquark states. The dominant contributions come from the gluon-gluon interactions.

Using tracking information to locate lost jets works best in the central region where the CTC provides momentum measurement. Events with CTC track clusters that fail our cuts are almost certainly dijet events and can be removed from the data sample. The VTPC, however, is a much less effective tool for detecting lost jets. Track clustering in the VTPC is not precise enough to discriminate between monojet signal and dijet background on an event by event basis. Events with VTPC track clusters that fail our cuts are only more likely to be dijet background than events without such track clusters. Therefore, we do not use VTPC data to reject specific events. Instead, we use the number of events rejected by the VTPC track clustering cuts to estimate the fraction of monojet events that are actually dijet background.

The algorithm first searches for a lost jet in the central region. If no cluster of CTC tracks is found which satisfies the criteria outlined in Section 3.7, then the VTPC data in the region $|\eta| > 1.0$ is searched for a track cluster back-to-back with the leading jet. Since the VTPC cannot measure curvature for tracks with $p_t > 300$ MeV, we can only cut on the number of tracks in a cluster and not on $\sum p_t$. The lack of momentum information is one of the reasons VTPC track clustering is not as effective as CTC track clustering in identifying lost jets. Another impediment to finding lost jets in the VTPC is that many of the VTPC tracks lack a precise measurement of their φ coordinates.

The method used for finding track clusters in the VTPC is similar to the clustering procedure for the CTC. Three dimensional tracks opposite in φ to the leading cluster within $\pm 30°$ are used as seed tracks. The centroid is calculated by averaging the η and φ coordinates of the three-dimensional tracks in the cluster. Two-dimensional tracks are included in the cluster if they are within $|\Delta\eta| < 0.7$ of the centroid, and if they are in the same octant as the centroid or its nearest neighbor. The algorithm searches for the cone with the greatest number of tracks. The forward and backward ($\eta > 1.0$ and $\eta < -1.0$) regions are searched separately. The event is considered a dijet if the cluster with the most tracks is opposite to the leading cluster within $\pm 30°$, and the number of tracks in the cone is greater than or equal to some number denoted by N_{cut}^{VTPC}. The event is not rejected if track clusters of equal multiplicity are found in both the forward and backward regions. We varied the cut on the number of tracks from

3 to 10, and we quote results below for each value of N_{cut}^{VTPC}.

5.1.2 Estimating Dijet Backgrounds from Tracking Information

The amount of dijet background in the monojet sample can be estimated from the numbers of events rejected by the CTC and VTPC track cluster cuts. We can do this if we know the probabilities for the algorithm to identify a real dijet event or to mistakenly reject a monojet event. We call the former probability the true positive rate (TPR), and the latter probability the false positive rate (FPR). The calculation of the dijet background proceeds in the following manner.

For convenience, we divide the detector into three η regions: $|\eta| < 1.0$, $1.0 < |\eta| < 1.5$, and $|\eta| > 1.5$. We refer to these regions as Regions 0,1, and 2 respectively.

We can group all the events in the data set into four categories. Dijet background events are classified by the region in which the jets are lost. We will denote the number of dijet events with jets lost in Regions 0,1, and 2 by D_0, D_1, and D_2 respectively. The fourth category includes true monojets, W backgrounds, and all other residual backgrounds. Let N_{mon} represent the number of events in this group.

We define the following set of probabilities:

C_i = Probability for CTC track clustering to identify a jet lost in Region i, $i = 0, 1, 2$.

V_i = Probability for VTPC track clustering to identify a jet lost in Region i, $i = 0, 1, 2$.

F_{C0}, F_{C1} = Probability for CTC track clustering to find a fake track cluster in Regions 0,1 in a real monojet event.

F_V = Probability for VTPC cuts to reject a real monojet event.

The probabilities $\{C_i, V_i;\ i = 0, 1, 2\}$ are the true positive rates, and the probabilities $\{F_{C0}, F_{C1}, F_V\}$ are the FPRs. We have not included in our definitions the probability for the CTC track clustering to find a false track cluster in Region 2 in a genuine monojet event. Because the CTC tracking efficiency falls off sharply beyond $|\eta| = 1.0$, this probability is effectively zero. The probability C_2 is negligibly small for the same reason.

The η resolution of the CTC track clustering is adequate to discriminate between jets in different η regions. Let N_0 and N_1 denote the number of events with jets in Regions 0 and 1 that are rejected by the CTC cuts. In the VTPC, however, track clusters do not reliably point towards lost jets. Therefore, we do not use the η information provided by VTPC track clustering. Let N_V denote the number of events rejected by the VTPC cuts in all three η regions. The total number of events in the data is represented by N_{total}.

The numbers $\{N_{total}, N_0, N_1, N_V\}$ are related to $\{N_{mon}, D_0, D_1, D_2\}$ by the

following set of equations:

$$N_{total} = N_{mon} + D_0 + D_1 + D_2 \tag{5.1}$$

$$N_0 = F_{C0} N_{mon} + C_0 D_0 \tag{5.2}$$

$$N_1 = F_{C1} N_{mon} + C_1 D_1 \tag{5.3}$$

$$N_V = F_V(1 - F_{C0} - F_{C1}) N_{mon} + V_0(1 - C_0) D_0 + V_1(1 - C_1) D_1 + V_2 D_2 \tag{5.4}$$

The factors of $(1 - F_{C0} - F_{C1})$, $(1 - C_0)$ and $(1 - C_1)$ in the last equation arise from the fact that each event is first tested against the CTC cuts and then against the VTPC cuts.

Once we have determined the probabilities $\{F_{C0}, F_{C1}, F_V, C_i, V_i;\ i = 0, 1, 2\}$ for a given set of cuts, and the number of events rejected by these cuts, we only need some simple algebra to determine the dijet backgrounds $\{D_0, D_1, D_2\}$. An implicit assumption behind this calculation is that the algorithm's rejection rates for genuine monojets are the same as the rejection rates for non-dijet residual backgrounds. We examine this assumption below.

In the following sections we present estimates of the various probabilities and describe the techniques used in determining them.

5.1.3 Dijet Detection Efficiency

To measure the efficiency for our algorithm to identify dijet background, we tested it on a sample of unbalanced dijets similar to the data shown in Figure 5.1. We selected back-to-back dijet events that satisfied the following criteria:

- The event had $0.2 < f_2 < 0.5$. Requiring the second jet to have at least 20% of its energy detected excludes monojets and other electroweak processes from the sample.

- The EM fraction of the second cluster was less than 85%. This excluded from the sample events with direct photons and isolated neutral hadrons. Backgrounds from lost photons and neutral hadrons were estimated separately (see Chapter 6.)

- The event passed our monojet cuts when the smaller cluster was removed.

From a sample of about 3×10^5 QCD events, 506 events were found that satisfied these requirements.

Since the smaller jets in the unbalanced dijet sample have already lost most of their energy in calorimeter cracks, we expect them to have similar characteristics to the lost jets in our dijet background. In particular, the smaller jets in unbalanced dijet events have on the average fewer particles than jets well measured by the calorimeters. For dijet events with $0.2 < f_2 < 0.5$ that have the smaller cluster in the central region, the average number of CTC tracks associated with the second jet is 5.7. This compares to an average of 8.1 CTC tracks for jets in well-measured dijet events ($f_2 > 0.8$). Clearly, lower multiplicity jets are more likely to be lost in cracks than jets with many particles.

The efficiencies for the CTC and VTPC track cluster algorithms to identify dijets, as a function of the η coordinate of the smaller jet, are displayed in Figure

5.4. Figure 5.4(a) shows that the nominal CTC cuts (≥ 2 tracks, $\sum p_t/E_t^{(1)} \geq 0.3$) identify jets with nearly 100% efficiency in Region 0. The efficiency falls off for $|\eta| > 1$, but it is still possible for the CTC to detect jets in Region 1. The number of events with jets in the region $|\eta| > 1.5$ that are detected by the CTC is very small and can be neglected. Figure 5.4(b) shows the VTPC jet identification efficiency for a cluster multiplicity cut of 6. The algorithm is most efficient in Region 2, where it detects 60% of the jets. Although only VTPC tracks with $|\eta| > 1$ are used in clustering, the algorithm will still find track clusters with multiplicities of 6 or more in 15% of the events with a jet in Region 0. This high probability for finding random clusters of tracks shows that track clustering in the VTPC is only a rough tool for locating lost jets.

5.1.4 Calculating the True Positive Rates

The true positive rate for a track clustering algorithm in a given η region is the average probability for the code to find lost jets in that region. Since we expect the lost jets in the dijet background to be clustered around the η cracks, the test sample of unbalanced dijets is the appropriate data set to use in measuring the true positive rates $\{C_i, V_i;\ i = 0, 1, 2\}$. In Table 5.1 we display the TPR in each η region for the CTC nominal cuts and various values of N_{cut}^{VTPC}.

Our studies of the CTC and VTPC track clustering algorithms show that the probability of detecting a jet is nearly independent of the transverse energy of the jet. Therefore, it is not important that the jets in our test sample of unbalanced

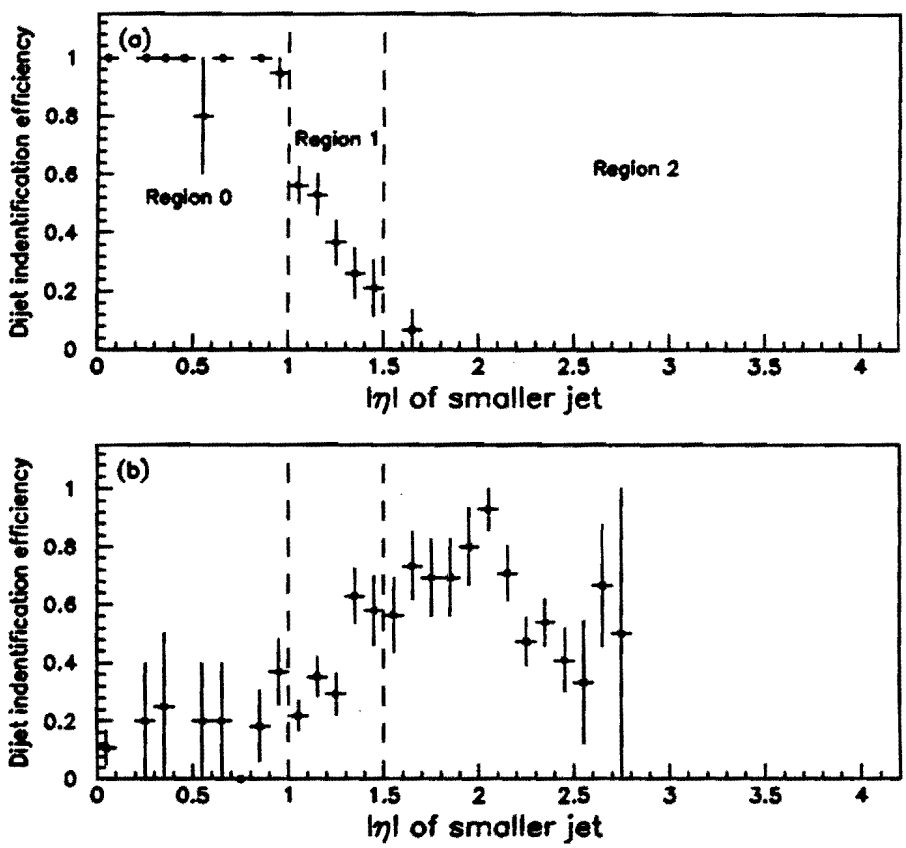

Figure 5.4: Dijet identification probability for (a) CTC track clustering and (b) VTPC track clustering with $N_{cut}^{VTPC} = 6$.

N_{cut}^{VTPC}	η Region		
	0	1	2
3	0.516 ± 0.064	0.668 ± 0.033	0.826 ± 0.024
4	0.387 ± 0.062	0.569 ± 0.035	0.789 ± 0.026
5	0.290 ± 0.058	0.495 ± 0.035	0.702 ± 0.029
6	0.145 ± 0.045	0.337 ± 0.033	0.599 ± 0.031
7	0.097 ± 0.038	0.272 ± 0.031	0.488 ± 0.032
8	0.065 ± 0.032	0.163 ± 0.026	0.368 ± 0.031
9	0.032 ± 0.023	0.104 ± 0.022	0.240 ± 0.028
10	0	0.064 ± 0.017	0.157 ± 0.023
CTC cuts	0.984 ± 0.016	0.510 ± 0.035	0

Table 5.1: True positive rates for various values of N_{cut}^{VTPC} and the nominal CTC cuts. The errors represent statistical uncertainties.

dijets have exactly the same E_t spectrum as the dijet background.

5.1.5 Calculating the False Positive Rates

We have measured from Monte Carlo data the probability for the CTC cuts to reject a true monojet event, and we display the results in Table 5.2. The probabilities shown in this table and in Table 5.3 are the sum $F_{C0} + F_{C1}$. This sum represents the probability for the algorithm to find a fake track cluster in

N_{cut}^{CTC}	$\sum p_t/E_t^{(1)}$ Cut		
	0.10	0.20	0.30
1	0.048	0.0031	0.0019
2	0.044	0.0029	0.0019
3	0.034	0.0026	0.0015

Table 5.2: False positive rates for CTC cuts determined from $Z^0 \rightarrow \nu\bar{\nu}$ Monte Carlo.

either Region 0 or 1. The Monte Carlo data show that if we require the p_t of the track cluster be at least 20% of the E_t of the leading jet, then the false positive rate is only a few tenths of a per cent. This probability is negligibly small.

To determine the FPR for the VTPC cuts, we used real W and Z events from the CDF data in which the bosons decayed into electrons or muons. The p_t spectrum and underlying event characteristics of Ws are nearly identical to those of Zs. We tested our algorithm on those events that pass our monojet cuts after the charged leptons have been removed. This data set contains 175 events and has a negligible amount of background from processes other than IVB decays. The VTPC TPRs measured from these data are displayed in Table 5.3. When we tested the CTC track clustering on the W and Z data, we found that the nominal cuts rejected a single event. This event could be either a false positive or an actual dijet background.

N_{cut}^{VTPC}	False Positive Rate
3	0.451 ± 0.0014
4	0.314 ± 0.0012
5	0.189 ± 0.0009
6	0.109 ± 0.0006
7	0.063 ± 0.0003
8	0.017 ± 0.0001
9	0.006
10	0.006

Table 5.3: False positive rates for various values of N_{cut}^{VTPC} measured from W and Z data. The errors represent statistical uncertainties. For $N_{cut}^{VTPC} \geq 9$, only a single event was rejected.

Most of the events in the final monojet data set are W and Z decays, and the dijet identification code cannot distinguish between Ws, monojets, and other decay modes of the Z. After electroweak processes and dijets, the process that appears most often in the data set is direct photon production. We can test our assumption that the same false positive rates apply for all non-dijet processes by comparing the FPRs for W and Z events to the FPRs for direct photon backgrounds. We used a sample of 540 CDF events with high-p_t photons in the central region to measure the FPRs for direct photon events. These events pass our monojet cuts when the photon is removed. The CTC false positive rates for direct photons are listed in Table 5.4. The data show that if we put a cut on the p_t of the track cluster at 30% of the E_t of the leading jet, then the CTC FPR will again be small enough to be neglected. In Figure 5.5 we compare the VTPC false positive rates for vector boson decays to the FPRs for direct photon events. Within statistical errors, the probabilities for the two types of events are in close agreement.

5.1.6 The Estimated Dijet Background

In Section 3.7 we described the CTC track clustering cuts and stated that these cuts rejected 3 events. All of these events are in Region 1. We insert these results into Equations 5.2 and 5.3 along with the measured probabilities $F_{C1} \approx 0$ and $C_1 = 0.51$ to obtain

$$D_0 = 0$$

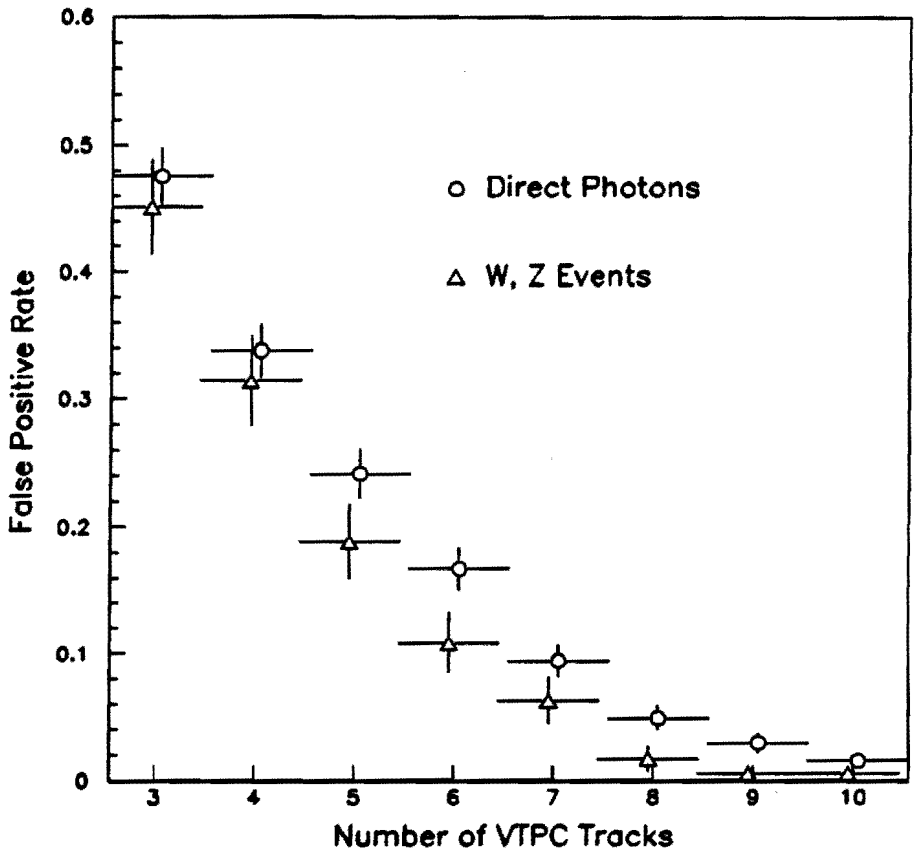

Figure 5.5: VTPC dijet identification false positive rates for IVB decays and direct photon background for values of N_{cut}^{VTPC} from 3 to 10. The error bars represent statistical uncertainties.

N_{cut}^{CTC}	$\sum p_t/E_t^{(1)}$ Cut		
	0.10	0.20	0.30
1	0.183 ± 0.0171	0.029 ± 0.0075	0.004 ± 0.0028
2	0.175 ± 0.0169	0.028 ± 0.0073	0.002 ± 0.0020
3	0.153 ± 0.0160	0.024 ± 0.0067	0.002 ± 0.0020

Table 5.4: False positive rates for CTC cuts determined from direct photon data. The errors represent statistical uncertainties.

and

$$D_1 = 5.9 \pm 0.41 \text{ (sys.)} \ \pm 3.4 \text{ (stat.)}$$

where the systematic error is from the uncertainty in the value of C_1. We therefore expect the dijet background in Region 1 to be 6 events, before we apply the CTC cuts. After we remove the three events flagged as dijets by the CTC, we estimate that the final data set contains a residual background of 3 ± 3 dijet events with jets lost in Region 1.

Table 5.5 shows for each value of N_{cut}^{VTPC} from 3 to 10 the number of events rejected by the VTPC algorithm, and the calculated values for N_{mon} and D_2. All the results in this table are consistent within the estimated errors. The smallest error is for $N_{cut}^{VTPC} = 8$. To further elucidate our method for determining the dijet backgrounds, we present the details of the calculation of N_{mon} and D_2 for the cut $N_{cut}^{VTPC} = 8$.

The data set contains 229 events before the CTC dijet cuts are applied, so that $N_{total} = 229$. Equation 5.1 and the CTC results quoted above therefore give

$$223 = N_{mon} + D_2.$$

For $N_{cut}^{VTPC} = 8$, the VTPC clustering algorithm identifies 14 events as possible dijet background. We therefore substitute the CTC results and the values for F_V, V_1, C_1 and V_2 from Tables 5.1 and 5.3 into Equation 5.4 to obtain

$$14 = 0.017 * N_{mon} + 0.16 * (1 - 0.51) * 6 + 0.37 * D_2.$$

(Recall that $F_{C2} \approx 0$.) These two equations can be solved for N_{mon} and D_2 to yield

$$N_{mon} = 195 \pm 0.46 \text{ (sys.)} \pm 11 \text{ (stat.)}$$

and

$$D_2 = 28 \pm 0.20 \text{ (sys.)} \pm 11 \text{ (stat.)}.$$

The systematic errors are calculated from the uncertainties in the probabilities. The errors in our final results are dominated by the statistical uncertainties in the number of events rejected by the cuts.

We also used the unbalanced dijet sample to produce an approximate $\not{E}_t$ spectrum of the dijet background. For each unbalanced dijet event we calculated $\not{E}_t'$, the amount of transverse energy that would have been missing if the second cluster had not been present:

$$\not{E}_t' = |\vec{\not{E}}_t + \vec{E}_t^{(2)}|.$$

N_{cut}^{VTPC}	Number of events rejected	Number of non-dijet events	Number of dijet events with jets lost in Region 2
3	105	216.8 ± 27.7	6.3 ± 27.4
4	85	195.2 ± 19.7	27.9 ± 19.4
5	64	183.2 ± 15.9	39.9 ± 15.6
6	45	182.7 ± 14.1	40.4 ± 13.7
7	25	199.1 ± 12.3	24.0 ± 11.8
8	14	195.4 ± 11.2	27.7 ± 10.7
9	9	191.4 ± 13.3	31.7 ± 12.8
10	5	199.7 ± 15.2	23.4 ± 14.8

Table 5.5: For each value of N_{cut}^{VTPC}: the number of events rejected by the VTPC track clustering algorithm (N_V), the estimated number of non-dijet events (N_{mon}), and the estimated number of dijet events with jets lost in Region 2 (D_2). We quote the results for $N_{cut}^{VTPC} = 8$ as our measured values for N_{mon} and D_2.

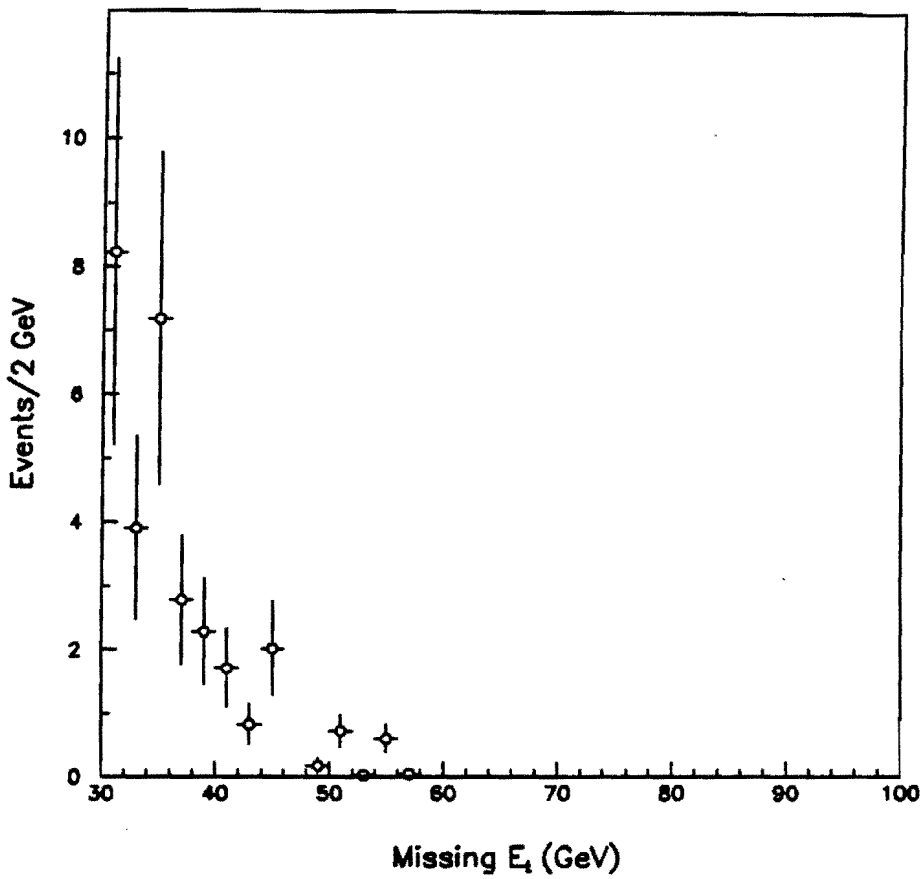

Figure 5.6: Expected $\not{E}_t$ spectrum for the dijet background, assuming $D_0 = 0$, $D_1 = 3$, and $D_2 = 28$.

The $\not{E}_t'$ values were entered on histograms to form three $\not{E}_t'$ distributions, corresponding to the η regions that the second clusters were in. We expect the $\not{E}_t$ spectrum of the dijet background in each η region to have the same shape as the $\not{E}_t'$ distribution for that region.

Figure 5.6 shows the $\not{E}_t'$ spectrum for the mismeasured dijets, folded with the $\not{E}_t$ trigger efficiency shown in Figure 2.16 and normalized to 3 events with the second cluster in Region 1 and 28 events with the second cluster in Region 2. The error bars represent the sums in quadrature of the statistical uncertainties in the unbalanced dijet sample, the uncertainties in the dijet background and the uncertainties in the $\not{E}_t$ trigger efficiency.

As we found in the case of the W and Z backgrounds, most of the dijet background events have low missing E_t. Again, this is consistent with the data of Figure 3.15.

5.2 Multijet Backgrounds

An event with three or more QCD jets can mimic a monojet if one or more of the jets are badly measured or lost entirely. Figure 3.5 is an example of a trijet event with poorly measured energy flow. A cluster with $E_t = 13.8$ GeV is seen at the position $\eta = -0.85$, $\varphi = 289°$. But there is also a CTC track with $p_t = 20.5$ GeV at $(\eta, \varphi) = (-0.89, 290°)$. The energy from this particle was probably lost in the 30° crack region. Only the presence of this single CTC track prevented

the event from being included in the monojet sample.

Multijet QCD background events in the monojet sample can be grouped into four categories, depending on how many jets are lost or mismeasured:

1. All the jets in the event are detected, but one jet is poorly measured.
2. A single jet in the event is lost completely.
3. All the jets in the event are detected, but two or more jets are badly measured.
4. Two or more jets are lost completely.

In rejecting dijet background, we discarded events that had clusters with $E_t > 5$ GeV back-to-back with the leading cluster. We apply the same criteria here for discriminating between jets that have been poorly measured and jets that have been lost completely. If a high-E_t jet is reconstructed as a cluster with $E_t < 5$ GeV, or not reconstructed at all, it is considered to be lost. A cluster with $E_t > 5$ GeV is considered to possibly be the remnant of a higher energy jet.

We have searched the data for anomalies that would indicate the presence of multijet QCD backgrounds. In the sections below we present estimates for the number of background events in each of the four categories.

5.2.1 Multijet Events with One Jet Lost or Mismeasured

If the missing E_t in an event is due to a jet that has lost most of its energy in a crack, but has still been reconstructed as a cluster in the calorime-

ters, then the $\not{E}_t$ vector will point towards that cluster. We looked for correlations between the missing E_t direction and the azimuthal coordinates of the second and third clusters, in events with three or more energy clusters with transverse energies greater than 5 GeV. The data contain 56 such events. In Figure 5.7 we display histograms of the azimuthal separations between the $\not{E}_t$ vector and the second and third clusters. The histograms show no peaks at 0° that would be caused by badly measured jets. A histogram of $\Delta\varphi$ between the $\not{E}_t$ vector and the fourth cluster, for the 22 events in the data that have four or more clusters with $E_t > 5$ GeV, is shown in Figure 5.8. Again there is no peak at 0°.

The data of Figures 5.7 and 5.8 are consistent with zero multijet background events from Category 1. However, Figure 5.7 shows that there are three events with $\Delta\varphi$ between the $\not{E}_t$ vector and the third cluster less than 20°. These events could possibly be background. We conclude that the lower and upper bounds on the background from multijet events with one jet mismeasured are 0 and 3 events.

Since it is more likely for a jet hitting a crack to be partially reconstructed than to disappear entirely, the lack of evidence for multijet backgrounds with one mismeasured jet implies that there is no significant background from multijet events with a single lost jet. We therefore conclude that the lower bound on the multijet background from Category 2 is zero events. If events of this type are present in the data set, however, there is no way we could detect them. But we

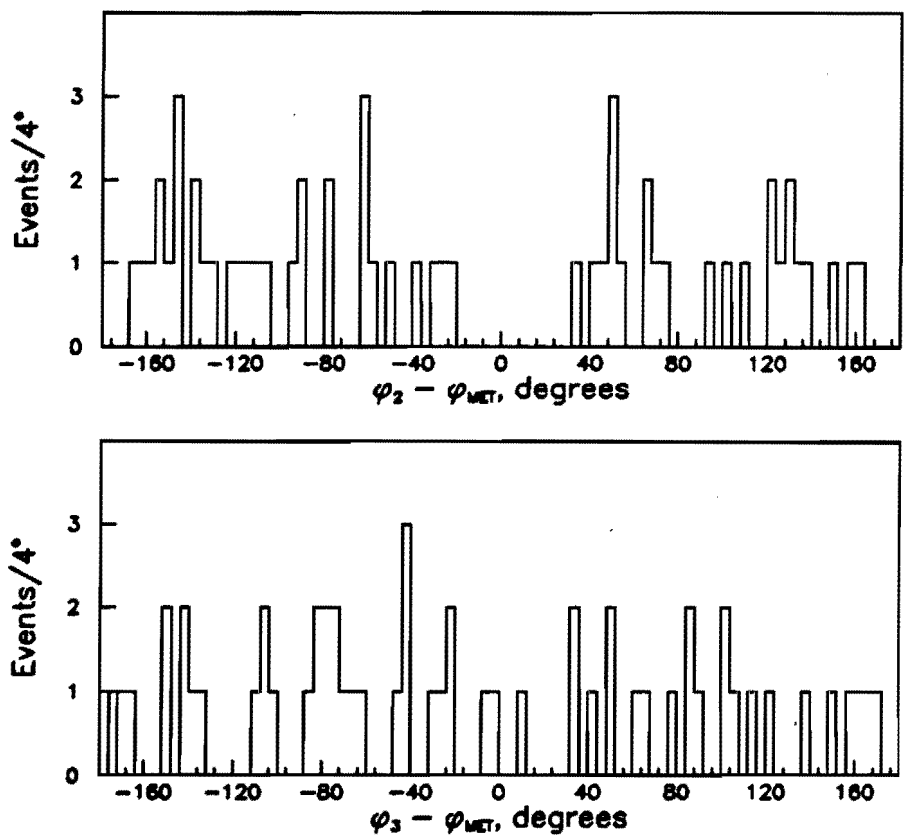

Figure 5.7: Histograms of the differences between the azimuthal angle of the $\not{E}_t$ vector (φ_{MET}) and the azimuthal positions of the second and third clusters (φ_2, φ_3) for events with three or more clusters with $E_t > 5$ GeV.

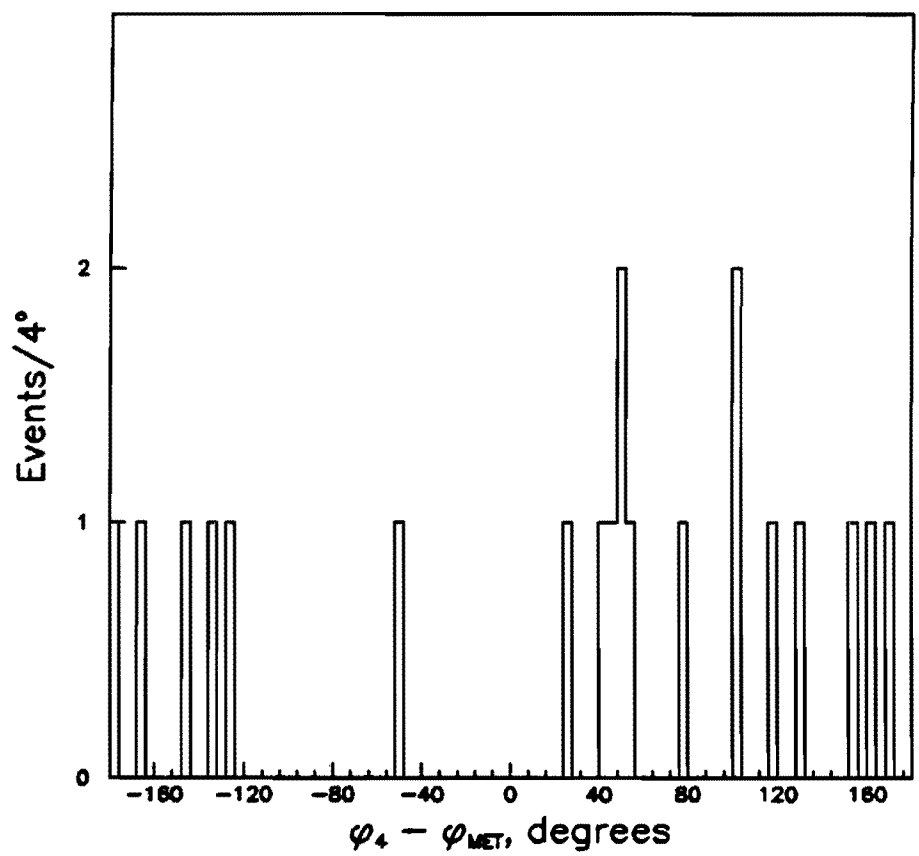

Figure 5.8: Histogram of the difference between the azimuthal angle of the $\not{E}_t$ vector and the azimuthal position of the fourth cluster for events with four or more clusters with $E_t > 5$ GeV.

can roughly estimate how many multijet events with lost jets we might expect in the data. The trijet cross section is approximately a factor of α_s smaller than the dijet cross section; therefore, one might naively expect the trijet background to be about a factor of α_s smaller than the dijet background. For $\alpha_s \approx 0.10$, this gives about 4 events. A conservative estimate of the upper bound on the multijet background with one jet lost is 5 events. We conclude that the total residual background from multijet events with one jet lost or mismeasured is 4 ± 4 events.

5.2.2 Multijet Events with Two or More Jets Lost or Mismeasured

If calorimeter flaws have caused more than one jet to be mismeasured, then the $\not{E}_t$ vector will not necessarily point towards a particular cluster. However, events of this type will tend to have more than one cluster in known crack regions. Referring to Figure 5.1, we define the η boundaries of the crack regions:

- 90° crack: $|\eta| < 0.2$
- 30° crack: $0.8 < |\eta| < 1.3$
- 10° crack: $2.1 < |\eta| < 2.5$

We measured the fraction of events in the monojet sample with three or more clusters that have at least two clusters in crack regions. These data are listed in Table 5.5 for each combination of cracks and compared to the results from $Z^0 \rightarrow \nu\bar{\nu}$ Monte Carlo simulations. The errors displayed represent the statistical

Crack Regions	Fraction of Events	
	Data	$Z^0 \rightarrow \nu\bar{\nu}$ Monte Carlo
90°-90°	0.036 ± 0.025	0.056 ± 0.020
90°-30°	0.143 ± 0.047	0.128 ± 0.023
90°-10°	0.054 ± 0.030	0.039 ± 0.009
30°-30°	0.107 ± 0.042	0.042 ± 0.011
30°-10°	0.089 ± 0.039	0.021 ± 0.007
10°-10°	0.018 ± 0.018	0.004 ± 0.003
90°-30°-10°	0.054 ± 0.030	0.010 ± 0.004
Total fraction in cracks	0.50 ± 0.067	0.283 ± 0.008

Table 5.6: Comparison between data and Monte Carlo of the fraction of events with 3 or more clusters that have 2 or more clusters in crack regions.

uncertainties in the data, and the statistical uncertainties and the uncertainties in the trigger efficiencies in the Monte Carlo. The Monte Carlo results quoted in Table 5.5 were obtained using the MRSB structure functions with $Q^2 = \langle p_t \rangle^2/4$. Other choices of structure functions and Q^2 give similar results. We assume that the $Z^0 \rightarrow \nu\bar{\nu}$ Monte Carlo results also describe the W events in the data set.

Out of the 56 events in the data that have three or more clusters with $E_t > 5$ GeV, 28 events have two or more clusters in crack regions. This represents 50% of the three cluster events, with a statistical uncertainty of $\pm 7\%$. The Monte

Carlo data listed in Table 5.5 show that 28.3% of monojet events with three or more clusters are expected to have two or more clusters in cracks. To estimate the systematic uncertainty on this number, we varied the structure functions, Q^2 value, and simulated energy scale and compared the results. The highest value obtained was 29.3% and the lowest value was 27.7%. Taking one-half of the difference between these values as an estimate of the systematic error gives a total uncertainty of $\pm 0.8\%$.

If $50 \pm 7\%$ of the multicluster events in the data have two or more clusters in cracks, and Monte Carlo results show that only $28.3 \pm 0.8\%$ of multicluster monojet events are expected to have clusters in cracks, then the data probably contains multijet background. We can estimate how many of the 28 multicluster events with clusters in cracks are actually QCD background events. The calculation proceeds in the following manner. Let T represent the number of QCD background events in the data with two or more jets in crack regions. Let n denote the number of multicluster events in the data with two or more clusters in crack regions and F_{crack} represent the fraction of non-multijet events expected to have two or more clusters in cracks. If the total number of multicluster events in the data is 56, then we can write

$$n = F_{crack}(56 - T) + T.$$

It follows that

$$T = \frac{n - 56F_{crack}}{1 - F_{crack}}.$$

Therefore, we can estimate the multijet background in our sample if we know the value of F_{crack}.

Although Monte Carlo studies indicate that $F_{crack} = 0.283 \pm 0.008$ for W and Z events, the data also contain other types of events – mainly dijets, direct photons, and isolated neutral hadrons. We can ignore the small contributions from cosmic ray and beam gas backgrounds. From the unbalanced dijet sample we find that $F_{crack} = 0.238 \pm 0.049$ for dijet background. To estimate F_{crack} for the direct photon/isolated neutral hadron background events, we studied a sample of events that came in on the same Level 2 jet triggers as the dijets, but contained a cluster with EM fraction greater than 0.85. We required these events to pass the monojet cuts after this cluster was removed. To exclude $W \rightarrow e\nu$ events from this sample, we also required the events to have $\sigma_{\mathrm{MET}} < 2.0$ GeV$^{\frac{1}{2}}$. We found about 2300 such events that contained three or more clusters with $E_t > 5$ GeV. From this sample, we estimate that $F_{crack} = 0.243 \pm 0.008$ for the photon/neutral hadron background.

The true value of F_{crack} for the non-multijet events in the data is some weighted average of the values of F_{crack} for the various types of events. However, we do not know the exact proportions of the different types of events in the monojet sample. But the uncertainty in our estimate for the multijet background is dominated by the statistical uncertainty in the number of events with clusters in cracks (taken to be the $\sqrt{n}$), and the precise value of F_{crack} is not important. If we assume that the non-multijet events in the sample consist entirely of vector

boson decays so that $F_{crack} = 0.283$, then our expression for T gives

$$T = 16.9 \pm 7.4 \text{ events.}$$

If, however, we assume that all the non-multijet events in the sample are dijets with $F_{crack} = 0.238$, then we arrive at

$$T = 19.3 \pm 6.9 \text{ events.}$$

The difference between these two estimates is not large compared to the statistical uncertainty. Reasonable assumptions for the relative proportions of vector boson decays, dijet events, and direct photon/neutral hadron background events in the monojet sample give estimates for T around 18 ± 7 events.

Our last category of multijet background events includes events that have completely lost two or more jets. As in the case of multijet events with one jet lost, we have no way of detecting such events. But the probability for a multijet event to lose two or more jets is extremely small. We have shown that the data set contains about 30 dijet events. The total dijet cross section is around a few hundred nanobarns. Therefore, in 4.7 pb^{-1} of integrated luminosity one would expect to produce on the order of 10^6 dijet events. This implies that the probability for one jet in an event to disappear completely is on the order of 10^{-5}. We conclude that the probability for two or more jets in a multijet event to be completely undetected is vanishingly small.

5.3 Summary of QCD Backgrounds

We have shown that there are cracks in the CDF detector and we have defined their locations. We used information from the tracking detectors to estimate the residual dijet background. We estimate that 31 ± 11 dijet events remain in the final data set. The expected $\not{E}_t$ spectrum for these events is shown in Figure 5.6.

From studying the frequency for finding events in the data with two or more energy clusters near known calorimeter cracks, we have concluded that the data contain 18 ± 7 multijet QCD events with two or more poorly measured jets. In addition, we estimate that the data contain 4 ± 4 multijet events with a single jet lost or mismeasured. The $\not{E}_t$ spectrum of the multijet QCD background is unknown. In the final chapter we cut from the sample events with two or more clusters in crack regions in order to present the estimated $\not{E}_t$ distribution of the signal plus background.

Chapter 6

Backgrounds from Prompt Photons and Neutral Hadrons

The lowest order Feynman diagrams for prompt photon production in parton-parton scattering are shown in Figure 6.1. These subprocesses produce events containing a high-E_t photon back-to-back in azimuth to a hadronic jet.

We have seen how false monojet events can result from the failure of the calorimeters to detect hadrons from jet fragmentation or leptons from vector boson decays. Similarly, the data can also contain events in which photons have been lost in calorimeter cracks and dead regions. Our methods for estimating direct photon and neutral hadron backgrounds are based on studies of both real CDF data and Monte Carlo simulations. We could have chosen to rely solely on Monte Carlo simulations to estimate these backgrounds, but by using real data whenever possible we hope to minimize the systematic errors associated with Monte Carlo analyses.

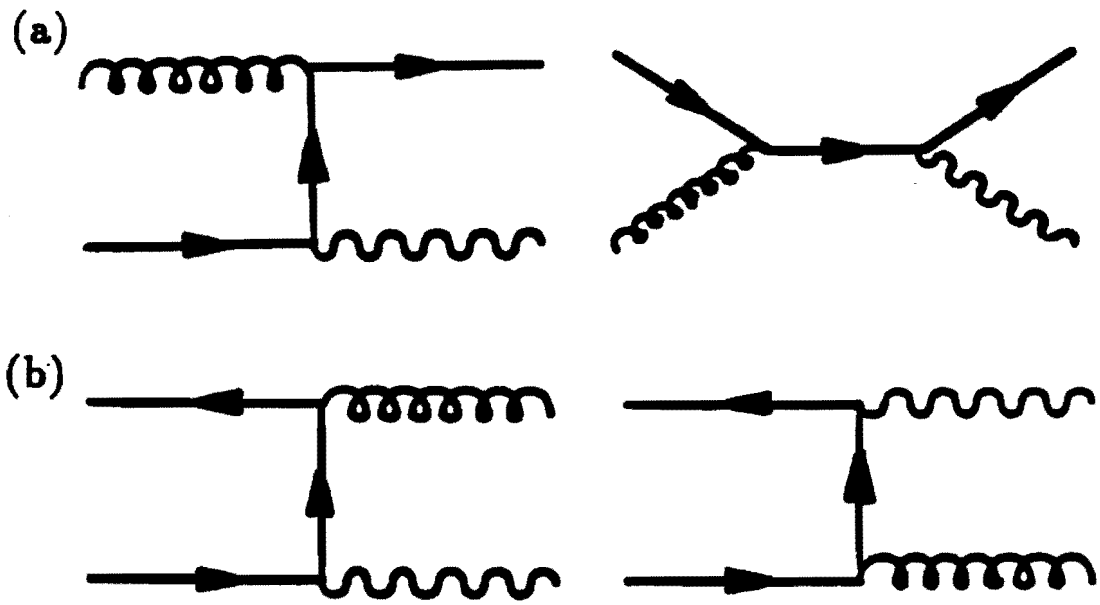

Figure 6.1: The lowest order Feynman diagrams for direct photon production in the parton model. Diagrams (a) show Compton scattering, and diagrams (b) show $q\bar{q}$ annihilation.

The CDF detector is unable to discriminate, on an event by event basis, between EM showers produced by single prompt photons and showers caused by multiple photons from decays of neutral particles such as π^0, η, and K_S mesons. For this reason we group these two sources of background together.

The procedure we used for evaluating direct photon and neutral hadron backgrounds is similar to the technique described in Chapter 4 for using the $W \rightarrow e\nu$ data set to estimate the background from hadronic decays of W taus. We start with a sample of photon candidates from the CDF data. We test each event to see if it would pass our monojet cuts if the photon calorimeter cluster were not present. Events that pass our cuts are added to the background estimate, with a weight determined by the probability for the photon to have been lost in a crack and the trigger efficiency, selection efficiency, and geometric acceptance for photons. The photon loss probabilities were determined from the ISAJET Monte Carlo and detector simulation.

Before we present the specific details of our technique for evaluating direct photon and neutral hadron backgrounds, a brief description of the CDF photon data set is in order. In the following section we describe the procedure used to select the photon candidate events used in this study. The reader who is interested in further information should consult Reference [47].

6.1 The CDF Direct Photon Sample

We base our analysis on a sample of prompt photon candidates collected from 2.55 pb^{-1} of CDF data. These events passed a Level 2 trigger which required that there be a cluster in the central calorimeters with $E_t > 23$ GeV and EM fraction greater than 89%. The trigger also required the photon to be isolated: the extra energy inside an η-φ cone of radius 0.7 centered on the cluster had to be less than 15% of the cluster energy.

The events were further required to satisfy the following criteria:

- There were no CTC tracks associated with the photon cluster. This eliminated clusters produced by charged particles.

- There could be only one CES cluster with $E_t > 1$ GeV within the boundaries of the photon calorimeter cluster. CES strip and wire clusters consist of 11 channels (total width ≈ 0.1 radians) centered on a seed channel with at least 0.5 GeV of energy. A CES chamber with wire and strip clusters is shown schematically in Figure 6.2. This requirement reduced the background from multiple photons produced in neutral hadron decays.

- The CES lateral and transverse shower profiles, when fit to the the average shower profiles observed for testbeam electrons, were required to satisfy $\frac{1}{2}(\chi^2_{r\varphi} + \chi^2_z) < 20$. This cut further reduced the neutral hadron background.

- The centroid of the photon cluster, measured by the CES chambers, had

to be in the CES fiducial volume. The fiducial volume of a CES chamber is defined by

$$14 \text{ cm} < |z| < 217 \text{ cm}$$

and

$$|X| < 17.5 \text{ cm}$$

where X is the distance from the center of the chamber in the r-φ direction. See Figure 6.2. The fiducial cuts were imposed to avoid uninstrumented regions at the edges of the CES chamber. They also avoided the calorimeter 90° crack and φ cracks.

- The photon calorimeter cluster was required to be in the region $|\eta| < 0.9$. This cut reduced energy leakage through the 30° crack.

- The missing E_t significance, σ_{MET}, had to be less than 3.0 $\text{GeV}^{\frac{1}{2}}$. This cut removed photons produced by cosmic ray bremsstrahlung.

About 1.2×10^4 photon candidates survive these cuts. The efficiencies for photons to pass each of these cuts are listed in Table 6.1.

We also need to understand the selection efficiency for isolated neutral hadrons. The two cuts designed to reject neutral hadrons are the cut on the CES χ^2 and the cut on the E_t of the second CES cluster. The combined efficiencies of these cuts for the various decay modes of neutral mesons is shown in Figure 6.3. These data show that a substantial portion of the events with isolated neutral hadrons

Trigger Cuts	γ Efficiency
$E_t > 23$ GeV	≈ 1 for $E_t > 27$ GeV
EM fraction > 0.89	≈ 1
Isolation	$0.82 \rightarrow 0.96$
Event Selection Cuts	
No track pointing at photon	0.965
No second CES cluster with $E_t > 1$ GeV	0.90
$\frac{1}{2}(\chi^2_{r\varphi} + \chi^2_z) < 20$	≈ 1
CES fiducial cuts	0.64

Table 6.1: Efficiencies for the photon trigger and event selection cuts. The efficiency of the isolation cut varies with the transverse energy of the photon.

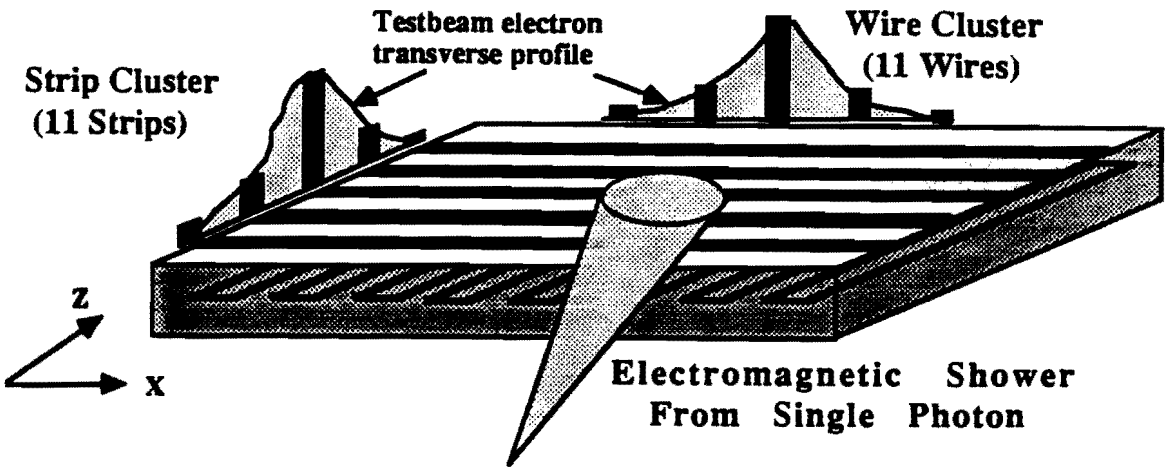

Figure 6.1: Photon strip and wire clusters in a CES chamber.

were not included in the direct photon data set. Is it possible that the rejected neutral hadron events are a potential source of monojet background?

Figure 6.3 shows the CES χ^2 distributions for the photons and the neutral hadron background in the direct photon sample. This plot shows that most neutral hadrons will pass the χ^2 cut. The requirement that there be no second CES cluster with $E_t > 1$ GeV is a much tighter cut, and rejects most of the background. Events will fail these cuts if two photons are separated by at least the angular width of a CES cluster. This corresponds to a spatial separation of about 20 cm at the inner radius of the central calorimeter. This distance is large compared to the size of any of the calorimeter cracks and dead regions.

It is reasonable to assume that the probability for two such widely separated photons to both disappear in cracks is much smaller than the probability for a single photon to be lost. We therefore assume that isolated neutral hadrons that fail the photon selection cuts do not contribute significantly to the monojet backgrounds.

6.2 Calculating the Direct Photon/Neutral Hadron Background

The number of direct photon and neutral hadron events in the data set, N_γ, is given by

$$N_\gamma = \frac{\mathcal{L}_{mon}}{\mathcal{L}_\gamma} \sum_i w_i$$

where the sum is over all photon candidate events that pass the monojet cuts when the photon cluster is removed, $\mathcal{L}_{mon}/\mathcal{L}_\gamma$ is the ratio of the integrated luminosities in the monojet and photon data sets, and w_i is the weight assigned to the ith event. The weight is given by

$$w = \epsilon_{trig}(\not{E}_t') * \frac{1}{\epsilon_\gamma} * P_{lost}(p_t) * (1 + \mathcal{F}(p_t))$$

where p_t is the transverse momentum of the photon measured by the calorimeters and

- $\epsilon_{trig}(\not{E}_t')$ is the efficiency of the $\not{E}_t$ trigger (from the empirical fit of Figure 2.16) evaluated at $\not{E}_t'$, the magnitude of the $\not{E}_t$ that would have been observed if the photon had not been present.

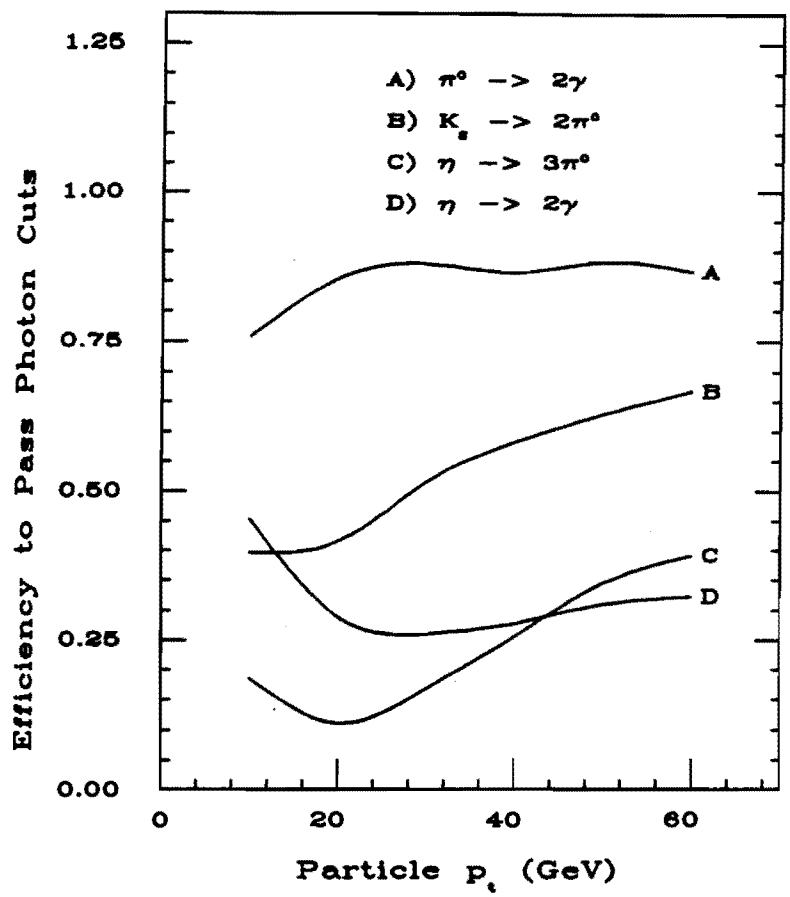

Figure 6.3: The efficiencies for neutral hadrons to pass the photon CES cuts, determined from Monte Carlo studies.

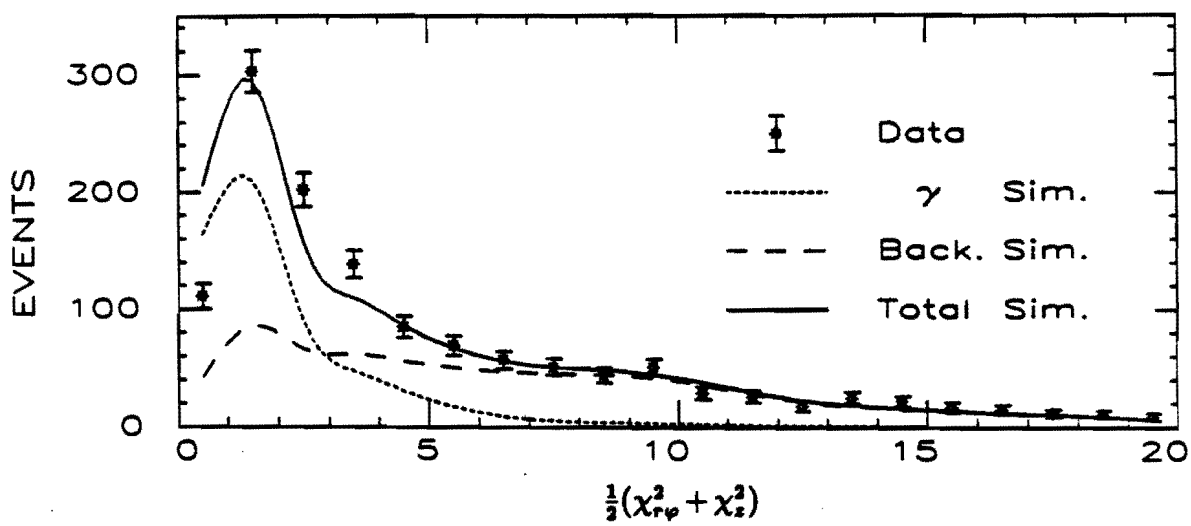

Figure 6.3: The CES χ^2 distributions for photons and neutral hadron background, from Monte Carlo and the data.

- ϵ_γ is the product of all the photon trigger and selection efficiencies in Table 6.1 except the isolation cut efficiency.

- $P_{lost}(p_t)$ is the probability for a photon with transverse momentum p_t to be lost in a calorimeter crack or dead region.

- $\mathcal{F}(p_t)$ is the fraction of direct photon and neutral hadron background events, as a function of photon candidate p_t, that have a photon cluster outside of the region $|\eta| < 0.9$.

We do not include the isolation cut efficiency in calculating the weight because photon candidates that fail this cut are not expected to appear in the monojet background. In an event with a single high-E_t jet and a photon, the jet will tend to be opposite in φ from the photon. If the photon is not detected, then in order for the event to pass the monojet cuts the photon p_t must be at least 30 GeV. The dijet cut on back-to-back clusters is 5 GeV; the trigger isolation cut is 15% of the photon p_t. 15% of 30 GeV is 4.5 GeV, only slightly less than the dijet cut threshold. Therefore, essentially all photon events that fail the isolation cut would also fail the dijet cut if the photon cluster were not detected.

The probability for a photon to escape detection, P_{lost}, was determined from the ISAJET Monte Carlo and the CDF detector simulation package. ISAJET was used to generate direct photon events, and the transverse momenta of the photons was plotted on a histogram. The fraction of the photons in each p_t bin that did not produce a calorimeter cluster or produced a cluster with $E_t < 5$

GeV was identified as the probability for photons in that bin to be lost. These data are displayed in Figure 6.5. We used an empirical fit to the data to estimate the photon loss probability for a given photon p_t. The fit is an exponential for $p_t < 58$ GeV and a constant for higher values of p_t.

The fraction of direct photon and neutral hadron background events with the photon candidate outside of the region $|\eta| < 0.9$, $\mathcal{F}$, was determined from CDF data. From a sample of events that were collected with jet triggers, we selected events that satisfied the following criteria:

- The event had to contain a calorimeter cluster with EM fraction > 0.85.
- The event was required to have $\not{E}_t < 15$ GeV. This excluded $W \rightarrow e\nu$ events from our sample.
- The event had to pass the monojet cuts when the cluster with EM fraction > 0.85 was removed.

The transverse energy of the calorimeter cluster with EM fraction > 0.85 (taken to be the photon candidate) was plotted on a histogram. For each E_t bin we calculated the fraction of events with the photon candidate in the region $|\eta| > 0.9$. These data are shown in Figure 6.6 along with the linear fit used to estimate $\mathcal{F}$.

From the entire direct photon sample, we find 540 events that pass the monojet cuts after the photon candidate is removed. Our background calculation then gives:

$$N_\gamma = 31.0 \pm 1.47 \text{ (sys.)} \pm 1.14 \text{ (stat.)} \text{ events.}$$

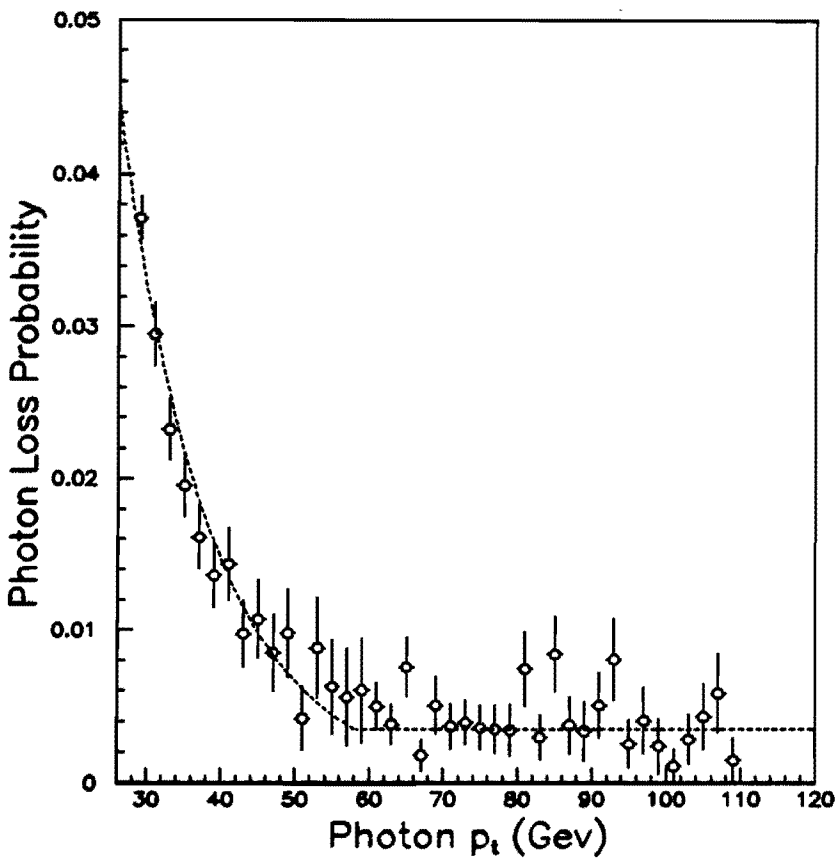

Figure 6.5: The probability for a photon to escape detection determined from Monte Carlo studies. The error bars represent statistical uncertainties. Also shown is the empirical fit used in the direct photon background calculation.

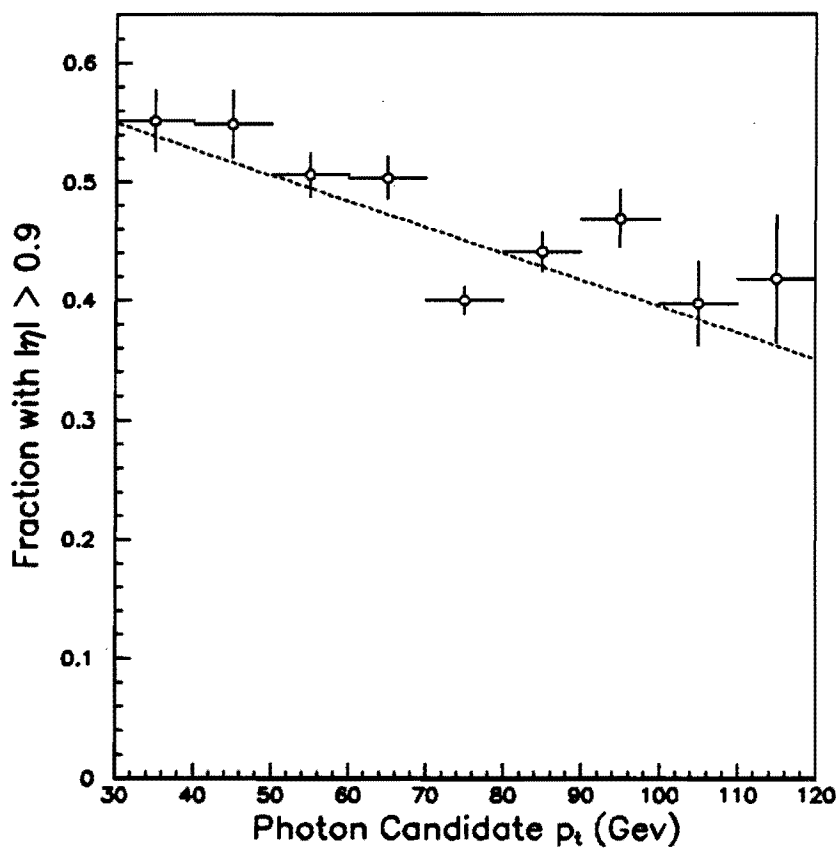

Figure 6.6: Fraction of prompt photon and neutral hadron background events with the photon candidate in the region $|\eta| > 0.9$. The error bars represent statistical uncertainties. Also shown is the empirical fit used in the direct photon background calculation.

The $\not{E}_t$ spectrum of the expected direct photon and neutral hadron background is shown in Figure 6.7. The error bars in this plot reflect the the uncertainties in the $\not{E}_t$ trigger efficiency, the photon loss probability, the fraction of events with photons outside of $|\eta| < 0.9$, and the statisical uncertainities.

We have now presented background estimates for all the sources of background listed in Section 3.1. In the following chapter we will extract the $Z^0 \rightarrow \nu\bar{\nu}$ signal from the data set and demonstrate that the observed signal is consistent with the Standard Model.

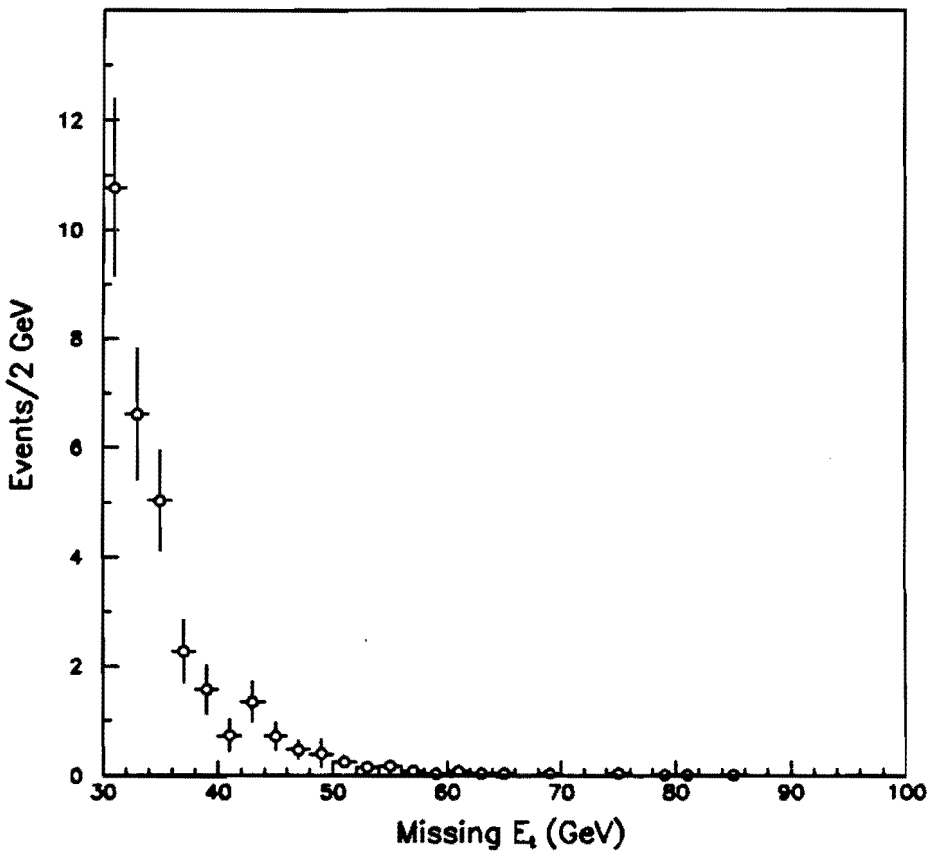

Figure 6.7: The expected $\not{E}_t$ spectrum of the prompt photon and isolated neutral hadron background.

Chapter 7

Conclusions

In Table 7.1 we summarize the results of the background calculations presented in the preceeding chapters. Subtracting the sum of the background estimates from the number of events in the monojet sample yields a $Z^0 \rightarrow \nu\bar{\nu}$ signal of 49 ± 23 events. This is consistent with the Monte Carlo prediction of 78 ± 15 events.

In the following section we compare the observed number of $Z^0 \rightarrow \nu\bar{\nu}$ events to the number of $Z^0 \rightarrow e^+e^-$ events also found in the CDF data. We also present the $\not{E}_t$ spectrum of sum of the estimated components of the monojet sample and compare it to the spectrum observed in the data.

7.1 Comparison to $Z^0 \rightarrow e^+e^-$

The decay of the Z^0 is specified in the Standard Model [56] in terms of the Fermi coupling constant G_F, that mass of the Z^0, and the Weinberg angle θ_W

Process	Estimated Number of Events
$p\bar{p} \rightarrow W^{\pm} + \text{jet};\ W^{\pm} \rightarrow \ell^{\pm}\nu_{\ell}$	57 ± 11
$p\bar{p} \rightarrow W^{\pm};\ W^{\pm} \rightarrow \tau^{\pm}\nu_{\tau};\ \tau \rightarrow \text{hadrons}$	26 ± 5
$p\bar{p} \rightarrow Z^{0} + \text{jet};\ Z^{0} \rightarrow \ell^{+}\ell^{-}$	1 ± 0.2
QCD dijets	31 ± 11
Multijet events with one jet lost or mismeasured	4 ± 4
Multijet events with ≥ 2 jets lost or mismeasured	18 ± 7
Prompt photons and isolated neutral hadrons	31 ± 2
Cosmic rays and beam gas	9 ± 4
Total Background Estimate:	177 ± 18
Number of events in the final sample:	226
Extracted $Z^{0} \rightarrow \nu\bar{\nu}$ Signal:	49 ± 23

Table 7.1: The estimated contribution to the monojet sample from each source of background, and the estimated number of invisible Z^0 decays in the monojet sample.

which is a free parameter of the theory. For each neutrino family the partial width is given by

$$\Gamma(Z^0 \rightarrow \nu_\ell \bar{\nu}_\ell) = \frac{G_F m_z^3}{12\sqrt{2}\pi} = 0.165$$

and for each species of charged lepton the partial width is

$$\Gamma(Z^0 \rightarrow \ell^+\ell^-) = \Gamma(Z^0 \rightarrow \nu_\ell \bar{\nu}_\ell) \times (1 - 4sin^2\theta_W + 8sin^4\theta_W).$$

This thesis reports on a measurement of the ratio

$$\frac{N_\nu \Gamma(Z^0 \rightarrow \nu_\ell \bar{\nu}_\ell)}{\Gamma(Z^0 \rightarrow e^+e^-)} = \frac{N_\nu}{1 - 4sin^2\theta_W + 8sin^4\theta_W} \tag{7.1}$$

For $sin^2\theta_W = 0.23$ and $N_\nu = 3$, this gives:

$$\frac{N_\nu \Gamma(Z^0 \rightarrow \nu_\ell \bar{\nu}_\ell)}{\Gamma(Z^0 \rightarrow e^+e^-)} = \frac{Br(Z^0 \rightarrow \nu\bar{\nu})}{Br(Z^0 \rightarrow e^+e^-)} = 5.962$$

We can therefore check to see if the size of the observed $Z^0 \rightarrow \nu\bar{\nu}$ signal is consistent with theoretical expectations by comparing it to the number of $Z^0 \rightarrow e^+e^-$ events found in the CDF data. The same result could also be achieved by comparing the monojet signal to the number of $Z^0 \rightarrow \mu^+\mu^-$ events, but the $Z^0 \rightarrow \mu^+\mu^-$ data set from the CDF 1988-89 run is too small to be useful for this purpose.

A brief description of the selection process for $Z^0 \rightarrow e^+e^-$ events is given below. Further details can be found in Reference [48].

7.1.1 The CDF $Z^0 \rightarrow e^+e^-$ Sample

The $Z^0 \rightarrow e^+e^-$ candidate events were collected from 4.05 pb^{-1} of CDF data. These events passed a Level 2 trigger which required that there be a cluster in

the central calorimeters with $E_t > 12$ GeV and EM fraction greater than 87.5%. The trigger also required that there be a CTC track with $p_t > 6$ GeV associated with the cluster.

The events were further required to have an electron candidate in the central region that satisfied the following criteria:

- $E_t > 20$ GeV.
- $E_t/p_t < 1.5$. p_t is the transverse momentum of the CTC track associated with the cluster.
- LSHR < 0.2. This quantity is defined in Section 3.5.
- $\Delta z < 3$ cm and $\Delta(r\varphi) < 1.5$ cm. Δz and $\Delta(r\varphi)$ are the distances between the extrapolated track and the shower position measured by the CES chamber.
- $\chi^2_z < 15$. This quantity is defined in Section 3.5.
- The fraction of the cluster's energy in the hadronic calorimeters could not exceed $0.055 + 0.00045E$, where E is the cluster energy in GeV.
- The E_t deposited in a η-φ cone of radius 0.4 centered on the cluster minus the E_t of the cluster could not exceed 10% of the energy in the cone. This required the electron to be isolated.

The event was also required to have a vertex z position within 60 cm of the center of the detector, and to have a second electron candidate such that the invariant mass of the two electrons was between 75 and 105 GeV. The second electron had to pass the following cuts:

- If the electron was in the central region, it was required to have $E_t/p_t < 2.0$.
- If the electron was in the gas calorimeters, than it had to satisfy the following criteria:
  - At least half of the VTPC wire channels along a road between the event vertex and the calorimeter cluster had to record hits.
  - The shower shape requirement for plug electrons was $\chi^2_{3\times3} < 20$. For forward electrons, the requirement was $E_{front}/E_{total} > 0.6$.
- EM fraction > 0.90.
- The E_t deposited in a η-φ cone of radius 0.4 centered on the cluster minus the E_t of the cluster could not exceed 10% of the energy in the cone.

The electron candidates were also required to be in the fiducial regions of the calorimeters, away from known cracks and dead regions. A total of 235 events passed these cuts.

The selection efficiencies for $Z^0 \rightarrow e^+e^-$ events were found to be independent of the Z^0 transverse momentum. The selection and trigger efficiencies are listed in Table 7.2.

Electron Regions	Trigger Efficiency	Selection Efficiency
central-central	≈ 1	0.79 ± 0.06
central-plug	0.97 ± 0.04	0.79 ± 0.06
central-forward	0.97 ± 0.04	0.83 ± 0.05

Table 7.2: Trigger and event selection efficiencies for $Z^0 \rightarrow e^+e^-$ events with the first electron in the central region and the second electron in the central, plug, or forward.

7.1.2 The Ratio $Br(Z^0 \rightarrow \nu\bar{\nu})/Br(Z^0 \rightarrow e^+e^-)$

We compare the observed number of true monojet events to the number of $Z^0 \rightarrow e^+e^-$ events that contain a single high-E_t hadronic jet. We do this by taking the ratio of the number of monojets to the number of $Z^0 \rightarrow e^+e^-$ events that pass the monojet cuts after the electrons are removed. In this way identical cuts are performed on both data sets and the monojet selection efficiencies cancel. However, the integrated luminosities, trigger efficiencies, and fiducial acceptances for the two data sets are not equal, and their ratios must be taken into account. We must also consider the selection efficiencies for the $Z^0 \rightarrow e^+e^-$ cuts.

The acceptance for both electrons from a Z^0 decay to be in the fiducial regions of the calorimeters was studied from Monte Carlo simulations, and found to vary linearly with the p_t of the Z^0. For $Z^0 \rightarrow \nu\bar{\nu}$ events, the neutrinos are not observed and can be anywhere. The geometrical acceptance for the neutrinos is therefore

equal to 1.

The ratio of the $\nu\bar{\nu}$ branching fraction to the e^+e^- branching fraction for the Z^0 is therefore given by:

$$\frac{Br(Z^0 \rightarrow \nu\bar{\nu})}{Br(Z^0 \rightarrow e^+e^-)} = \frac{49}{\frac{\mathcal{L}_{mon}}{\mathcal{L}_{ee}} * f_{DY} * \sum\{\epsilon_{trig}^{(i)}/(\epsilon_{ee}^{(i)} * a_i)\}}$$

where 49 is the observed $Z^0 \rightarrow \nu\bar{\nu}$ signal, $\mathcal{L}_{mon}/\mathcal{L}_{ee}$ is the ratio of the integrated luminosities of the monojet and $Z^0 \rightarrow e^+e^-$ samples, and f_{DY} is the correction for the fraction of Z^0 candidates that come from the Drell-Yan continuum ($f_{DY} = 0.987 \pm 0.005$). The sum is over the $Z^0 \rightarrow e^+e^-$ events that pass the monojet cuts after the electrons are removed. The missing E_t trigger efficiency for the ith event, corresponding to the magnitude of the $\not{E}_t$ that would have been observed if the electrons had not been present, is denoted by $\epsilon_{trig}^{(i)}$. The product of the electron trigger and selection efficiencies for the ith event is $\epsilon_{ee}^{(i)}$. The fiducial acceptance for the electrons, corresponding to the Z^0 p_t of the ith event, is represented by a_i.

We find 4 events in the $Z^0 \rightarrow e^+e^-$ sample that would pass the monojet cuts if the electrons were not present. The characteristics of these events are displayed in Table 7.3. Our result is therefore

$$\frac{Br(Z^0 \rightarrow \nu\bar{\nu})}{Br(Z^0 \rightarrow e^+e^-)} = 4.4 \pm 3.0$$

This is in agreement with the Standard Model and three species of light neutrinos.

Another way to express the above result is to use Equation 7.1 to calculate

Electron Regions	E_t' (GeV)	ϵ_{trig}	Fiducial Acceptance
Central-central	33.7	0.877	0.460
Central-central	39.7	0.890	0.440
Central-central	48.4	0.901	0.465
Central-forward	37.2	0.887	0.437

Table 7.3: Characteristics of the four $Z^0 \rightarrow e^+e^-$ events that pass the monojet cuts after the electrons are removed. E_t' is the missing E_t that would have been observed if the electrons had not been detected.

N_ν, the number of light neutrino species. This gives

$$N_\nu = 2.2 \pm 1.5.$$

Using the results from Table C.1 in Appendix C, we calculate an upper limit on N_ν:

$$N_\nu < 5 \ \ (90\% \text{ C.L.}).$$

For comparison, measurements of N_ν from other recent high energy physics experiments are presented in Table 7.4.

7.2 The Monojet Missing E_t Spectrum

In Figure 7.1 we display the estimated missing E_t spectrum of the sum of the $Z^0 \rightarrow \nu\bar{\nu}$ signal and all the sources of monojet background described in the

Experiment	Number of Neutrino Species
UA1 (1987)	< 10 (90% C.L.)
MARK II (1989)	2.8 ± 0.6
L3 (1989)	3.42 ± 0.48
OPAL (1989)	3.1 ± 0.4
DELPHI (1989)	2.4 ± 0.6
ALEPH (1990)	3.01 ± 0.16
L3 (1992)	3.24 ± 0.51
This analysis	2.2 ± 1.5

Table 7.4: Measurements of N_ν from various $p\bar{p}$ and e^+e^- collider experiments. The values from UA1, L3 (1992) and this analysis are from direct observation of the invisible decays of the Z^0; the other values were obtained from measurements of the decay width of the Z^0.

preceeding chapters. Since we do not have knowledge of the $\not{E}_t$ spectrum of the multijet QCD background, the data of Figure 7.1 do not include the 28 events that have three or more energy clusters with $E_t > 5$ GeV and two or more clusters in crack regions. However, we did not apply these cuts to the estimated backgrounds from QCD dijets and hadronic decays of W taus. Removing events with two or more clusters in cracks reduces these backgrounds by only a few per cent, and this change is small compared to the statistical uncertainties in the background estimates. We also neglected the small contributions to the monojet sample from multijet QCD events with one jet lost or mismeasured (estimated to be 4 ± 4 events), and from cosmic ray/beam gas backgrounds (9 ± 4 events).

The data set contains 198 events after the events with two or more clusters in cracks are removed. The sum of the signal plus background estimates give a sample size of 217 ± 15 events. Figure 7.1 shows that there is good agreement between the data and the calculations not only in the number of events but also in the shape of the $\not{E}_t$ distribution.

7.3 Limits on New Physics

Although the data reveal no evidence for the existence of hitherto unknown processes that produce monojets, we can set an upper limit on the possible cross section for such processes. We can derive from our results an upper limit on the cross section for monojet production. The difference between this cross section

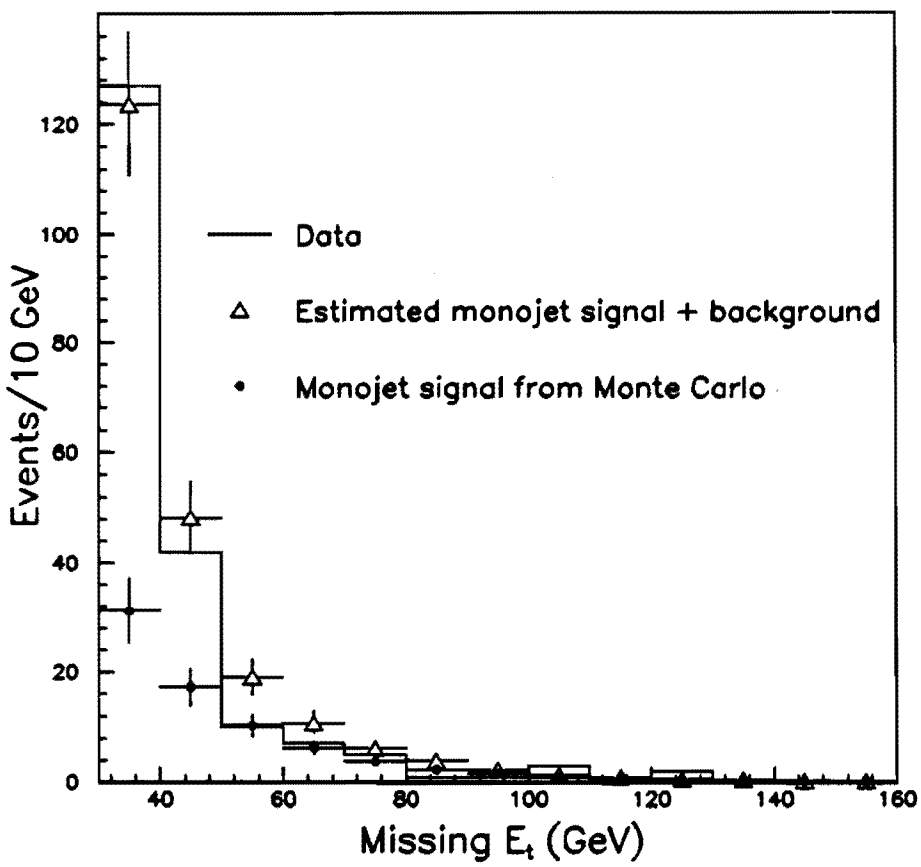

Figure 7.1: The $\not{E}_t$ distributions of: the $Z^0 \rightarrow \nu\bar{\nu}$ signal estimated from Monte Carlo (dots), the sum of all estimated components of the monojet sample (triangles), and the final monojet data set (histogram). Events with three or more energy clusters that have two or more clusters in cracks have been excluded.

and the known cross section for $p\bar{p} \rightarrow Z^0 + \text{jet}$; $Z^0 \rightarrow \nu\bar{\nu}$ is the limit for possible new physics.

We use the mathematical technique described in Appendix C to calculate the upper limit on the number of real monojets in the data set at the 95% confidence level. From this upper limit and our knowledge of trigger and selection efficiencies, we can calculate an upper limit on the cross section for processes that produce events with a single high-E_t jet ($E_t > 15$ GeV) with the jet in the central region ($|\eta| < 1.2$) and missing E_t greater than 30 GeV. For a final data sample of 226 events, of which 177 ± 18 are estimated to be background, we find that the upper limit s on the observed signal at the 95% confidence level is $s = 110$ events. The corresponding cross section is given by

$$\sigma_{mon} = \frac{s}{\mathcal{L}_{mon} * \epsilon_{trig} * \epsilon_{zvert} * \epsilon_{cuts}}$$

where

$\mathcal{L}_{mon}$ = Integrated luminosity of the monojet sample.

ϵ_{trig} = Average efficiency of the Missing E_t trigger for events with $\not{E}_t > 30$ GeV.

ϵ_{zvert} = Efficiency of the vertex z position cut ($|z_{vert}| < 60$ cm.)

ϵ_{cuts} = Efficiency of the monojet selection cuts for events with a single high-E_t jet, the jet in the central region, and $\not{E}_t > 30$ GeV (determined from Monte Carlo).

The numerical values of ϵ_{trig}, ϵ_{zvert}, and ϵ_{cuts} are 0.890, 0.948, and 0.823 respectively. This gives an upper limit on the monojet cross section

$$\sigma_{mon} < 33.5 \text{ pb}$$

at the 95% confidence level. The PAPAGENO event generator (using the MRSB structure functions) gives the cross section for the process $Z^0 \rightarrow \nu\bar{\nu}$:

$$\sigma_{Z^0 \rightarrow \nu\bar{\nu}} = 25.2 \text{ pb}$$

Hence, our upper limit for the cross section for new physics is

$$\sigma_{new} < 8.3 \text{ pb} \ \ (95\% \text{ C.L.}).$$

7.4 Possible Improvements to this Study

At the time of this writing, the CDF Collaboration is collecting $p\bar{p}$ data with an upgraded detector [57]. The Tevatron has also been improved, and luminosities around 5×10^{30} cm^{-2}s^{-1} or higher are expected to be achieved soon. For the benefit of those who might tread this path again, we present the following suggestions for improving this study.

The single most important change that would benefit a similar analysis of monojet data would be an increase in the integrated luminosity of the data sample. Throughout this analysis, the precision of our results has been limited by statistical errors. This is particularly true for the QCD dijet background calculations. A larger CDF data set would not only lead to a better understanding

of the monojet data, it would presumably also bring a corresponding increase in the number of $Z^0 \rightarrow e^+e^-$ events. This would give a better measurement of the ratio of the $\nu\bar{\nu}$ branching fraction to the e^+e^- branching fraction.

The most problematic part of this analysis, and also the largest source of error, was understanding the QCD backgrounds. The QCD background studies would benefit not only from an increase in overall size of the data set but also from changes in the choice of triggers used in collecting QCD data. In the 1988-89 run, three Level 2 triggers were used to collect most of the QCD data. Each trigger required a single jet with E_t above a certain threshold. The thresholds used were 20, 40, and 60 GeV. The first two triggers were prescaled by factors of 300 and 30 respectively. Most of the data came in on the 60 GeV trigger. However, due to the larger cross section at low E_t, most of the monojet QCD backgrounds are from events with jet transverse energies below 40 GeV. An increase in the amount of low E_t QCD data collected would be helpful in studying the QCD backgrounds. The relative paucity of low E_t data from the 1988-89 run is one of the reasons why the relative errors for the low $\not{E}_t$ bins in the histogram of Figure 5.6 are so much larger than the errors for the high $\not{E}_t$ bins.

The changes that have been made to the CDF detector for the current run include the installation of an improved vertex tracking chamber (VTX), a silicon microstrip detector (SVX), and an expanded muon system. These existing hardware upgrades, and the proposed future upgrades discussed below, afford opportunities to do a better analysis of the monojet data.

The VTX uses octagonal proportional chambers similar to those used in the VTPC, but the drift distance has been reduced from 15 cm to 4 cm and the pads have been removed. The VTX consists of 28 such modules. As in the case of the VTPC, adjacent modules are rotated by 11.3° to allow a stereo view of tracks. The VTX efficiencies and resolutions should be superior to those of the VTPC. Better tracking at small angles would improve the efficacy of the track clustering technique used in this study to analyze the QCD backgrounds.

The SVX consists of two 25 cm long modules on either side of the interaction point. Each module contains four layers of silicon microstrip detectors at radii between 3 and 8 cm from the beam axis. The SVX precisely measures the positions of secondary vertices, with an impact parameter resolution around 20 μm for high momentum tracks. A τ lepton from a W decay travels about 2 mm in the lab frame. It should therefore be possible to directly observe τ decay vertices. This would improve the rejection of monojet τ background.

The addition of new scintillators and drift chambers has extended the muon coverage of the CDF detector to $|\eta| = 1.0$. Although $W \rightarrow \mu\nu$ events are a major source of monojet background, muon background in the central region is already well identified by the CTC and the effect of the muon upgrade on a monojet analysis would be small.

In the future, the plug and forward gas calorimeters are expected to be replaced by a single calorimeter system that will fit into the space occupied by the existing endplugs. The new plug calorimeters will use scintillating plastic

tiles and optical fiber readout. They will have improved hermeticity and energy resolution, and this will result in a more accurate measurement of missing E_t. When the new endplugs are installed, the forward muon toroids will be moved 5 m closer to the central detector. The forward muon chamber/scintillator systems will be upgraded, and CDF will then have the capability to identify muons out to $|\eta| = 2.8$. Muon backgrounds in the monojet sample can then be greatly reduced.

Appendix A

Corrections to the Missing E_t Measurement

The raw missing E_t for a monojet event, obtained by vectorially summing the energy measured in each calorimeter tower, is only a rough measure of the true transverse momentum imbalance. Mismeasurement of the $\not{E}_t$ is caused by nonlinear calorimeter response and energy leakage through cracks. We describe here the method used for correcting the observed $\not{E}_t$ to account for these effects. This technique was originally developed to correct the $\not{E}_t$ in W boson events [49]. We use it without modification, except that corrections to the E_t of W electrons are not necessary.

For the purposes of this calculation, we divide the energy measured by the detector into two parts: the clustered energy (jets), and the unclustered energy (UCE). The ith component of the raw unclustered energy vector is defined by:

$$\mathrm{UCE}_i = -(\sum_{p_t > 10\,\mathrm{GeV}} p_i + \not{E}_t^{(i)}), \quad i = 1,2$$

where $\not{E}_t^{(i)}$ is the ith component of the raw missing E_t, and $\sum p_i$ is the sum of the ith momentum component of each jet. The sum is over all energy clusters with p_t above a threshold cut. Clusters below this cut are included in the unclustered energy. The momentum vector of a cluster differs from the energy vector used elsewhere in this analysis by only a small correction for the finite mass of the jet.

Corrections are applied separately to the energy of each cluster and to the unclustered energy. The corrected missing E_t for the event, $\not{E}_t^{(corr)}$, is then obtained from the corrected energies by inverting the above relation:

$$\not{E}_t^{(i,corr)} = -(\mathrm{UCE}_i^{(corr)} + \sum_{\mathrm{clusters}} p_i^{(corr)}), \quad i = 1,2$$

The procedures used to correct each piece of the missing E_t are outlined below.

A.1 Clustered Energy Corrections

The energy of a cluster is first multiplied by a correction factor, determined by its η coordinate, to give the energy that would have been measured had the jet been in the central calorimeter. Another correction factor is then applied to give the true energy for a central jet with this observed energy. Knowledge of the relative calorimeter response as a function of η is obtained using the method of dijet balancing. In this technique, QCD dijet events are selected that have at

least one jet in the central region that is not close to the 10° and 30° η cracks. The central jet is called the "trigger" jet, and the other jet (which can be anywhere in the detector) is the "probe" jet. The ratio of the transverse energies of the probe jet to the trigger jet gives a correction factor for the energy measurement relative to the central calorimeters.

The absolute correction factor for jets in the central region was determined from Monte Carlo studies. This factor represents the ratio of the total momentum of all the particles incident on the calorimeter within the clustering cone to the observed cluster energy.

A.2 Unclustered Energy Corrections

The correction factor for the unclustered energy was determined from studying Monte Carlo simulations of W events. The true energy of all the particles outside of the jets in a W or Z event was found to be a factor of 2 greater than the measured energy. This factor includes not only a correction for calorimeter mismeasurement, but also a correction for low-p_t particles which spiral in the magnetic field and never reach the calorimeters.

A.3 Systematic Errors

A good test of the accuracy of this technique is to apply it to a sample of $Z^0 \rightarrow e^+e^-$ events in which the Z^0 recoils off a jet. For these events, the missing

E_t should be zero and the momenta of the electrons is well measured by the CTC. However, the CDF $Z^0 \rightarrow e^+e^-$ sample is relatively small, and improved statistics can be obtained by also looking at direct photon events in which the photon recoils off a jet and converts into an e^+e^- pair. Studies based on these data samples have determined that the systematic error σ on the corrected energy of a cluster is given by:

$$\sigma = \sqrt{(0.020 * p_t)^2 + 2.25}\ \text{GeV}$$

for clusters with $p_t < 57$ GeV. The systematic error for clusters with $p_t > 57$ GeV is given by:

$$\sigma = \sqrt{(0.020 * p_t)^2 + 6.25}\ \text{GeV}$$

The systematic error on the unclustered energy scale factor (2.0) was determined from the Z^0 sample. The two sigma upper and lower bounds for this scale factor were found to be 1.75 and 2.4.

The effect of the $\not{E}_t$ corrections on the final monojet data set is shown in Figure A.1. Also shown in Figure A.1 is the p_t distribution of the Z^0 bosons from Monte Carlo simulations of the expected $Z^0 \rightarrow \nu\bar{\nu}$ signal. Comparison with Figure 3.15 shows that for most events the raw missing E_t is less than the true transverse momentum imbalance.

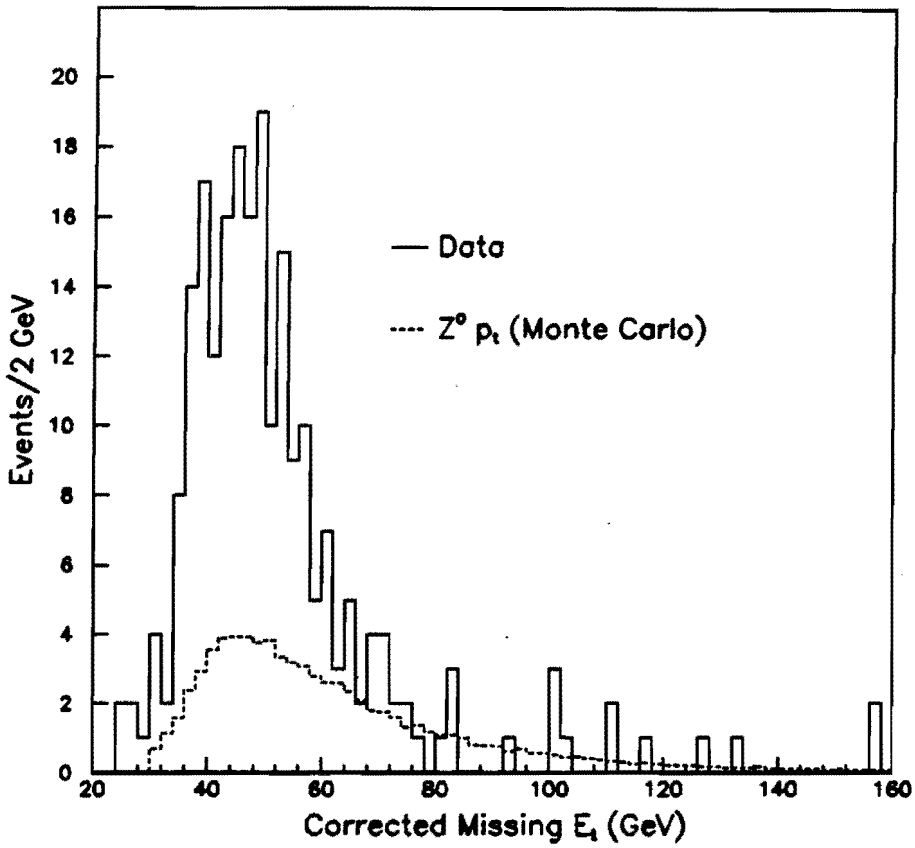

Figure A.1: Corrected $\not{E}_t$ distribution for the 226 events that pass the monojet cuts. Also shown is the estimated Z^0 p_t distribution for the expected monojet signal.

Appendix B

The CDF Detector Simulation Program

The Monte Carlo results quoted in this study were produced using Version 3.21 of the CDF detector simulation program QFL [50], [51]. The QFL program is designed to produce an accurate and reliable simulation of detector behavior, while at the same time being fast and efficient. The speed of the program enables users to process high statistics samples of Monte Carlo events in a reasonable amount of CPU time.

The geometry of the simulated detector is somewhat simplified. The VTPC is not included in the simulation, but the effects of the material of the VTPC on particles that pass through it is taken into account. The calorimeters are modeled as having uniform density, although the tower segmentation is correctly reproduced.

B.1 Calorimeter Simulation

Electromagnetic and hadronic showers are modeled using parameterizations that describe the longitudinal and transverse shower profiles and energy deposition in each sampling layer [52]. These parameterizations have been adjusted to fit test beam data. The assumed resolution of each detector is given by

$$\sigma = \frac{\sigma_0}{\sqrt{E}} + 0.01$$

where the additional 1% is to account for calibration error. The values of σ_0 for each detector are discussed in Section 2.2.2.

The tuning of the energy scale in QFL is based on test beam data and studies done on a sample of single isolated tracks [53]. The systematic error on the QFL energy scale is estimated to be 5% for $E < 5$ GeV, 3% for 5 GeV $< E <$ 15 GeV, and 4% for $E > 15$ GeV.

The central EM calorimeter uses two phototubes per tower, and this is modeled in QFL. When dividing deposited energy between the two tubes, the simulation code includes the exponential attenuation of the signal in the optical media. This is necessary to correctly reproduce the response of the tower to multiple hits.

Particular attention has been paid to accurately modeling the calorimeter cracks in the CDF detector. For the central region, energy leakage between the 15° segments in φ (the φ cracks) and through the crack between the two arches (the 90° crack) is modeled by applying a correction factor on the energy

deposition based on the particle's impact point on the face of the tower. The η cracks between the endwall and the plug (the 30° crack) and between the plug and the forward (the 10° crack) are simulated by incorporating the uninstrumented regions in the QFL geometry. In addition, underinstrumented areas in the plug hadron calorimeter are accounted for by applying an η and φ dependent correction factor.

The overall accuracy of the calorimeter simulation has been studied by comparing it to dijet events and direct photon events where the photon was converted [54]. The agreement between the Monte Carlo and real data is good.

B.2 Tracking Simulation

The simulation of a particle traveling from the event vertex to the calorimeters includes the effects of the passive material that it passes through. The processes modeled include multiple scattering, energy loss, electron bremsstrahlung and γ conversion. For particles that pass through the CTC, simulated tracks are created based on measured CTC efficiencies and resolutions. The tracking simulation has been adjusted to agree with the electron tracks observed in $W \rightarrow e\nu$ events [55]. For particles that reach the muon chambers, simulated track stubs are created based on the measured performance of the chambers.

Appendix C

Calculating the Monojet Signal Upper Limit

We present here an outline of the technique described by G. Zech in Reference [58] for calculating the upper limit on a signal present in a data sample, when given the size of the sample and an estimate of the background.

Consider an experiment for which the expectation value of the observed signal is s and the expectation value for the background is b. Let $P(n_s; s)$ represent the probability for observing n_s signal events, and $P(n_b; b)$ represent the probability for observing n_b background events. The probability $P(n; s+b)$ of observing a total of n events is given by the sum of the products of the probabilities of observing n_s signal and n_b background events for all possible combinations of n_s and n_b that give a total of n:

$$P(n; s+b) = \sum_{n_b=0}^{n} P(n_b; b) P(n - n_b; s).$$

We now assume that the experiment has observed exactly N events. This implies that the number of background events must be no greater than N. We use this knowledge to renormalize $P(n_b; b)$ to the range $n_b \leq N$:

$$P'(n_b; b) = P(n_b; b) / \sum_{n_b=0}^{N} P(n_b; b).$$

The probability for observing n events ($n \leq N$) now becomes:

$$W(n) = P(n; s + b) / \sum_{n_b=0}^{N} P(n_b; b).$$

We wish to calculate the expected signal s for which the probability of observing N events or less is equal to some number α. This value of s corresponds to the upper limit on the observed signal at the $1 - \alpha$ confidence level. It follows that α is given by

$$\alpha = \sum_{n=0}^{N} W(n)$$

which is equivalent to

$$\alpha = \sum_{n=0}^{N} P(n; s + b) / \sum_{n_b=0}^{N} P(n_b; b).$$

In practice, we do not know the true value of b, the expectation value of the background. Instead, we have measured b to be equal to a value b_0 within an uncertainty $\pm\sigma_b$. We will assume that the parent distribution $g(b)$ that the observed values of b are drawn from is a gaussian with mean b_0 and standard deviation σ_b:

$$g(b) = \frac{1}{\sqrt{2\pi}\sigma_b} e^{-\frac{(b-b_0)^2}{2\sigma_b^2}}.$$

Our expression for α now becomes:

$$\alpha = \frac{\sum_{n=0}^{N} \int g(b) P(n; s+b) db}{\sum_{n_b=0}^{N} \int g(b) P(n_b; b) db}. \tag{C.1}$$

We will use Equation C.1 to calculate the upper limit s on the monojet signal at the 95% confidence level ($\alpha = 0.05$).

The probability $P(n_s; s)$ is given by the Poisson distribution:

$$P(n_s; s) = \frac{e^{-s} s^{n_s}}{n_s!}.$$

Similarly, the probability $P(n_b; b)$ is also Poisson distributed:

$$P(n_b; b) = \frac{e^{-b} b^{n_b}}{n_b!}.$$

Substituting the Poisson distributions into Equation C.1 gives

$$\alpha = \frac{\sum_{n=0}^{N} \sum_{n_b=0}^{n} \frac{e^{-s} s^{n-n_b}}{(n-n_b)!} \int_0^\infty g(b) \frac{e^{-b} b^{n_b}}{n_b!} db}{\sum_{n_b=0}^{N} \int_0^\infty g(b) \frac{e^{-b} b^{n_b}}{n_b!} db}. \tag{C.2}$$

The integrals that appear in the numerator and denominator of Equation C.2 are of the form

$$\begin{aligned}
\frac{1}{n_b!} \int_0^\infty g(b) e^{-b} b^{n_b} db &= \frac{1}{\sqrt{2\pi}\sigma_b n_b!} \int_0^\infty e^{-\frac{(b-b_0)^2}{2\sigma_b^2}} e^{-b} b^{n_b} db \\
&= \frac{1}{\sqrt{2\pi}\sigma_b n_b!} \int_0^\infty \exp\{\frac{-(b^2 + b_0^2 - 2bb_0 + 2\sigma_b^2 b)}{2\sigma_b^2}\} b^{n_b} db \\
&= \frac{e^{(b_0 - \sigma_b^2)/2}}{\sqrt{2\pi}\sigma_b n_b!} \int_0^\infty \exp\{\frac{-(b - (b_0 - \sigma_b^2))^2}{2\sigma_b^2}\} b^{n_b} db.
\end{aligned}$$

We make the substitution

$$x = \{\frac{b - (b_0 - \sigma_b^2)}{\sigma_b}\}^2$$

to obtain

$$\frac{1}{n_b!}\int_0^\infty g(b)e^{-b}b^{n_b}db = \frac{e^{(b_0-\sigma_b^2)/2}}{2\sqrt{2\pi}n_b!}\int_{(\frac{\sigma_b^2-b_0}{\sigma_b})^2}^\infty (\sigma_b\sqrt{x}+b_0-\sigma_b^2)^{n_b}\frac{e^{-x/2}}{\sqrt{x}}dx.$$

We use the expansion

$$(\sigma_b\sqrt{x}+b_0-\sigma_b^2)^{n_b} = \sum_{i=0}^{n_b}\frac{n_b!}{i!(n_b-i)!}\sigma_b^i x^{\frac{i}{2}}(b_0-\sigma_b^2)^{n_b-i}$$

to write the integral as

$$\frac{e^{(b_0-\sigma_b^2)/2}}{2\sqrt{2\pi}}\sum_{i=0}^{n_b}\frac{\sigma_b^i(b_0-\sigma_b^2)^{n_b-i}}{i!(n_b-i)!}\int_{(\frac{\sigma_b^2-b_0}{\sigma_b})^2}^\infty x^{(\frac{i-1}{2})}e^{-x/2}dx.$$

Recall the definition of the χ^2 probability distribution for k degrees of freedom:

$$P_{\chi^2}(x;k) = \frac{1}{2\Gamma(k/2)}(\frac{x}{2})^{k/2-1}e^{-x/2}.$$

The integral now becomes

$$\frac{1}{n_b!}\int_0^\infty g(b)e^{-b}b^{n_b}db =$$

$$\frac{e^{(b_0-\sigma_b^2)/2}}{\sqrt{2\pi}}\sum_{i=0}^{n_b}\frac{\sigma_b^i(b_0-\sigma_b^2)^{n_b-i}}{i!(n_b-i)!}2^{\frac{i-1}{2}}\Gamma(\frac{i+1}{2})\int_{(\frac{\sigma_b^2-b_0}{\sigma_b})^2}^\infty P_{\chi^2}(x;i+1)dx. \qquad \text{(C.3)}$$

Substituting Equation C.3 into Equation C.2 gives the exact solution for α in terms of s, N, b_0 and σ_b. However, this solution can be difficult to translate into workable computer code. For large values of N, b_0 and σ_b, it is more practical to solve Equation C.1 using techniques of numerical integration. This task is simplified by making use of the fact that a Poisson distribution with mean μ,

Monojet Signal	1 - Confidence Level
90	0.468
95	0.280
98	0.202
101	0.145
104	0.103
110	0.0495
115	0.0260
120	0.0133

Table C.1: Upper limits on the number of real monojets in the data, and the corresponding values of $\alpha = 1 - CL$.

$P(n;\mu) = e^{-\mu}\mu^n/n!$, for μ greater than about 10 is well approximated by a gaussian distribution with mean μ and standard deviation $\sqrt{\mu}$:

$$P(n;\mu) \approx \frac{1}{\sqrt{2\pi\mu}} e^{\frac{-(n-\mu)^2}{2\mu}}.$$

We evaluated Equation C.1 for $N = 226$, $b_0 = 177$, $\sigma_b = 18$ and various values of s. These results are displayed in Table C.1. The value $s = 110$ events corresponds to $\alpha = 0.05$ or a 95% confidence level.

Bibliography

[1] M. Contreras. *Top Search at CDF*. Fermilab preprint: FERMILAB-Conf-91/294-E. October 1991.

[2] F. Abe *et al.* Phys. Rev. Lett. **62**, 1825 (1989)

[3] P. Hu. *Search for Supersymmetric Particles in $p\bar{p}$ Collisions at $\sqrt{s} = 1.8$ TeV*. PhD Thesis, Rutgers University. June, 1990.

[4] UA1 Collaboration. Phys. Lett. **B 198**, 261 (1987)

[5] UA2 Collaboration. Phys. Lett. **B 235**, 363 (1990)

[6] UA1 Collaboration. Phys. Lett. **B 185**, 241 (1987)

[7] G. S. Abrams *et al.* Phys. Rev. Lett. **63**, 724 (1989)

[8] G. S. Abrams *et al.* Phys. Rev. Lett. **63**, 2173 (1989)

[9] L3 Collaboration. Phys. Lett. **B 231**, 509 (1989)

[10] ALEPH Collaboration. Phys. Lett. **B 231**, 519 (1989)

[11] ALEPH Collaboration. Phys. Lett. **B 235**, 399 (1990)

[12] OPAL Collaboration. Phys. Lett. **B 231**, 531 (1989)

[13] DELPHI Collaboration. Phys. Lett. **B 231**, 539 (1989)

[14] L3 Collaboration. Phys. Lett. **B 275**, 209 (1992)

[15] Decriptions of the Fermilab Tevatron can be found in the following references:

R. Johnson, *Proceedings of the IEEE 1987 Particle Accelerator Conference,* Washington, D.C., 8-12.

P. Martin *et. al.*, *Ibid.* 47-49.

J. D. McCarthy, *Ibid.* 1388-1391.

J. Gannon, *Proceedings of the IEEE 1989 Particle Accelerator Conference,* Chicago, IL, 68-70.

[16] F. Abe *et al.* Nucl. Inst. and Meth. **A 271**, 387 (1988)

[17] F. Snider *et al.* Nucl. Inst. and Meth. **A 268**, 75 (1988)

[18] F. Bedeschi *et al.* Nucl. Inst. and Meth. **A 268**, 50 (1988)

[19] L. Balka *et al.* Nucl. Inst. and Meth. **A 267**, 272 (1988)

[20] L. Nodulman *et al.* Nucl. Inst. and Meth. **176**, 345 (1980)

[21] S. Bertolucci *et al.* Nucl. Inst. and Meth. **A 267**, 301 (1988)

[22] Y. Fukui *et al.* Nucl. Inst. and Meth. **A 267**, 280 (1988)

[23] G. Brandenburg *et al.* Nucl. Inst. and Meth. **A 267**, 257 (1988)

[24] S. Cihangir *et al.* Nucl. Inst. and Meth. **A 267**, 249 (1988)

[25] S. R. Hahn *et al.* Nucl. Inst. and Meth. **A 267**, 351 (1988)

[26] A. Sansoni. Private communication.

[27] S. Errede and W. Trishcuk. *E/P Calibration of the CEM Calorimeter.* CDF Note #1081 (1990)

[28] F. Abe *et al.* Phys. Rev. Lett. **63**, 720 (1989)

[29] G. Ascoli *et al.* Nucl. Inst. and Meth. **A 268**, 33 (1988)

[30] K. Byrum *et al.* Nucl. Inst. and Meth. **A 268**, 46 (1988)

[31] C. Grosso-Pilcher and S. White. *The CDF Luminosity Calibration.* Fermilab preprint: FN-550. October 1990.

[32] D. Amidei *et al.* Nucl. Inst. and Meth. **A 269**, 51 (1988)

[33] J. Proudfoot. *Proceedings of the Workshop on Calorimetry for the Superconducting Supercollider*, Tuscaloosa, AL, 1989. 1-8.

[34] B. Winer. *The W Boson Transverse Momentum Spectrum in Proton-Antiproton Collisions at* $\sqrt{s}$ = 1.8 *TeV.* PhD Thesis, University of California-Berkeley. February, 1991. LBL preprint: LBL-30221.

[35] The author of the PAPAGENO event generator is Dr. Ian Hinchliffe. Current address: Lawrence Berkeley Laboratory, Berkeley CA 94720.

[36] D. Brown and S. Kannappan. *SETPRT, a Single Parton Fragmentation Module*. CDF Note #873 (1989)

[37] A. D. Martin, R. G. Roberts, and W. J. Stirling. Phys. Rev. **D 37**, 1161 (1988).

[38] A. D. Martin, R. G. Roberts, and W. J. Stirling. Mod. Phys. Lett. **A4**, 1135 (1989)

[39] E. J. Eichten, I. Hinchliffe, K. D. Lane, and C. Quigg. Rev. Mod. Phys. **56**, 579 (1984)

[40] E. J. Eichten, I. Hinchliffe, K. D. Lane, and C. Quigg. Rev. Mod. Phys. **58**, 1065 (1986)

[41] M. Diemoz, F. Ferroni, E. Longo, and G. Martinelli. Z. Phy. **C 39**, 21 (1988)

[42] F. Paige and S. D. Protopopescu. *ISAJET Monte Carlo Version 6.21*. Brookhaven National Laboratory Technical Report BNL 38034. 1986.

[43] T.Hessing, S. Behrends, P. Tipton and B. Winer. *Monte Carlo Fragmentation Tuning for Jet Energy and Resolution Analysis*. CDF Note #1131 (1990)

[44] CELLO Collaboration. Z. Phy. **C 46**, 537 (1990)

[45] A. Roodman. *A Measurement of the $p\bar{p} \rightarrow W \rightarrow \tau\nu$ Cross-Section Times Branching Ratio as a Test of Lepton Universality.* PhD Thesis, University of Chicago. August, 1991.

[46] D. Brown. *A Study of Dijet P_t Balancing using 1987 Data.* CDF Note #835 (1989).

[47] CDF Collaboration. *Measurement of the Isolated Prompt Photon Cross Section in $\bar{p}p$ Collisions at $\sqrt{s} = 1.8$ TeV.* Fermilab preprint: FERMILAB-Pub-92/31-E. February, 1992.

[48] CDF Collaboration. *Measurement of the Z_{p_T} Distribution in $\bar{p}p$ Collisions at $\sqrt{s} = 1.8$ TeV.* Fermilab preprint: FERMILAB-Pub-91/199-E. July, 1991.

[49] B. Winer. *MET Corrections for the Inclusive W Boson Sample.* CDF Note #1240 (1990)

[50] J. Freeman and C. Newman-Holmes. *A Fast Calorimeter Simulation for SSC Detector Design.* Fermilab preprint: FERMILAB-Conf-87/231. December, 1987.

[51] D. Brown, S. Kannappan, and M. Shapiro. *QFL Version 2: Improvements and Checks.* CDF Note #753, 1988.

[52] A. Beretvas and J. Freeman. *Proceedings of the 1986 Summer Study on the Physics of the Superconducting Supercollider*, Snowmass, CO, 482-486.

[53] S. Behrends, M. Shapiro, and A. Roodman. *Update on Central Calorimeter Response to Pions and Tuning of Qfl.* CDF Note #1344, 1991.

[54] T. Hessing and B. Winer. *A Brief Note Comparing Jet Data to QFL.* CDF Note #1347, 1991.

[55] J. M. Benlloch and T. Rodrigo. *Tracking in QFL.* CDF Note #1634, 1991.

[56] V. Barger and R. Phillips. *Collider Physics.* (Addison-Wesley Publishing Co., Menlo Park, CA, 1987).

[57] CDF Collaboration. *Proposal For an Upgraded CDF Detector.* CDF Note #1172, 1990.

[58] G. Zech. Nucl. Inst. and Meth. **A 277**, 608 (1989)